AN EXPERIMENTAL INVESTIGATION OF GAS-SOLID INTERACTION PHENOMENA

By

JOHN WILLIAM CORYELL

Bachelor of Science

Oklahoma State University

Stillwater, Oklahoma

1965

Submitted to the Faculty of the Graduate College
of the Oklahoma State University
in partial fulfillment of the requirements
for the Degree of
DOCTOR OF PHILOSOPHY
May, 1972

AN EXPERIMENTAL INVESTIGATION OF GAS-SOLID

INTERACTION PHENOMENA

Thesis Approved:

Lionel M. Raff
Thesis Adviser

J Paul Devlin

Vic Pundit

Thomas G Hunter

D Thurham
Dean of the Graduate College

ACKNOWLEDGEMENTS

I am indebted to Dr. Lionel M. Raff, whose advice and patient understanding was essential throughout this work.

Jerry Lorenzen deserves recognition for the significant contributions that he made to this effort.

Heinz Hall and his staff in the Physics and Chemistry Machine Shop merit particular thanks for the uniformly excellent fabrications they supplied and for the engineering design assistance they gave.

This study was made possible by financial support from the Oklahoma State University Research Foundation through a National Science Foundation grant. Appreciation is also expressed to the Chemistry Department for financial support in the form of an Assistantship.

Finally, I wish to express my gratitude to my wife, Kay, for the contributions that she made to this work. Without her encouragement and support, the effort necessary would have been much greater and the experience far less satisfying.

TABLE OF CONTENTS

LIST OF TABLES

LIST OF FIGURES

Figure Page

CHAPTER I

INTRODUCTION

Experimental and theoretical examination of gas-solid interactions are important for several reasons from both a practical and theoretical point-of-view. The technological aspects of space travel, orbiting satellites, missiles and the like demand an accurate knowledge of drag coefficients for a vehicle moving through a rarefied gas. The free molecule drag coefficient, C_D, could be calculated if the vehicle received from each gas particle in collision with the vehicle all the momentum that the particle has relative to the vehicle. This complete accommodation of the gas particles at a surface typically does not occur. The particles transfer a portion of their momentum to the surface and then rebound with some mean velocity, $\bar{v}_r$. No satisfactory technique currently exists for calculating the mean velocity of the rebounding particles a priori. Consequently, some estimate of $\bar{v}_r$ and of C_D must be attempted. Often these estimates lack the necessary precision. For instance, the orbital decay of artificial satellites in the earth's upper atmosphere can be related to the product of atmospheric density and drag coefficient. Harris and Jastrow[1] obtained an average density by assuming $C_D = 2.3 \pm 0.3$. Other calculations involving C_D have used values from 2.0 to 2.7.[2]

There is similarly a great academic interest in elucidating the important features of the gas-solid interface because of what this

can tell us of the solid state itself, particularly in terms of the potential energy at the solid surface. The process of gas-solid collision is of obvious importance in the field of heterogenous catalysis. There are a very great number of natural phenomena, such as corrosion and vapor condensation, which have their basis in the incomplete energy transfer that takes place in rarefied media between gas particles and a solid surface.

The earliest studies of gas-solid interactions followed the kinetic theory. Kundt and Warburg[3] tested the Boltzman equation as it is applied to a non-equilibrium condition. They examined the effect of gas viscosity on the damping of a vibrating disk, verifying Maxwell's prediction that gas viscosity is independent of gas density. Maxwell[4] explained this low density phenomenon by introducing the theory of slip. He suggested that gas particles strike the surface with some velocity characteristic of the bulk gas, while the gas that leaves the surface possesses an energy characteristic of the surface. Thus, on the basis of kinetic theory, there is predicted to be some temperature discontinuity at the surface. It was a further triumph for kinetic theory when Smoluchowski[5] verified the existence of this temperature jump by determining the heat transfer between a glass surface and gaseous hydrogen.

Knudsen[6-8] introduced the term "accommodation coefficient" (AC or α) to describe the fractional energy and momentum transfer at the gas-solid interface. The usual and more general definition of AC is from Blodgett and Langmuir[9]:

$$\alpha = \frac{E_r - E_g}{E_s - E_g} \qquad (1)$$

where the quantities are derived and defined in the following way. Assume a gas beam, temperature T_g, that impinges upon a solid surface of temperature T_s, where $T_s > T_g$. The energy flux through the surface of the solid is the difference between the energy carried to the surface by the incoming particles in the gas beam and the energy carried from the surface by the particles that carom away. If the interaction between the gas beam and the surface is incomplete, the mean energy of a particle in the reflected stream is the same as that of a particle issued from a body of gas at some temperature, T_r, which lies between T_s and T_g. If the interaction were complete, the mean energy of the particles in the reflected stream would be characteristic of that possessed by a beam effusing from an ideal oven with a temperature equal to that of the surface, T_s.

Let N be the number of gas particles which strike a unit surface area per second, and let the particles possess a mean energy, $\bar{e}_g$, which corresponds to their temperature, T_g. The incident energy flux, E_g, is therefore $\bar{e}_g N$. Assume a steady state accumulation of particles at the surface; that is, N(in) equals N(reflected). The energy flux away from the surface, E_r, is $\bar{e}_r N$. The energy flux across the surface is simply $E_r - E_g$. If the interaction between the gas particles and the surface were complete, the energy flux through the gas-solid interface would be $E_s - E_g$. Therefore, the accomodation coefficient measures the relative efficiency of energy transfer per collision between a stream of gas particles and a solid surface.

It is more convenient to define AC as a function of the temperature of the gas beam and of the solid surface. Since 2 kT represents the mean translational energy per particle that issues from a body of

gas in equilibrium at a temperature T, the AC may be defined in terms of the pertinent temperatures as:

$$\alpha = \frac{T_r - T_g}{T_s - T_g} \tag{2}$$

It should be noted that the AC defined in this fashion is not a well-behaved function, that is, the AC expression is not defined at T_s equal to T_g. This somewhat undesirable feature was removed by Raff[10] and co-workers. They defined an energy transfer coefficient (ETC or α_E) which is a measure of the fraction of energy transferred across the gas-solid interface:

$$\alpha_E = \frac{E_g - E_r}{E_g} \tag{3}$$

Alternatively, it may prove to be more convenient to use the modified expression of Jackson[11];

$$\alpha = \lim_{T \to 0} \frac{T_r - T_g}{T} \tag{4}$$

where $T = T_s - T_g$. This is a particularly useful expression for those experimental systems where the AC is markedly dependent upon the difference in temperature between the gas and the surface.

An alternative method is to express accommodation in terms of the momentum transferred across the gas-solid interface[12]. The defining equation for such measurements is generally of the form[13]:

$$\alpha = \frac{N_i - N_r}{N_i - N_s} \tag{5}$$

Where N_i is the normal component of momentum for the impinging gas particle and N_r is the normal component of momentum for the reflected particles. The value of N_s is the normal momentum which would be exhibited by the gas particles if they left with velocities characteristic of the surface temperature (complete accomodation). This generally implies an assumption of a Maxwell-Blotzman distribution for the diffusely scattered, completely accommodated gas particles. Momentum accommodation normal to a surface is typically determined with a sensitive torsion balance apparatus. A metal target mounted on one arm of the balance is suspended in a beam of test gas inside a vacuum envelope. The other arm of the balance operates as a null force device, where the nulling force required to keep the target from rotating in the beam is directly related to accommodation of momentum at the target surface.

There are presently three standard methods for determining accommodation coefficients. Roughly two-thirds have been obtained by the Low Pressure method as elucidated by Knudsen[6,7]. Kennard[14] has reviewed the Temperature Jump method as it is currently applied. This technique has accounted for about one-third of the reported AC. Finally, the time-of-flight method (TOF) as utilized by Moran[15,16], Hinchen and Foley[17], Hagena[18,19], and others[20] has yielded a handful of published results in the last few years.

The first two methods are conductivity cell measurements. The experimental apparatus typically consists of a small diameter filament made from the solid under investigation. This filament is suspended along the axis of a glass tube which has a diameter much greater than that of the wire. The wire may be heated by the passage of a

precisely measured electrical current. Characteristically, the wire is made of some engineering metal with a high melting point, such as tungsten, so that it may be flashed clean at a very high temperature. The cylinder is filled with the gas of interest, and the surrounding glass wall is cooled. A net transfer of heat from the filament to the walls is established as a result of free molecular collision and radiation. The inside walls of the cylinder usually are covered with an effective getter (mischmetal) which traps contaminant gases, assuring a perfectly clean surface on the wire for the duration of the experiment. The resistance of the filament is a direct measure of its temperature for a given current flow. The current required to maintain the filament at an average temperature, T_s, and the potential drop across the filament at that temperature determine the power input, W_f, to the filament. This power is dissipated not only by gas conduction but also through end loss to the filament supports and by radiative losses. The degree to which these latter two contribute to W_f may be found from duplicate experiments in a good vacuum. This power is denoted W_v. Thus, the net steady state power loss from unit filament area to the gas W_g is merely the difference:

$$W_g = W_f - W_v \tag{6}$$

In the Low Pressure method, the gas during a run is maintained at 0.05 mm H_g to assure free molecular flow. The AC is defined:

$$\alpha = \frac{W_g}{W_{KT}} \tag{7}$$

where W_{KT} is the free molecule heat conductivity and is equivalent to

the difference $E_s - E_g$. Under the conditions of this experimental method, W_{KT} may be derived as[21]

$$W_{KT} = (P)(A)(T_s - T_w)\left(\frac{C_v}{R} + \tfrac{1}{2}\right)(R/2\pi MT_g)^{\frac{1}{2}} \quad (8)$$

The quantities in this expression are as follows:

P = gas pressure

A = area of filament

C_v = constant volume heat capacity of the gas

R = gas constant

M = molecular weight of the gas

For the Temperature Jump method, the gas pressure is in the range of 10 to 100 mm H_g. Measurements of thermal conductivity are made within that range of pressure in a conductivity cell. At these pressures free molecular flow is no longer maintained within the cell. There is, therefore, a temperature discontinuity near the filament, the so-called "temperature jump". The accommodation coefficient is related to the distance of the temperature jump from the filament, but the theory relating these two quantities is subject to some criticism. However, in those cases where reasonable care was taken in surface preparation[22,23], the Temperature Jump method yields results which agree favorably with Low Pressure measurements, for which the theoretical foundation is unquestioned. The first measurements of AC with any degree of precision was by Roberts[24,25] in 1930. He was primarily interested in determining the accommodation of gases on clean tungsten surfaces. He was limited by the vacuum technology of the day, and his results undoubtedly reflect measurements made on surfaces of questionable cleanliness. Thomas and co-workers[26-32] have produced

results using the Low Pressure method which are probably the most reliable of any with this technique. For instance, Thomas and Schofield[30] report a value for the AC of helium on tungsten of 0.0165, which must be representative of the interaction between inert gaseous particles and a truly clean surface. They employed an effective getter, deposited on the walls of their vacuum system, to trap the residual gases in the region of the tungsten filaments. In the absence of such gases, the measured accommodation coefficient remained constant for a time significantly longer than in previous tests where no getter was used. Residual gases typical of most vacuum systems[21] interact strongly with metal surfaces, increasing the thermal accommodation coefficient.

The measurement of accommodation coefficient using either conductivity cell technique suffers from several faults. The gases are limited to those which will not interact strongly (adsorb) on the metal surface nor which will react with the getter material. This effectively restricts the gases that can be used to the noble gases. Many metals possess an oxide coating on their surface which is not volatile even at the melting point of the base metal, thus some cleaning procedure more stringent than simple flashing of the filament must be employed to assure a clean metal surface for the accommodation experiment. Eggleton and Tompkins[33] resorted to reduction of the oxide by heating in the presence of hydrogen, but they then had to bombard the filament with ionized nitrogen and argon to remove the adsorbed hydrogen.

Measurements within conductivity cells are typically made over a rather limited range of temperatures with a severely restricted temperature differential between the filament and the cylindrical wall. Menzel and Kouptsidis[32] have extended the technique somewhat to include gas

temperatures between 77°K and 313°K and with a temperature difference between wall and filament of up to 50°K. The temperature of the gas is always less than the temperature of the surface. The actual crystal structure of the surface as well as its relative smoothness are parameters of the interaction which are not subject to adjustment nor are they even known in a typical conductivity cell measurement. The conductivity cell measurement of AC is a true bulk measurement; it represents an average over all of the gas particle angles of incidence relative to the metal surface as well as an average over all possible gas particle energies. Since this constitutes an equilibrium measurement, the results yield virtually no knowledge of the precise nature of the gas-solid interaction. Yet it is the energetics of the interaction, on a molecular scale, which is of central importance in elucidating the parameters which affect the accommodation of gas by the surface.

These objections are, for the most part, removed in a molecular beam experiment. Most molecular beam experiments involving gas-solid interactions have been concerned with determining flux distributions of the scattered particles. A few have surmounted the experimental difficulties involved in determining the distribution of particle energies within the beam of scattered gas. Time-of-flight measurements of AC fall in this latter category and will be reviewed later with the other molecular beam techniques.

Roberts' experimental determination of accommodation coefficients prompted several theoretical studies[11,35-38] of the interaction of an inert gas with a clean metal surface. Of these, the study by Deveonshire[37], employing a quantum model is the most general. However, following Thomas and co-workers' definitive study of AC using

scrupulous experimental conditions, Brown[39] attempted to fit Devonshire's model with existing data with unsatisfying results.

In recent years, the advent of high speed computers has led to models describing the gas-solid interaction with ever-increasing complexity. Zwanzig[40] and Cabrera[41] have separately presented a one-dimensional classical calculation based on the collision of a gas atom with a solid that was represented as a semi-infinite mass-spring ensemble. Goodman[42-53], in a series of papers, has extended Zwanzig's work by introducing a 3-dimensional lattice for the solid. He is able to calculate accommodation coefficients for a 1-D gas interacting through a Morse potential with his 3-D lattice. The model possesses many obvious faults, and yet it yields good agreement with existing data on AC. This might suggest that the accommodation coefficient alone is too insensitive a test of any proposed model. Trilling[54-57] removed the restriction of a 1-D gas. His calculations also agree well with Thomas' measurements.

An area of very great experimental activity in the last seven years has been the determination of scattering distributions of gas beams reflected from metal surfaces. Some additional attention has been directed toward the more difficult problem of determining the speed distribution of the scattered particles. Lack of a precise knowledge of particle energies before and after collision with the surface has precluded more than qualitative to semiquantitative evaluation of gas-solid interaction parameters. However, the actual spatial distributions have been measured for a great many systems.

In all experiments involving gas-solid interactions, the nature of the surface is of prime importance. Experiments employing metal

surfaces are difficult to evaluate in terms of simple interaction phenomena because of the inherent uncertainty concerning the precise condition of the surface at the time of the experiment. Both surface structure (roughness and crystallinity) and adsorbed species (contamination) have very pronounced effects on scattering distribution.

The problems of surface preparation have received considerable attention. Roberts[58] reviews several methods of generating clean surfaces in an ultra-high vacuum. Saltsburg[59-69] and co-workers have had considerable success with the technique of continuously depositing a fresh target surface on a cleaved mica substrate during the course of a scattering measurement. Target material evaporates from a crucible located away from the gas beam path. The target particles condense at a rate roughly ten times that at which background contaminants could be expected to arrive at the target. Hence, they argue, the potential contaminants are immediately buried. Moreover, a careful adjustment of substrate temperature can insure epitaxial growth of a single crystal face. It now appears, however, that the actual temperature of the gas-solid interface during deposition may have been a few hundred (200-400) degrees hotter than they reported.[70] This effect of continual vapor deposition on the temperature of the thin film at the deposition surface was studied by Belous and Wayman.[70] To insure a relatively clean surface, the more conventional techniques of ultra-high vacuum production were used by Hinchen[17,71,72], et al.

The first experiments employing a molecular beam were merely directed toward determining the directional nature of the reflected flux of gas particles. Esterman and Stern[73] demonstrated the diffraction of helium from a cleaved lithium fluoride crystal. Frish[74]

was able to calculate Planck's constant from similar data taken using a gas beam with a very good velocity resolution. Recently, Crews[75,76] studied helium scattered from lithium fluoride. He obtains intense diffraction peaks which he discusses in terms of the theoretical work of Lennard-Jones and Devonshire.[77] O'Keefe[78-82], et al., examine the same system to determine how molecular properties other than de Broglie wavelength affect the scattering.

The spatial distribution of the gaseous particles relative to the surface are usually defined in the following fashion: The relationships are shown in Figure 1. The particles at temperature, T_g, strike the surface, temperature T_s, with spherical polar angles of θ_i and Φ_i, where the z-axis is taken as the surface normal. The in-plane angle of incidence, θ_i, and the surface normal define a plane into which the greatest majority of the beam flux is scattered with an in-plane angle of reflection, θ_r. A small flux is found out-of-plane with an angle of reflection, Φ_r. Typically, θ_r is not the same as the specular angle of reflection, θ_s. In some cases the maximum in θ_r may be coincident with the target normal (cosine scattering).

Zahl and Ellet[83,84] measured the flux distribution of mercury vapor scattered from sodium and potassium chloride and from potassium bromide and iodide. They found generally lobular patterns with $\theta_r > \theta_s$. The difference between these angles increased as the beam was cooled or the surface heated. Zabel[85] reported on the diffraction of the gases helium, neon, and argon from sodium chloride. Further studies involving heavy metals scattered from simple ionic crystals were conducted by Kellog[86], Hancox[87], and Fisher[88], et al. In each case there was observed the same trends in lobe maxima with respect to θ_i,

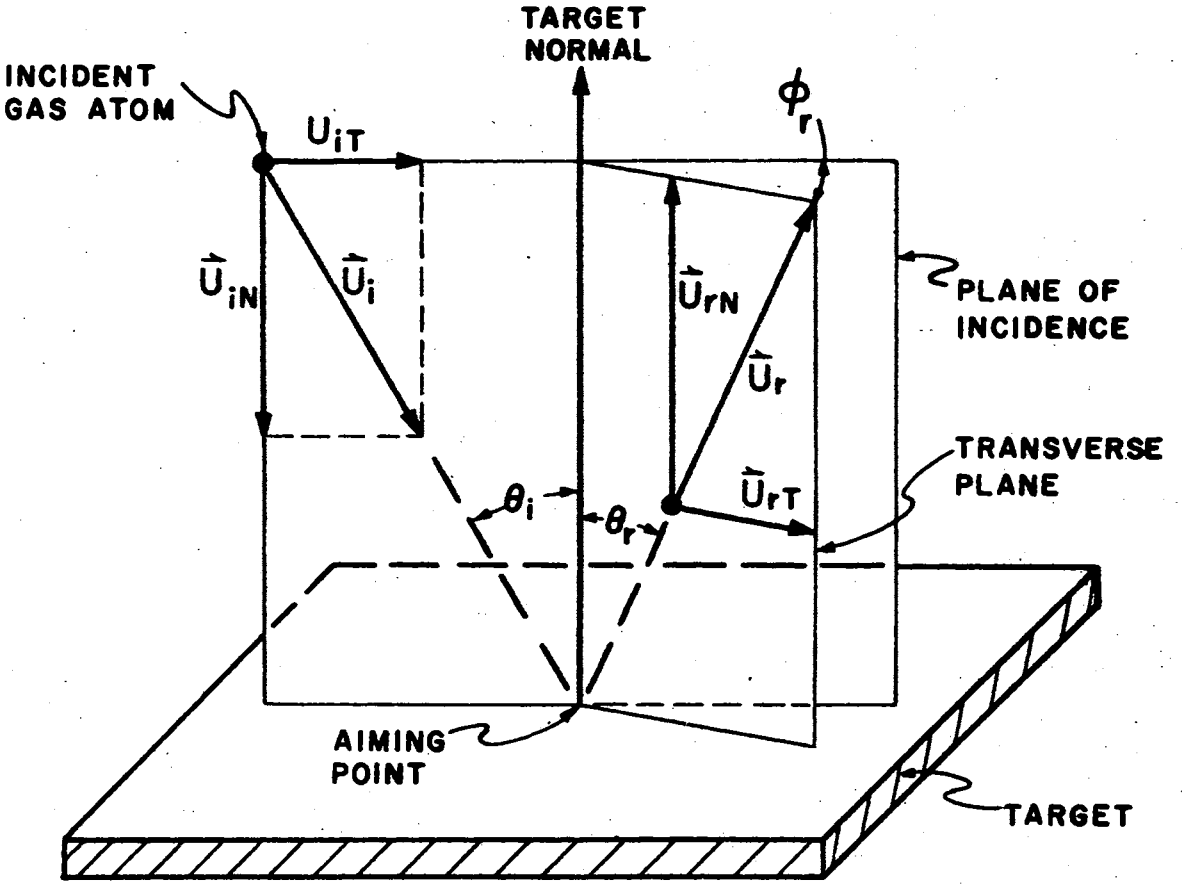

Figure 1. Three-Dimensional Gas-Solid Interaction Model

T_s, and T_g as was reported by Zahl and Ellet.

Recent advancements in electronic signal processing has greatly increased the wealth of information that can be obtained from a molecular beam experiment of this type. Sensitivity, which is a function of signal-to-noise ratio, is increased immensely by modulating the incoming beam of particles and then employing a lock-in amplifier to reduce background noise to a tractable level. Alternatively for some experiments, notably time-of-flight, the preferred instrument is the multichannel analyzer which locates the coherent signal floating in sea of random background information.

The application of the lock-in amplifier to molecular beam research was developed by Fite and Brackman[89]. Smith and Fite[90-92] used this technique in determining the scattering distribution of hydrogen and argon from a polycrystalline nickel surface. By determining the approximate phase shift between the reflected and incident beams and relating this to a speed change within the beam, Smith found that the accommodation coefficient depends upon the angle of scattering, θ_r. He estimated an accommodation coefficient of 0.8 near the normal versus 0.3 near the specular angle with room temperature argon scattered from nickel at 450°C with an in-plane angle of incidence of 60°.

The effect of gross crystal structure and surface condition is easily seen in the work of Smith and Saltsburg[59]. With a helium beam at 300°K incident at 50° upon a gold target at 560°K, scattering distributions were measured both with and without continuous deposition of target material. The distribution is narrow and specularly directed during the time the surface is kept clean with the continuous deposition of gold. After deposition is ceased for about 30 minutes, a

steady-state condition is reached in which the distribution is quite broad and only slightly specularly directed.

In the same work, Smith and Saltsburg show the effect in the scattering distribution in going from a polycrystalline target to a target that is a single crystal film. A polycrystalline target results from maintaining the substrate at 300°K during deposition, while a single crystal (111 face) results from deposition onto a substrate at 560°K. The polycrystalline film shows an almost perfect cosine scattering distribution, while the single crystal yields a distribution that is narrow and specularly directed.

Hinchen and Malloy[72] report on the scattering of helium, neon, and argon from targets of platinum, nickel, tantalum, and tungsten. In a separate measurement, they note the effect of a beam of molecular oxygen on a heated platinum target. They found that platinum targets with differing crystallographic orientations relative to the impinging gas beam show only slightly differing scattering distributions.

In general, all scattering distributions from clean surfaces are similar in gross features. The distribution is lobate, with a maximum varying from above the specular angle to below the specular angle, depending upon whether the gas temperature, T_g, is less than or greater than the temperature of the surface, T_s. This effect is increased as θ_i is increased. The out-of-plane scattering is symetric about the principal plane of scattering, and the out-of-plane distribution is much more narrow than the in-plane distribution. Both in-plane and out-of-plane scattering distributions broaden as the ratio of gas atom mass to surface atom mass is increased. As that ratio increases, the angular position of maximum spatial scattering is a much more sensitive

function of the relative temperatures of the gas and surface. These last two observations are consistent with the expectation that there would be a greater interaction between the surface and a gas atom of larger polarizability.

Spatial scattering lobe full-width at half maximum (FWHM) increases with the ratio T_s/T_g and with decreasing θ_i. These observations are consistent with the prediction that gas-solid interactions are greatest for direct impact between the colliding species and that most momentum transfer between gas and solid will occur along the normal to the surface and relatively little along the tangent to the surface. Transfer of the normal component of momentum also accounts for the trends seen in the deviation of spatial scattering lobes from the specular angle, as was mentioned previously.

In-plane spatial scattering intensity ($\Phi_r = 0^o$) increases toward a maximum as θ_i decreases. Conversely, out-of-plane scattering intensity approaches a minimum as θ_i approaches 0^o. For those cases where average speed of the scattered atoms has been determined for both in-plane and out-of-plane scattering, the maximum speeds are found at the peak of the scattering lobe spatial distribution for lower T_s/T_g and at the surface normal at higher T_s/T_g[20,93].

Broadening of the spatial scattering lobes for heavier gases from various well-ordered metal surfaces correlates well with Debye temperature of the surface. Peaks are sharper for those metals with higher θ_D[94]. This effect has been variously interpreted in terms of "stiffer" lattices[95] or lesser amounts of thermal "roughening"[96]. Spatial scattering lobes are generally sharper and more intense (by a factor of 2 for Pt)[94,97] from crystal planes with the closest packing.

Other effects are seen in the spatial distributions of gases scattered from ionic crystals where surface potential energy exhibits greater periodicity and amplitude than is seen in uncontaminated metal surfaces. Lithium fluoride, as well as other alkalai halides, has received a great deal of attention in these types of studies from the time that Stern and his associates[73,98-100] confirmed the dual nature of atomic beams by verifying de Broglie's wave relation $\lambda = h/mv$.

Lithium fluoride exists in a simple cubic structure, where the dimension of the unit cell is 2.01 Å.[101] However, the diffraction grating spacing in LiF is the distance between rows of nearest neighbors, 2.84 Å. Sharp diffraction peaks in the spatial scattering distributions of lighter gases reflected from freshly cleaved LiF have been reported by a number of workers.[75,76,78-82,102-104] However, considerable speculation exists concerning the surface composition of the crystals used. It appears likely that if the crystal is cleaved outside of a good vacuum, its surface immediately becomes contaminated with water vapor. This is best seen by comparing the work reported by Crews[75], who employed vacuum cleavage with that of O'Keefe[78-82], et al, who did not. Crews found that adsorption of water vapor up to a few adlayers sharpened scattering peaks while O'Keefe, et al., got no alteration of their spatial distributions upon addition of H_2O vapor. Water vapor strongly interacts with the LiF lattice, apparently forming well-ordered domains and possibly increasing the amplitude of the surface potential energy contours[68] as well.

Helium[75,103,104] and the hydrogenic molecules[81,82] exhibit the most well-defined diffraction peaks in scattering from LiF. Diffraction has been observed in the case of neon, but not argon.[80,102] Diffraction

was not observed in the spatial scattering distributions of helium reflected from silver that had been deposited epitaxially upon a single crystal of LiF.[68] This suggests that the amplitude of the potential energy contour above the surface is a key parameter influencing coherent scattering effects.

The scattering distributions for the lighter atoms show more diffracted beams at lower θ_i. Beam intensity decreases with increasing M_g/M_s. This effect is particularly strong in deuterium, where maximum intensity is ~4x less than that of hydrogen[81], strong evidence of rotational energy state coupling with the surface. For all data, the diffraction peaks become much less distinct as T_s is increased.

Coherent scattering distributions have been reported for a few cases of intentionally contaminated surfaces. Weinberg and Merrill[105] generate a (3 x 5) tungsten carbide overlayer on a W(110) substrate. This surface is stable at the normal annealing temperature of tungsten (1800°K). They found intense diffraction peaks for helium and deuterium and calculated a grating spacing of 11.0 Å for the incident gases at 295°C. The diffraction patterns seen from the carbide surface were about 3x more intense than those of the clean W(110). Taylor, et al.,[106] found two peaks in the spatial scattering distributions of helium ($T_g < 900°K$) on annealed platinum purposely contaminated with oxygen. The authors speculate that these might have arisen from coherent scattering effects at the surface.

Mason and Williams[104] report diffraction effects in the spatial distributions of helium from LiF single crystal contaminated with ethanol. The diffraction peaks were quite sharp, and indicated a (2 x 2) rhombus with the methyl group removed from the surface in an

upright position. No diffraction patterns were observed for CCl_4, C_6H_6, CH_3OH or H_2O.

An additional result of scattering distribution measurements with LiF single crystals under carefully controlled conditions has been the detection of bimodal distributions for the heavier gases (M_g > Ne). This has been reported in detail by Smith[80-82] and co-workers. They examine the spatial scattering distributions of the inert gases along like (110) and unlike (010) rows on the surface of LiF. These scattering distributions are similar to those already summarized for the noble gases/metal crystal systems. The chief difference in the lobular patterns found in scattering from metals and in scattering from LiF is that the distributions in the latter case are characterized by having two peaks in the principal plane ($\Phi_r = 0^o$). One peak appears to be rather insensitive to θ_i and is more-or-less "fixed" at $\theta_r = 65^o$. The other "inelastic" lobe maximum is subspecular, with a peak intensity very sensitive to experimental conditions. The bimodal nature of these distributions increases with decreasing M_g and with decreasing θ_i. At $\theta_i = 30^o$, the subspecular neon peak appears near or even behind the surface normal. Increasing T_s dramatically shifts the subspecular peak toward the specular direction. The supraspecular peak is moved away from the surface slightly. The authors observe peaks in the out-of-plane spatial distributions. The extent to which the spatial scattering distributions show a bimodal character is much less for beams aimed along rows of like atoms (110) than across the surface along rows of unlike atoms (010). For xenon, scarcely any bimodal character is observed at $\theta_i = 40^o$, (110) azimuth.

Accurate time of flight measurements of gas-solid interactions

commenced with the work of Moran[15] in 1959. In this technique, a molecular beam of known speed distribution is modulated to form sawtooth wave packets of gas particles. This modulated beam strikes a target and is reflected and detected just as in the previously described experiments. A multichannel analyzer isolates the signal produced by the detector as the sawtooth wave arrives from the scattering surface. The phase and amplitude of the signal at the multi-channel analyzer depends on the nature of the gas-solid interaction.[93,107] From an assumption of the type of interaction with the surface and from a knowledge of the distance the packet traversed, the accommodation coefficient may be calculated by comparing the phase angle between the packet and its modulator with the phase angle the packet would have had if it had experienced a completely elastic collision at the surface. However, the measurement of phase angle yields accommodation coefficients that are only as accurate as the interaction model that is assumed for the purposes of data reduction.[107]

This technique is burdened with some uncertainty. The phase angle of the signal relative to the modulator is measured with a precision in the order of a few degrees ($\sim 5^{\circ}$). When this uncertainty is propagated through to the final calculation of an effective AC, the result is an uncertainty of $\pm$ 200% for helium on a platinum surface at 970°K.[17] Moreover, the speed distribution of the particles in the reflected beam varies with scattering angle and with beam modulation frequency, which introduces a further small uncertainty in the final calculation of the accommodation coefficient.

The technique is useful in examining the qualitative features of the gas-solid interaction. Moran[16], et al., found that the mean energy

in the reflected beam increased with decreasing θ_r. Hagena[18] has made time-of-flight measurements of argon scattered from untreated stainless steel. Time-of-flight techniques are particularly effective for beams of moderate energy (2 to 20 ev), where supersonic beams[108] of very narrow speed distribution are employed. This energy range has received increased attention in gas-solid interaction experiments with the improvement in beam sources and from the appreciation of what spatial scattering distributions of these energetic beams reveal about the gas-surface interaction potential. At an energy somewhat less than 1.0 ev, there is a general reversal of trends in spatial scattering distributions as a function of the energy of the incident gas atom. This effect was originally predicted by Oman[109] and it has been called "structure" scattering. (As opposed to the "thermal" scattering seen with less energetic beams.) Gas atoms that have a large kinetic energy penetrate the repulsive potential of the crystal lattice, and the surface appears "rough". This rough nature allows increased transfer of momentum tangential to the surface. As incident gas energy increases, the gas-solid interaction approaches that of hard spheres[110], and the spatial scattering distributions become peaked around the specular direction with large amounts of scattering out-of-plane ($\Phi_r > 0^o$).[20] The effect increases with M_g and with decreasing θ_i, and the result is seen in the deviation from specularity of the lobe maxima and in the lobe full-width at half maximum (FWHM). It will be recalled that for thermal beams, the FWHM decreases with increasing T_g. The onset of structure scattering, seen as a reversal in that trend, occurs at a somewhat higher incident particle energy than for the trend reversal of relative non-specularity.[111]

The theoretical treatment of the phenomena observed when a molecular beam is scattered from a solid surface has progressed steadily from its naive inception with Baule.[112] Early work in the field of theoretical scattering distributions was done by Lennard-Jones and Devonshire.[77] They developed a quantum theory of diffraction based on the constants of the surface potential field. Computational difficulties have been a serious limitation to the application of quantum theory to this problem. The recent work of Beder[113], Allen and Feuer[114-116], and others[53] shows some progress toward treating a realistic solid model in three dimensions.

There have been a number of classical scattering theories reported. Goodman[42-52] has studied the hard sphere head-on collision of a beam with a surface represented by particles initially at rest. Logan, Keck, and Stickney[117] have presented a model of the surface as a set of hard cubes. They calculate scattering patterns for non-normal incident beams assuming a hard sphere collision of the incident particle. Logan and Keck[94,118] modified this treatment by incorporating a "softer" potential at the surface. The results were in good qualitative agreement for the angular variation of the maxima of scattering distributions. However, the lobe full-widths at half lobe maximum (FWHM) are too narrow, show too much dependence on θ_i, and too little dependence on M_g when compared with precise data taken from the (110) surface of tungsten.[93]

Oman[119-123] and co-workers have presented a model that shows a great deal of promise. This model consists of a surface of mass points arranged with the desired lattice configuration and connected with harmonic springs to each other and to fixed sites at the periphery of

the target. They associate a Lennard-Jones (6-12) potential with the surface, set initial conditions of velocity, lattice phase angle, impact point and the like, and then follow a great number of individual trajectories by integrating the classical equations of motion. They have extended their calculations to include diatomic molecules.

This model has formed the basis for one proposed by Lorenzen and Raff[99-102], in which scattering distributions and energy transfer coefficients (ETC) are evaluated as a function of the parameters known to influence the degree of interaction at the gas-solid interface. They obtain semiquantitative agreement with existing experimental data and in addition, make several predictions which await a more precise experimental determination than has been published to date.

Their model consists of a target of nine movable lattice sites connected with harmonic springs to each other and to the immovable lattice sites outside the general domain of the aiming point. A gaseous atom is directed toward the target, and a Morse interaction potential is assumed between each movable lattice site and the gaseous atom.

The gaseous atom is incident on the lattice face at some randomly chosen aiming point, with an initial velocity, v_i, at spherical polar angles, θ_i and Φ_i. The scattering occurs at spherical polar angles, θ_r and Φ_r, at a reflected velocity, v_r. Initial conditions are specified for the system, and the integration of the classical equations of motion are carried out using a computer. The final conditions of interest in each trajectory are then analyzed as in an actual experimental determination. These conditions include the ETC for

particles incident at energy E_i and angles θ_i and Φ_i and the final scattering angles, θ_r and Φ_r.

Recently, McClure[127-129] has proposed a classical model for scattering phenomena that shows a great deal of promise. The model pictures the surface of a crystal as an extended three-dimensional array of anisotropic oscillators. An additive pairwise Lennard-Jones (n,6) potential is used to depict interaction energy between an incident gas atom and individual surface atoms. Monte Carlo techniques are employed to obtain polar distributions of spatial scattering patterns from uniform specification of initial conditions. The chief unique result is a series of spatial scattering distributions that clearly predict bimodal scattering for certain combinations of gas/solid interaction parameters. These types of distributions arise when a gas beam impinges on an interaction field which has a long range periodicity. A further requirement of the interaction field is an amplitude sufficiently great that some transfer can occur in the tangential component of the momentum of the gas atom as it experiences a languid collision with the "rough" surface. This is not "structure" scattering, since the effect is predicted for gas atom energies as low as 0.04 ev. These predictions are confirmed for the noble gases ($M_g \leq$ Ne) on LiF.[80,81]

Tungsten is an attractive choice for use as a target material in gas-solid interaction studies. It is mechanically strong with a very high melting point. It is available in high purity as a well-defined and easily cleaned single crystal or in polycrystalline form. It is a natural choice for catalytic study, and a great bulk of work has been done on adsorption of various atoms and molecules on the tungsten substrate. McCarroll[130] reviews the early studies in the field, and

Musket[131] makes an up-to-date presentation of the room-temperature adsorption of oxygen on tungsten.

Recently, Madey[132,133] and co-workers reported in detail on the desorption of oxygen on polycrystalline tungsten. Using a careful flash desorption technique, they determine sticking probabilities and desorption kinetics for the various adsorbed species present on a tungsten filament. They find a temperature-independent sticking probability of 0.70 at zero coverage. In the desorption process, roughly 3/4 of the adsorbate is removed as atomic oxygen. Activation energy for this process is 118 kcal/mole. The balance of the adsorbed oxygen is selectively removed in three more-or-less well-defined oxide stages. This desorption scheme is summarized as follows in order of removal: Stage 4, WO_2, desorption $T_p = 1200^oK$; Stage 3, WO_2-WO_3-W_2O_6, desorption $1600^oK \geq T_p \geq 1350^oK$; Stage 2, WO-$WO_2$-$WO_3$, desorption $T_p = 1700^oK$; Stage 1, atomic oxygen, desorption $T_p = 2200^oK$. The trioxide fraction has an activation energy for desorption of 110 ± 9.6 kcal/mole with a frequency factor of $10^{14 \pm 2}$.

These results are somewhat in disagreement with those of earlier workers who employed less rigorous experimental technique. Kohrt and Gomer[134] use a stepwise adsorption/desorption technique without mass spectrometric analysis of residual gas. Ptushinskii and Chuikov[135] were unable to determine desorption kinetics satisfactorily, although the molecular species involved were suitably identified. Germer and May[136] made a low energy electron diffraction study (LEED) of oxygen adsorption on a (110) tungsten face without investigating desorption kinetics. However, they found diffraction peaks which suggested that at low coverage (1/2 monolayer), oxygen is held at the crystal surface

in well-ordered domains consisting of alternate rows of tungsten atoms and atomic oxygen. Bauer[137] has confirmed the existence of this and other well-ordered oxide structures present on the tungsten substrate at elevated temperatures.

The present work investigates the interaction between a high intensity argon beam and an annealed tungsten foil surface. This study was carried out in a bakeable, ultra-high vacuum system. To the extent that these results confirm theoretical models of the interaction, the interaction potential for this gas-solid system may then be varied in subsequent calculations to fit the experimental data.

CHAPTER II

EXPERIMENTAL APPARATUS

A. Introduction

The experimental rigors encountered in thermal energy atomic and molecular beam studies have been well-catalogued. Chiefly, they are: (a) the production of a collimated beam of particles with a well-defined energy; (b) the utilization of a vacuum system with such a pumping reserve that there is no damaging long-term deterioration of conditions within the system as the experiment proceeds; and (c) the detection of a signal from the gas beam, where the useful signal power is anywhere from a few to several orders of magnitude less than the signal power arising from the "background" or residual gas in the system. In addition, energy transfer studies, such as the one described herein, place some additional restrictions on the design criteria of the apparatus. These criteria are as follows: (a) the surface upon which the beam particles impinge must be well-defined, which generally implies that the surface must be perfectly clean; and (b) the distribution of the individual energies for both the incident and reflected particles must be precisely known.

While advancements in vacuum and electronics technology have considerably ameliorated the first three difficulties listed above; the last two, which are unique to energy transfer experiments of this sort, remain as severe handicaps to the successful resolution of the

various parameters of the gas-solid interaction. This chapter describes some of the efforts made to remove or reduce all of the obstacles mentioned.

The experimental apparatus described herein allows the study of the energy transfer across the interface between a large number of possible gas-solid combinations. A nozzle source generates the beam of gas. Although proper functioning of the source does not require it, the gas studied in this work was restricted to argon. This facilitates the data interpretation, since this gas lacks rotational or vibrational degrees of freedom, and it is relatively easy to detect.

The beam is modulated prior to impinging upon a clean surface. The spatial and velocity dispersion in the reflected beam is determined with a slotted disk velocity selector (SDVS) and an ordinary ion gauge detector. The beam signal passes through a preamplifier located adjacent to the detector envelope. A lock-in amplifier accomplishes the final signal processing prior to the recording of the experiment. The target may be rotated about the two axes that are mutually perpendicular to the gas beam at its intersection with the target face. The SDVS and detector revolve about the aiming point on the target surface. The nozzle, entry portal on the SDVS, and detector all lie in the same plane.

The final assembly, shown in horizontal section in Figure 2, consists of the following major components: (1) The Main Scattering Chamber, maintained at a very low pressure; (2) The Beam Source Chamber, containing the quartz nozzle, collimating orifice, and beam modulator; (3) The Target Holder, which secures the surface; (4) The Speed Selector and Detector, mounted together on a large turntable; (5) The Detector

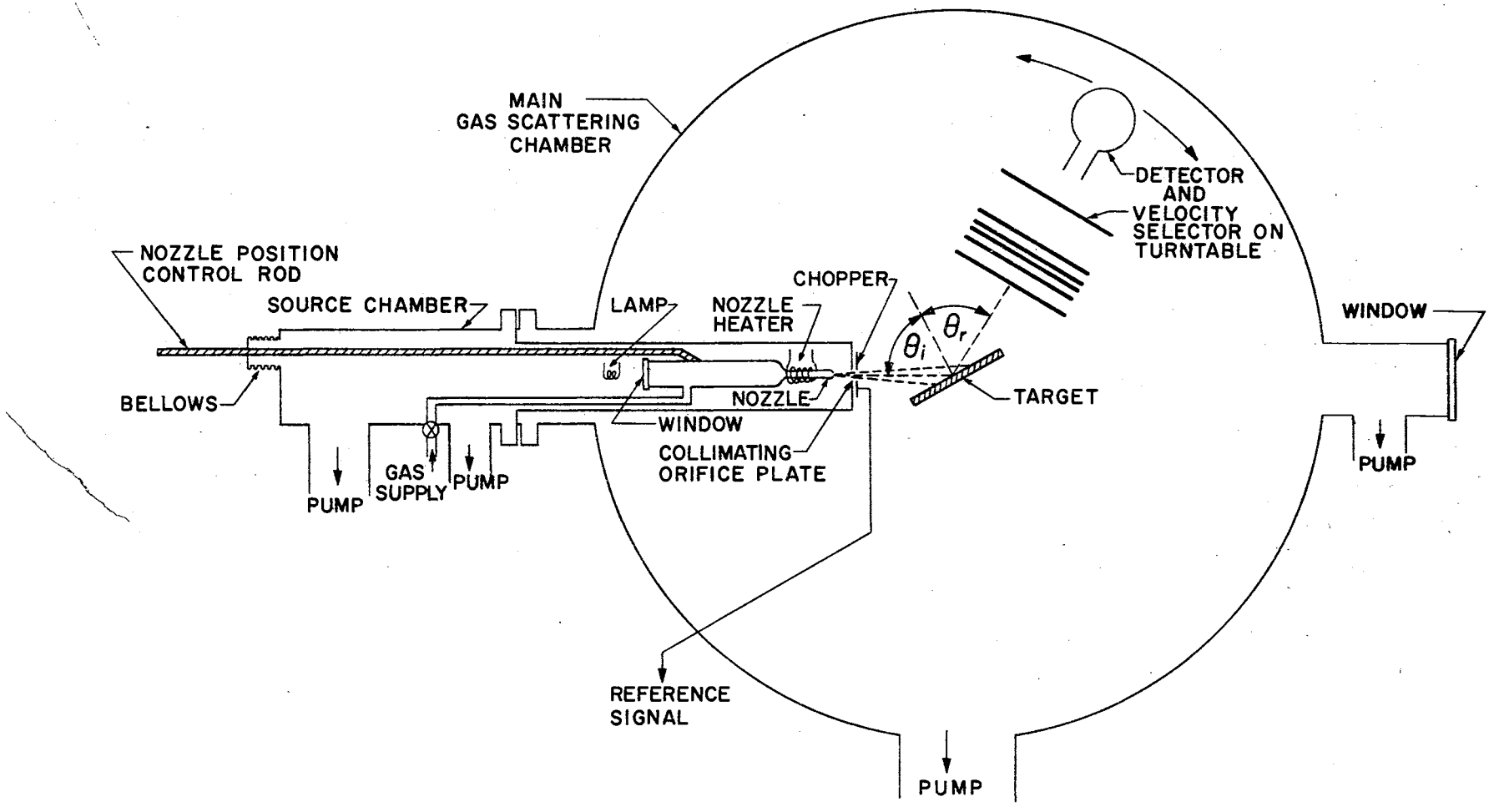

Figure 2. Experimental Apparatus Schematic

Electronics, which includes the detector power supply and all the signal processing equipment. A photograph of the apparatus is shown in Figure 3.

B. The Main Scattering Chamber

1. The Vacuum Envelope

The chamber is fabricated from cold-rolled stainless steel, secured with a continuous bead tungsten-inert gas (TIG) weld throughout. The internal dimensions of the main chamber are a diameter of 66.0 cm. and height of 49.2 cm, for a total wolume of about 175 liters. The wall of the envelope is .953 cm. thick, and the lid has a thickness of 1.91 cm. The chamber bolts to a baseplate that is 2.10 cm. thick, and an aluminum gasket 3.81×10^{-3} cm. thick seals the two. The gasket design is from the basic work of Batzer and Ryan.[138,139] Figure 4 is a detailed view of the sealing surface of the main scattering chamber. Batzer has suggested that narrow strips of aluminum, 12 inches wide, may be overlapped to seal a large diameter vacuum flange of this design. In this study, foil with a width of 30 inches was used so that there could be no air leaks across the lap. Note that Figure 4 shows the actual sealing land is not turned from the baseplate metal. A piece of bar stock 0.476 cm. square was TIG-welded into a groove in the baseplate and then the sealing taper was machined. This saved a significant amount of machining time.

The envelope has thirteen small flanges with short tubulations at strategic locations. There are two large side flanges. Flange dimensions are shown in Figure 5. The modifications of Batzer's basic

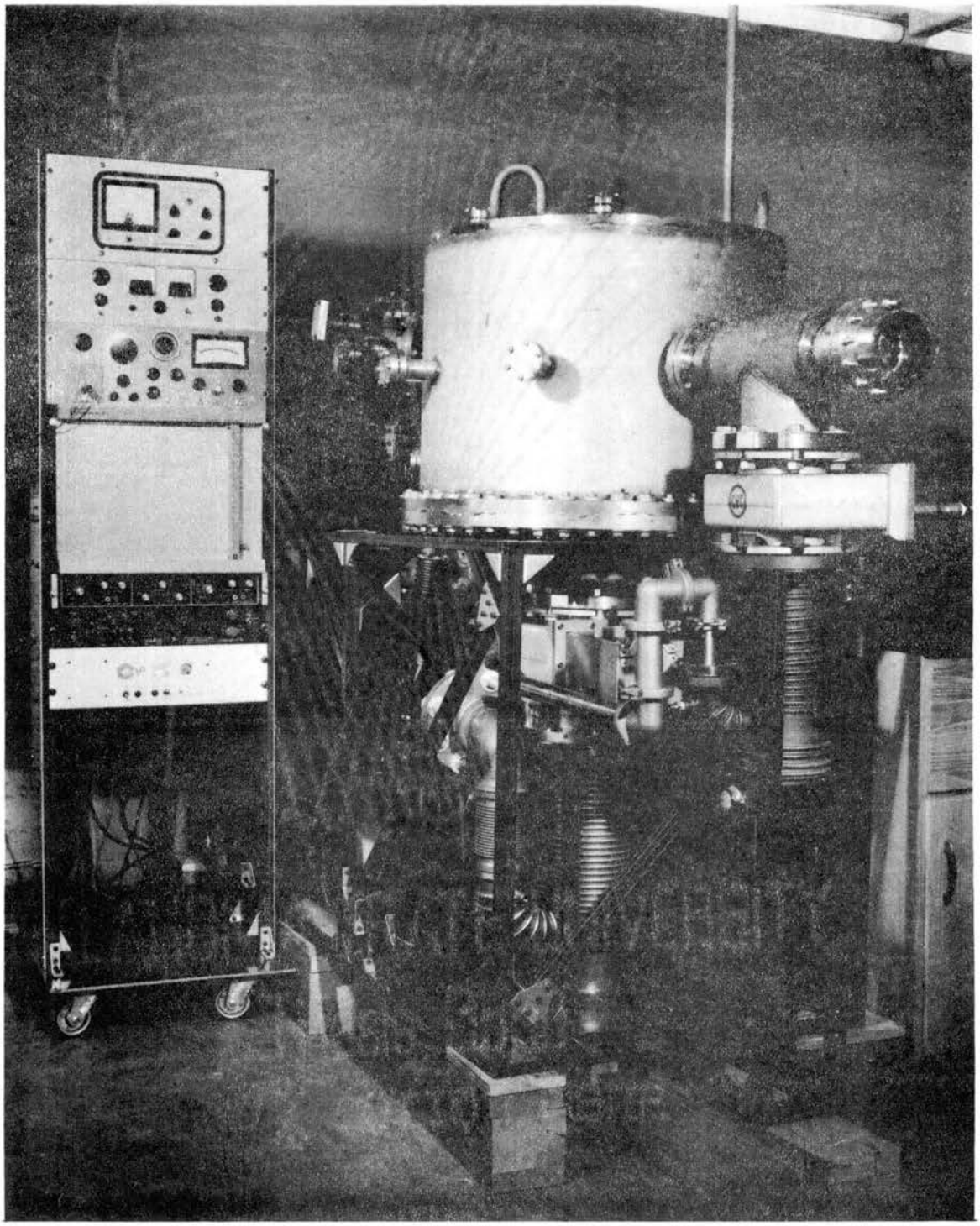

Figure 3. Experimental Apparatus

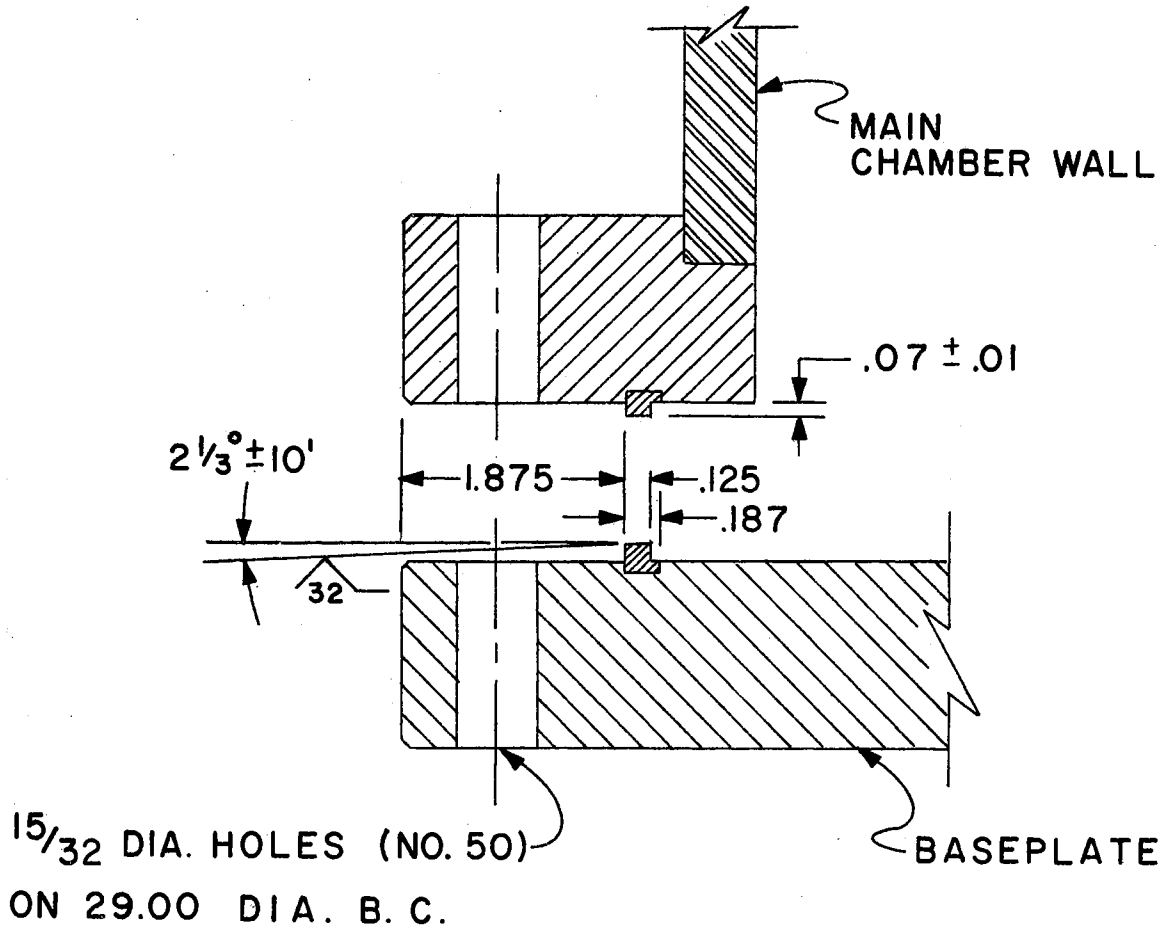

Figure 4. Flange Detail, Main Chamber

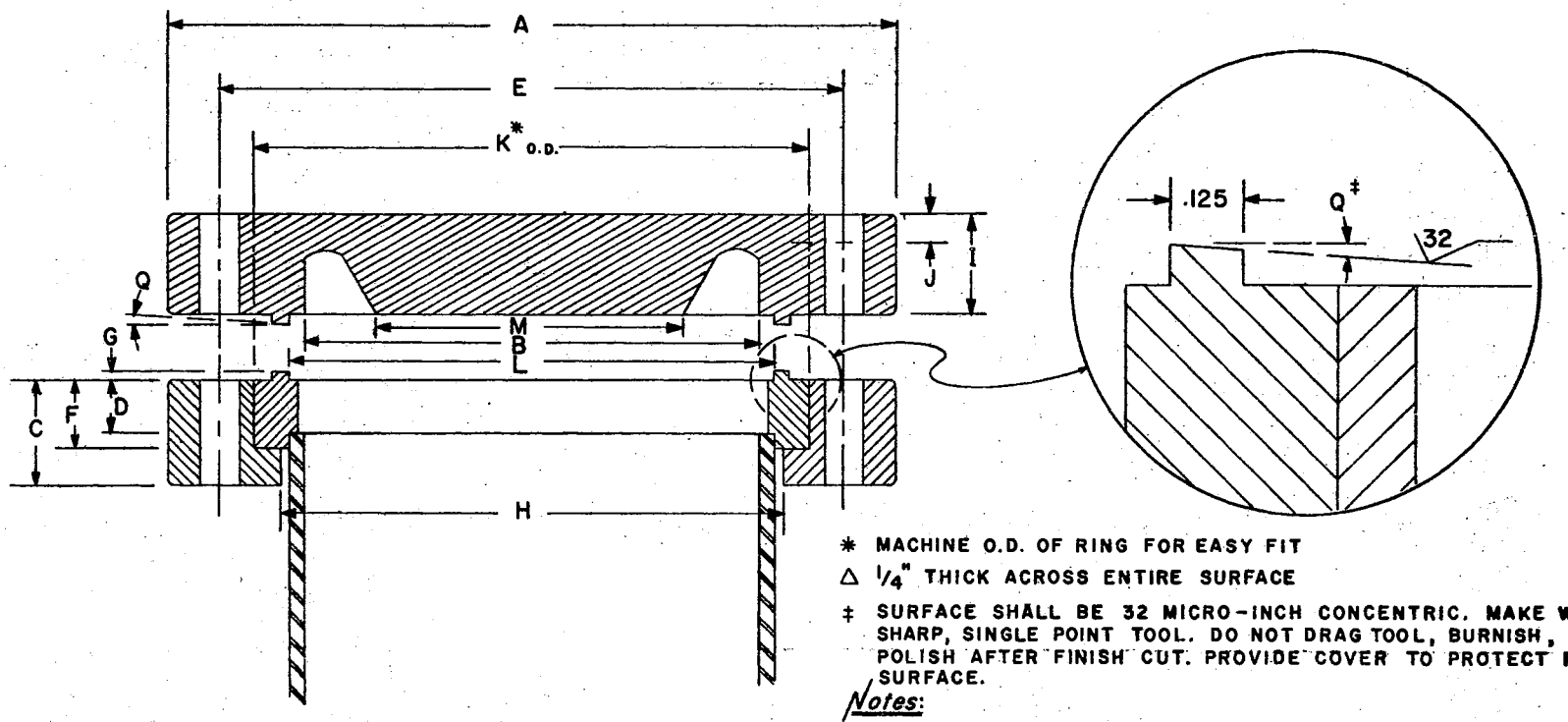

* MACHINE O.D. OF RING FOR EASY FIT

△ 1/4" THICK ACROSS ENTIRE SURFACE

‡ SURFACE SHALL BE 32 MICRO-INCH CONCENTRIC. MAKE WITH SHARP, SINGLE POINT TOOL. DO NOT DRAG TOOL, BURNISH, OR POLISH AFTER FINISH CUT. PROVIDE COVER TO PROTECT FINISHED SURFACE.

Notes:

NOMINAL O.D.	NOMINAL I.D.	A O.D.	B I.D.	C THICK	D SETBACK	E B.C.	F REC DPTH	G HIGH	H CLEAR	I THICK	J WALL	K* O.D.	L KNIFE	M ROUGH DIA.	Q‡ TAPER	BOLT HOLES NO.	BOLT HOLES DIA.
2 3/4	1 1/2	2.750	1.375	.500	.209	2.312	.300	.070	1.530	.550	△.250	1.813	1.500	—	1/2°–3/4°	6	.332
6	4	5.968	3.875	.843	.437	5.128	.563	.070	4.125	.800	.250	4.563	4.000	2.500	3/4–1°	12	.332
8	6	7.968	5.875	.937	.500	7.128	.624	.070	6.125	.880	.250	6.500	6.000	4.250	1 1/2° ±10'	14	.332

Figure 5. Flange Dimensions

design should be noted. Both of the larger flanges and most of the smaller ones have a rotatable, rather than a fixed, bolt circle. Flanges with this design were found to seal just as well as those which had the more conventional fixed bolt circle. The rotatable feature was a great convenience in the final assembly of the experimental apparatus. However, if the molecular beam had an essential geometry to its cross section, and if there were a uniquely-preferred orientation for the beam, flanges with fixed bolt circles would then be preferred. For those flanges with rotatable bolt circles, the machining procedure was specified as follows: (1) rough-out the sealing surface, (2) weld the sealing surface to the tubulation, (3) indicate and finish the sealing land, (4) assemble the flange with the bolt circle, (5) weld the assembly to the chamber. When the sealing surface for a rotatable flange is welded, it tends to warp severely, often as much as 0.5 mm. Thus, the sealing surfaces were finished following the initial welding process. For flanges with a fixed bolt circle, warpage was not a problem. The additional metal containing the bolt circle provides a satisfactory heat sink during the TIG welding process. A further change in the Batzer design was the inclusion of a step 0.318 cm. inside the sealing surface, as shown in the detail of Figure 5. This ledge provides a convenient site for the trimming of gasket material. The presence of the ledge does not adversely affect the essential rotation of the sealing surface about its knife edge point of initial contact.

The only deficiency in the Batzer design is the exposed position of the sealing land. If a radial scratch extends completely across this sealing surface, a large leak will result. Such scratches may be temporarily plugged with a dab of low vapor pressure epoxy (Varian

Torr-Seal). Alternatively, scratches in the smaller flanges may be removed by grinding in situ. To accomplish this grinding, the flange detail can be machined in reverse within a Delrin® blank. Delrin® holds 400-600 grit corundum quite well. The blank may then be turned by hand or with a small drill motor to lap out the scratch.

Several electrical feedthroughs were required to penetrate the vacuum wall. Bolt circles with the Batzer flange detail were welded to excellent 7-pin feedthrough blanks purchased from the General Electric Company. The electrical feedthrough design is shown in Figure 6. Figure 7 shows the heat sink required in welding the electric feedthrough blank to a bolt circle. A heat sink is an absolute necessity to prevent fracturing of the ceramic insulation around the Kovar feedthrough cap.

Rotary feedthroughs were purchased from Cooke Vacuum. These feedthroughs were of the radially bent bellows design, containing no O-ring seals. This design is preferred for ultra-high vacuum systems which are baked out. Two such feedthroughs are required on the main scattering chamber.

2. The Pumping System

The main scattering chamber is evacuated with two oil diffusion pumps which have liquid nitrogen baffles. A six-inch pump and baffle are attached directly to the baseplate of the chamber. A four-inch pump is attached to the chamber with a "T" made from 5-inch nominal diameter stainless steel pipe. At the outer end of this "T" is a viewing port. Both pumps utilize polyphenol ether oil as their working fluid. The liquid nitrogen baffles are filled automatically.

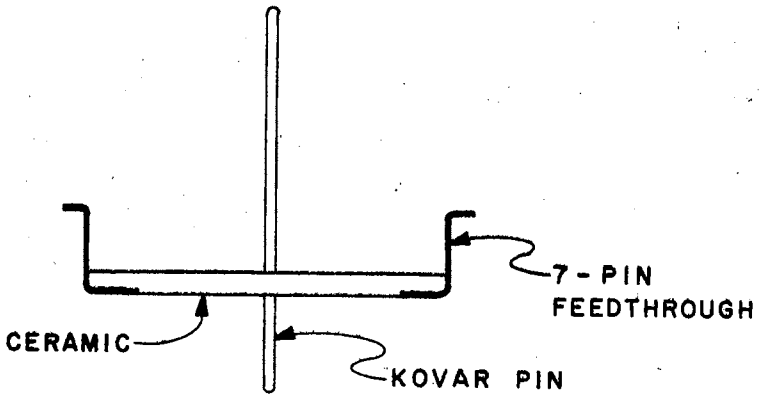

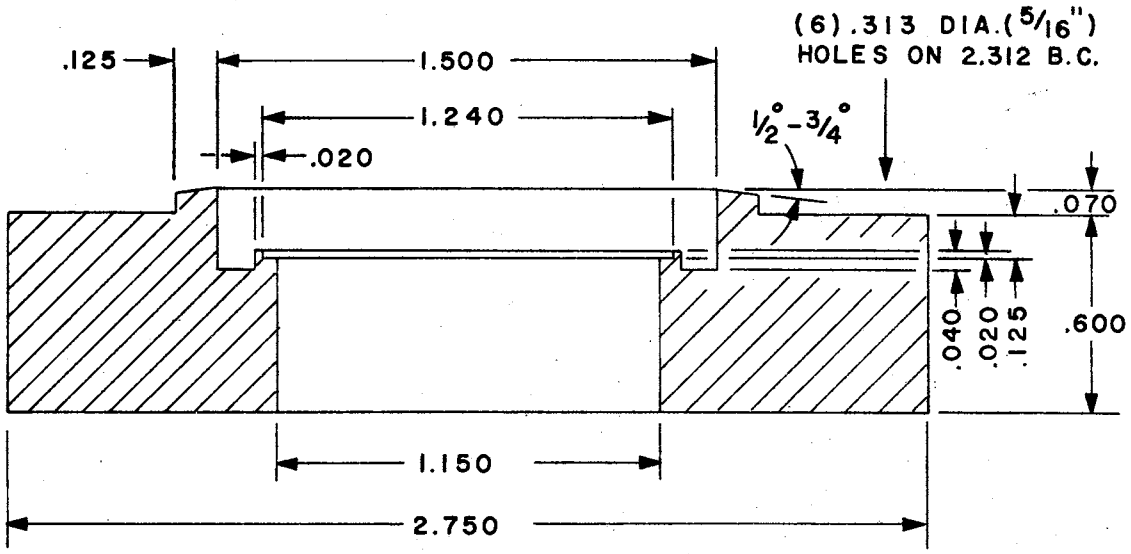

NOTE; TOLERANCE OF ALL DETAILS OF WELDING FILLET ±.005

Figure 6. Electrical Feedthrough

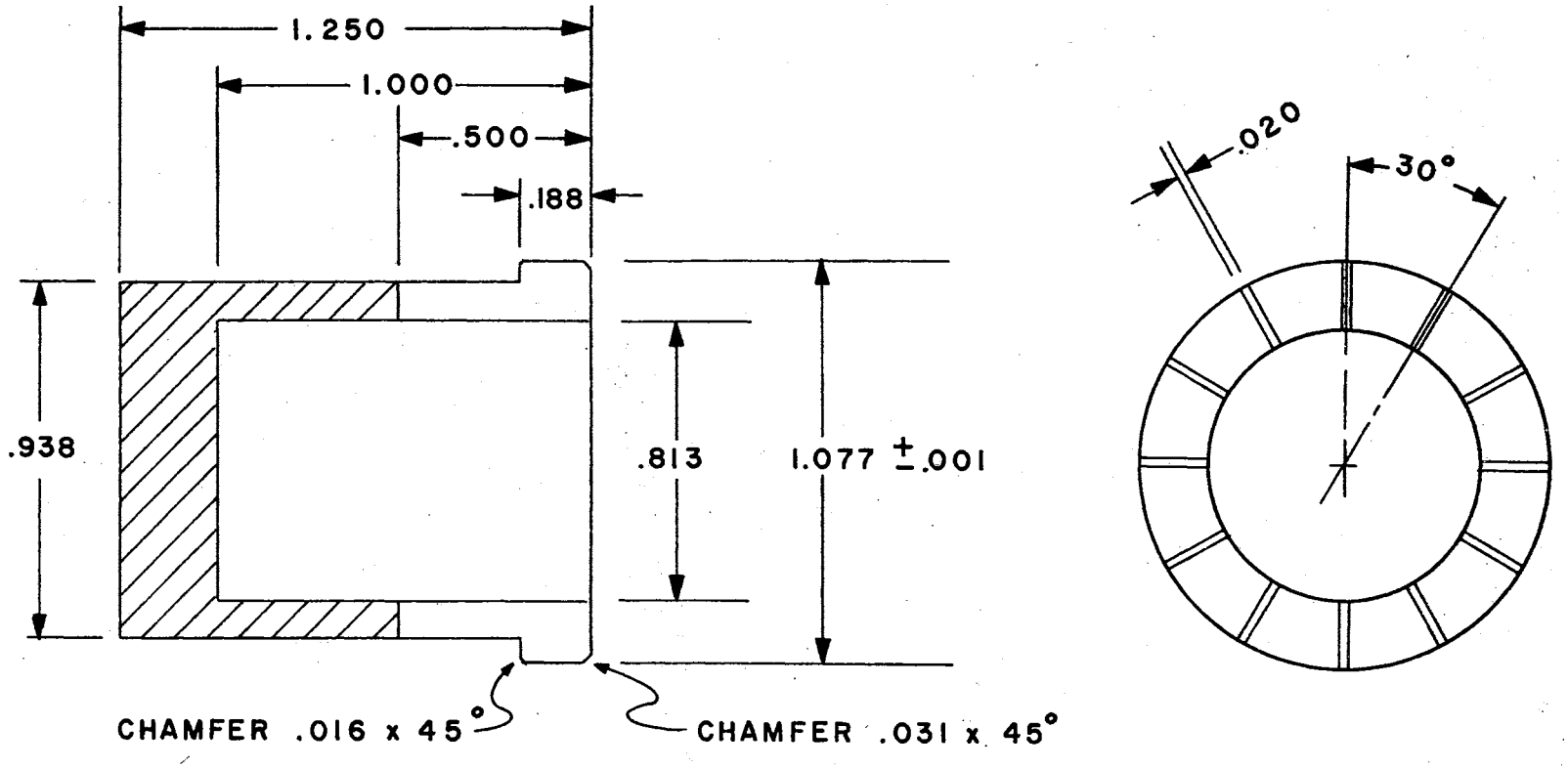

Figure 7. Heat Sink

Foreline connections are Dresser Vacuum TF-100 Twinflangs Unions attached with 4-inch nominal diameter pipe. In each foreline there is a flexible bellows coupling to dampen mechanical vibrations.

Two moderately large mechanical vacuum pumps, working in tandem, provide the forepumping. The pump closer to the diffusion pumps is a Roots-type blower, with a top pumping speed of 85 cubic feet per minute at a pressure of 100 microns. This pump is backed with a compound dual-vane mechanical pump which has a top pumping speed of 20 cubic feet per minute at 10 microns pressure. Together, the two pumps give a very high throughput over a wide pressure range. Pump down time for the entire vacuum system from atmospheric pressure to 5×10^{-4} mm Hg is less than 15 minutes.

The mechanical pumps are surrounded by an enclosure made of ceiling tile cemented to peg board. This provides an effective acoustical baffle for the pumps, which otherwise would be objectionably noisy. Total volume for this enclosure is about 850 liters.

The main vacuum system could be baked at 400°C, but the presence of solid state electronic devices within the vacuum envelope placed an upper limit of about 150°C on the temperature to which the system could be subjected. Bakeout is achieved by wrapping electrical heating tapes around the exterior of the apparatus. With the exterior of the chamber at 150°C, a thermocouple inside the motor on the SDVS was at a temperature of 75°C. After baking overnight, a pressure of 3×10^{-9} mm Hg has been achieved within the main scattering chamber.

Pressure within the vacuum envelope is measured with a General Electric Company "nude" ion gauge. Thermocouple gauges monitor the foreline vacuum.

A framework of Unistrut structural channels supports all the controls for the vacuum pumps associated with the system. This framwork also holds the acoustical baffle around the mechanical pumps. A cross-member on the frame supports the outer end of the beam source chamber.

C. The Beam Source Chamber

Research grade gas from a high-pressure cylinder passes from the supply cylinder through the cylinder regulator. The gas then goes in turn through an inline filter with a pore size of 7 microns, a Varian variable leak, and into the beam source chamber. The chamber is stainless steel throughout, with a total volume of 5.2 liters. Two oil diffusion pumps with a combined pumping speed of 390 liters per second evacuate the source chamber.

The nozzle source design, shown at 180 x magnification in Figure 8, follows that of Moran[15,16,140] with a few modifications. The source is 3 mm o.d. quartz tubing with a 1 mm thick wall. Each nozzle was made by cutting the tubing to the desired length, then fire polishing one end until an orifice of the desired diameter was achieved. As the fire polishing progressed, the orifice diameter was estimated by passing a finely-drawn tungsten wire through the end of the tube. In this way, a selection of nozzles with orifice diameters from 0.0120 mm to 0.0350 mm was easily attained using a gauge wire with a diameter of 0.023 mm. Final diameters were measured with a machinist's microscope which had a double micrometer stage precise to one-ten-thousandth of an inch. For the tests described herein, only nozzles with an orifice of $0.025 \pm .003$ mm were used.

The nozzle is held with a Cajon Ultra-torr tube fitting. The

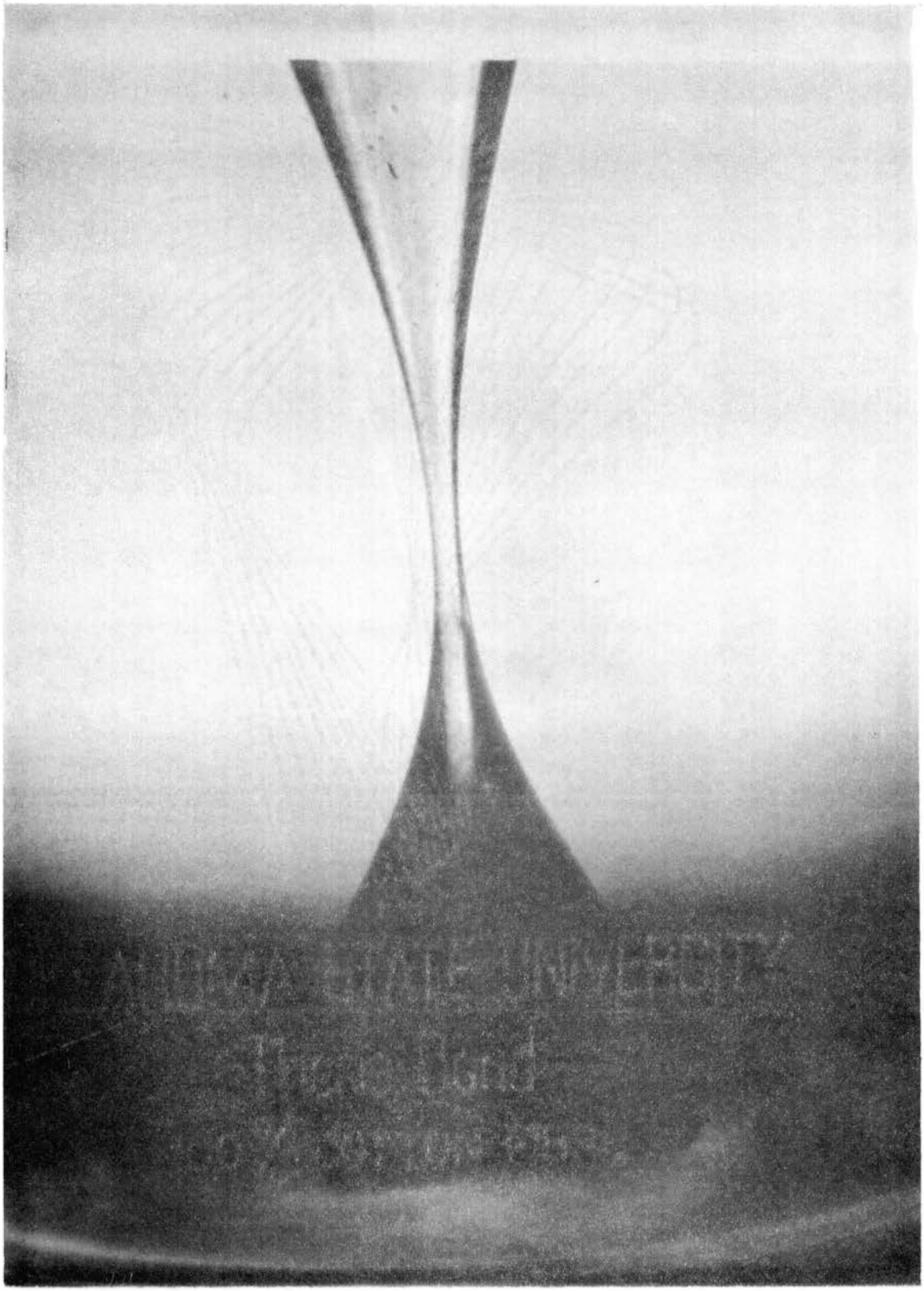

Figure 8. Quartz Nozzle

nozzle holder, shown in Figure 9, slides in a track of kinematic design that insures only one degree of freedom for the nozzle tip. The lateral position of the nozzle is then precisely controlled from outside the beam source chamber through a linear feedthrough in the vacuum wall. One turn of the feedthrough handle displaces the nozzle tip by 0.127 cm.

The nozzle holder has a window at its rear end. There is an intense lamp just behind this window. The light from the lamp may be observed in the view port of the main scattering chamber during the course of an experiment.

The beam source chamber and main scattering chamber have a single open area in common: the collimating orifice. The diameter of this orifice is 0.457 mm. The orifice was drilled in a circular coupon 0.30 mm thick. The nozzle-collimator distance is typically 0.762 cm. Beam width is shown in Figure 10. Unfortunately, the detector admittance port is larger by about 2x than is the beam at the detector and a precise measurement of the extent of the beam divergence is not possible. The beam is 0.17 cm wide at the target. A nichrome filament is wrapped around the barrel of the quartz nozzle so that the mean energy of the gas beam may be increased.

Good vacuum practice would dictate that the beam chopper be located in its own differentially pumped buffer chamber. That procedure would assure that a minimum of background gas from the source chamber would pass through the chopper and enter the main scattering chamber. Such a gas "leak" would tend to impart a very undesirable coherent character to the background gas within the larger chamber. However, it proved impractical to provide for a buffer chamber and its associated pumping system and yet keep the nozzle source sub-assembly to a manageable size.

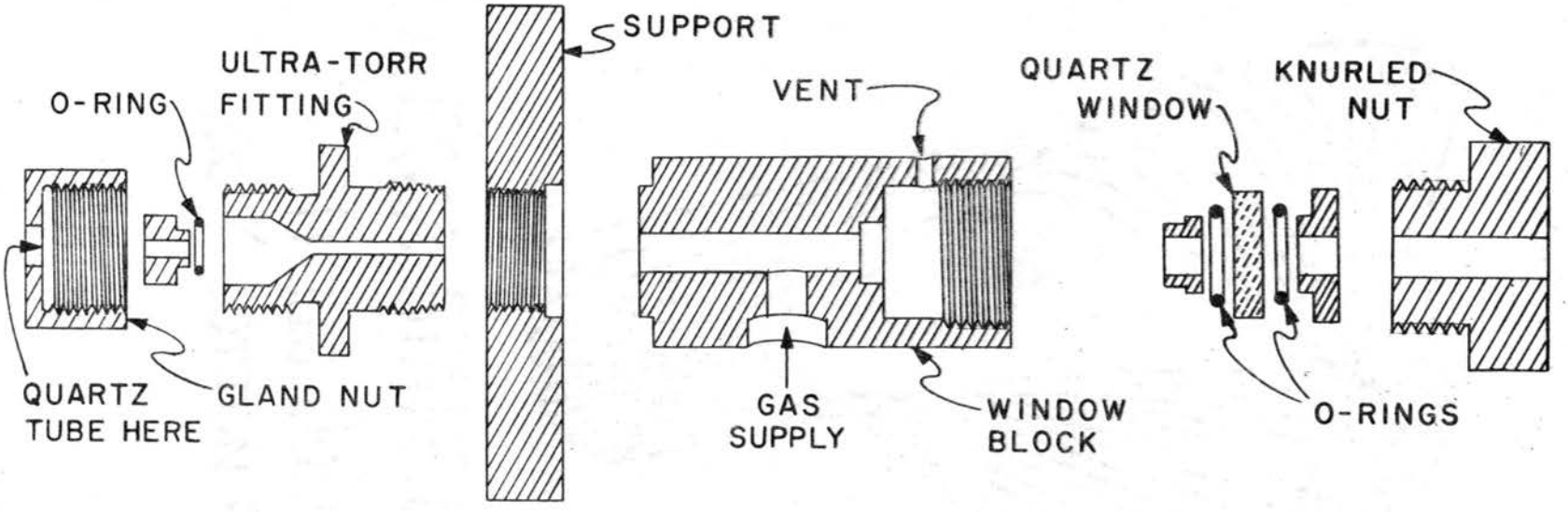

Figure 9. Nozzle Source Holder

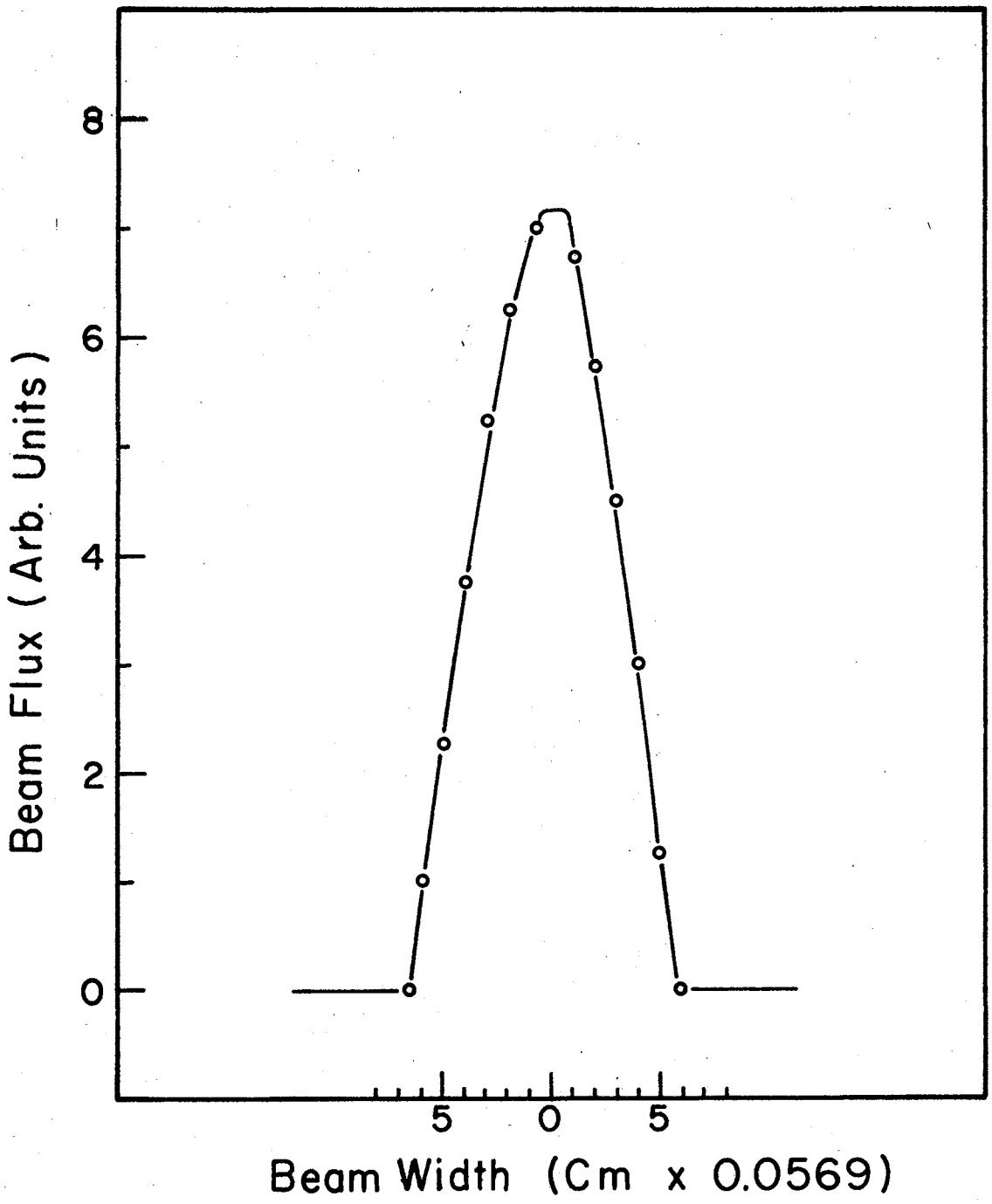

Figure 10. Nozzle Beam Width

The beam chopper is located on the downstream side of the beam collimating orifice, 8.5 mm from the bulkhead separating the two chambers.

Coherence in the background gas in an experiment which incorporates a nozzle source is not the problem that it is for experiments employing an effusive source. There is a very large difference in flux between these two basic types of source that is easily distinguishable at the detector. Nozzle sources of the design employed herein will typically have a flux of approximately 4×10^{17} particles per steradian per second.[140] Effusive sources with a similar orifice diameter have a flux of 1×10^{16} particles per steradian per second. Moreover, the velocity distribution characteristics of particles coming from each source are dramatically different. Nozzles sources have a velocity spread of about 10% or less and are much more energetic than effusive sources. Therefore, it is easy to distinguish between the particles in the gas beam and the particles that come from the background of the beam source chamber. The latter have such a low flux that they scarcely appear at the detector with the particles that are in the gas beam proper.

The beam is chopped at a frequency of 25 cycles per second using a two-vane mechanical chopper supplied by American Time Products (Bulova). This chopper is analogous to the device employed in an "Accutron" wristwatch. Two rectangular vanes, roughly 8 mm by 15 mm, are attached to the end of the tines of a tuning fork. Between the tines is a relatively large electromagnet which has two windings, a driver coil and a pick-up coil. The slightest shock starts the tines oscillating at their fundamental frequency. This creates a signal in the pick-up coil that is amplified and returned to the driver coil in

proper phase to make the tines vibrate with the desired amplitude. The amplifier is a simple solid-state device located outside the vacuum system. The pick-up signal is available at the amplifier for use as a lock-in reference.

The chopper used in this work is significantly different from the ones used in time-of-flight (TOF) determinations. For the TOF experiment it is essential to employ a chopper which has a sharp and well defined shutter function with a rise time very fast relative to the mean speed of the particles being chopped. Velocity dispersion will cause each chopped packet of gas particles to lose some of its coherence during the flight from the chopper to the detector. Typically, the chopper will have a triangular shutter function with a total open time (base) of 125 micro-seconds. These requirements would preclude the use of a tuning fork type chopper and its sinusoidal shutter function. Such stringent wave form requirements are not necessary when a slotted disk velocity selector is used for velocity determinations.

The tuning fork beam modulator suffers from one fault. When it is subjected to elevated temperatures, its fundamental frequency is altered sufficiently that the amplifier/drive will no longer maintain vibrations with amplitude adequate to interrupt the beam. At that point, the beam is no longer modulated, and the lock-in amplifier looses its reference. A light-weight tantalum shield protected the tuning fork drive coils and tines from the intense radiation experienced during the target heating cycles. An alternative method would be to power the tuning fork with a variable frequency drive and adjust the lock-in amplifier filter accordingly. In this way, modulator performance could be optimized in the likely event that the radiation shield was

not completely effective.

D. The Target Holder

Targets of metal foil 1.27×10^{-2} mm thick are held under a slight spring tension by two electrode clamps. The target is 14.92 cm from the nozzle collimating orifice. The targets are heated by passing 60 cycle a.c. through them. The total exposed target area is 1.73 cm by 1.59 cm. A current of 36 amperes at 2.2 volts heats the target to 1320°K. During the experiment, temperature of the target is measured with an optical pyrometer certified by the National Bureau of Standards. The precision of this method is $\pm 8^{\circ}$K.

The target foil clamps are supported with a single gimbal. The axis of rotation for this gimbal passes through the aiming point on the target and lies in the horizontal plane described by the nozzle and the detector assembly. Rotation of the target about this axis established the out-of-plane angle of incidence, Φ_i, and the out-of-plane angle of reflection, Φ_r, for the gas beam. This rotation cannot be accomplished from outside the chamber.

The target gimbal bracket is hung by a vertical rod from the ceiling of the main scattering chamber. This rod lies along the central axis of the scattering chamber. The rod may be turned from outside the chamber with a rotary feedthrough. Rotation of the rod establishes the in-plane angle of incidence, θ_i, for the gas beam. The angular resolution for the in-plane angle of incidence is 0.1°. The setting of θ_i may be monitored through two small view ports in the main scattering chamber. The index for the angle of incidence and the alignment of the entire speed selector and target assembly was checked

using a small laser, a cathetometer precise to $\pm$ 0.001 mm, and a mirror clamped in the target holder.

The targets are treated according to the method of Germer and May[136] as modified by Yamamoto and Stickney.[93] Targets were aged at ~1300°K in an atmosphere at 2 x 10^{-7} mm Hg, with periodic flashes to 2000°K.

E. The Speed Selector and Detector

The slotted disk velocity selector (SDVS) is from the basic design of Hostettler and Bernstein[141] (HB) with a few modifications. For this work particles that pass through the SDVS have their direction of travel specified by the orientation of the detector admittance orifice both in-plane (θ_r) and out-of-plane (Φ_r). Thus, the SDVS is a "speed" selector instead of a "velocity" selector. Six aluminum disks 1.59 mm thick and 16.0 cm diameter are clamped on a shaft that is attached to a hysteresis synchronous motor. The disks have rectangular slots 0.795 mm wide with a radial length of 7.95 mm. Each disk is clamped in a strategic location on the rotor shaft where it will remove the higher order speed side bands from the gas beam. Resolution for this speed selector is 4.6%. The maximum linear speed that the SDVS will pass is 1.5 x 10^5 cm/sec. The disks have 280 teeth instead of the 278 used by HB.

Trujillo notes that a great saving in the mass of SDVS mount may be achieved if the axle of the speed selector rotor is allowed to find its own axis of rotation. He accomplishes this by spring-loading the bearings at each end of his rotor. However, with this bearing support there are certain rotational speeds, generally low, at which the speed

selector assembly bounces. These frequencies are obviously the natural vibrational frequencies for the loading springs. A mass reduction in the rotor mount is more conveniently accomplished simply by dynamic balancing of the selector. A two-plane (dynamic) balancing technique must be employed rather than a one-plane (static) technique. This is because of the high rotational speed and appreciable moment of inertia of the rotor. The speed selector rotor was balanced with a tolerance of less than 5.0 microinches total vibrational runout in the center of the rotor shaft at 24,000 revolutions per minute.

The speed selector rotor is coupled to its driving motor through a flexible steel spring wire shaft. The motor is a 400 Hz, 3-phase, hysteresis synchronous motor with Barden Bar-temp (dry lubricated) bearings. The motor, of course, receives its power from outside the vacuum changer. Hostettler and Bernstein, as well as Trujillo, use a variable oscillator, capacitor bank (phase shifter), and power amplifier to attain a reasonably pure 3-phase current to power their SDVS motor. With this arrangement, the power output at the amplifier is independent of the frequency of operation. An alternate, and considerably less expensive method of supplying 400-cycle, 3-phase current to the SDVS is employed in the present work. A simple motor-generator set (MGS), similar to that used in tachometer installations, is utilized. A Variac supplies 120 volt alternating current to a heavy-duty rectifier and LC filter circuit. The essentially ripple-free direct current that comes from the filter then passes to the field windings of the MGS. The Variac can alter the voltage supplied to the MGS and regulate the generator frequency of the MGS. As the frequency of the current supplying the speed selector varies, the angular velocity of

the speed selector rotor varies. Obviously, the total power output of the MGS is diminished when it operates at less than full speed, but the SDVS requires very little power for operation in a vacuum.

For those particles which pass from the rear of the speed selector and enter the detector, linear speed is a direct function of the angular velocity of the speed selector rotor. Specifically, the speed in centimeters per second of the gas particles which successfully pass through the teeth of the SDVS is a factor 6.22 times the angular velocity of the rotor in revolutions per minute. It is thus essential that the turning rate of the SDVS be monitored continuously and precisely during an experiment. Most experimenters have employed some sort of photocell device to accomplish this. However, for the present work, it was sufficient merely to monitor the output of the MGS. This was accomplished by following two of the three motor windings with a digital frequency meter (General Radio Company, Type 1151-A). During an experiment, the MGS was accelerated to the desired speed, then the MGS power supply was turned off. The frequency meter measures the slowly decreasing angular velocity of the SDVS. The meter is sensitive to the signal generated by the motor as it coasts to a stop.

All time-of-flight measurements of energy accommodation have relied on a single rotating disk to modulate the beam. Chopping frequencies in these measurements have been moderately high (3KHz) to decrease loss of coherence in the signal as a result of speed dispersion during the flight of the particles. Thus, it is difficult to employ both mechanical speed selection of the gas particles and beam modulation in a time-of-flight measurement of accommodation, because of the rather involved phase relationships within the gas beam signal

which are imparted by what amounts to two independently functioning beam choppers. At maximum speed, the SDVS modulates the beam at 112 KHz. The uncertainty in the location of the wavefrount for each beam packet would greatly increase the ambiguity in a time-of-flight measurement of energy accommodation.

The frame of the velocity selector is .208 cm thick aluminum. The rotor bearing brackets are 1.27 cm thick stainless steel. The top of the portal on the SDVS lies .238 cm above the center line of the gas beam. The bottom of the acceptance channel of the SDVS is .556 cm below the beam center line. The first disk of the SDVS is 10.16 cm from the aiming point on the target surface.

The SDVS is mounted on a heavy turntable .953 cm thick and 62.9 cm in diameter. Underneath the turntable is a ring of stainless steel into which is machined a deep groove. On the baseplate of the main scattering chamber is an identical groove. Loose ball bearings 1.27 cm in diameter fit in the mated grooves and provide a simple thrust bearing on which the SDVS pivots. To reduce friction, the balls are dusted with niobium diselenide, a dry lubricant that is an electrical conductor.

Position of the SDVS turntable is controlled from outside the main scattering chamber with a bellows type rotary motion feedthrough. A gear rack runs around the periphery of the turntable and meshes with a pinion gear turned by the feedthrough. There is a 16-2/3:1 gear reduction in the rack and pinion. The SDVS can be located with a precision of $\pm 0.1^{o}$ of arc.

The disk assembly of the SDVS was clamped in the proper orientation and a pair of holes 1.58 mm in diameter were drilled through all

six disks. These holes lay along a diameter of the disk ensemble, just inside the slot cuts. With these holes and a small laser, the entire assembly can be checked for alignment. Specifically, it may be ascertained that the SDVS revolves about the center of the main chamber, that the aiming point of the target lies on the major axis of the main chamber, and that SDVS slots are orientated toward the target aiming point. Finally, the beam collimating orifice can be checked for proper position.

1. The Detectors

The detectors are mounted 33.0 cm from the target surface. Each is a miniature ion gauge. A glass envelope 10 mm inside diameter and 25 mm long is cemented with epoxy over each detector. In the side of each envelope is a tubulation 4 cm long and 1 cm diameter.

The detector used for determining speeds of the scattered particles is mounted directly behind the SDVS. This detector intercepts particles that pass the SDVS disks. The detector used in measuring spatial distributions of scattered particles is adjacent to the speed selector. The entrance canal in this second detector lies in the same geometric plane as the beam source, the aiming point on the target, the entry to the SDVS, and the entry to the first detector. The path into the spatial distribution detector is displaced 21.5° from the channel in the SDVS. Both detectors rotate about the aiming point on the target.

F. The Detector Electronics

Each detector is powered from a single supply outside the vacuum chamber. For a maximum signal using an argon beam, a grid voltage of + 160 volts is employed with a filament bias of + 26 volts. An emission current of 0.60 to 0.80 milliamperes is typical. The power supply consists of three independent, ripple-free, direct current sources (Lambda Electronics Corporation) that are individually regulated. Although there exists no regulation in the emission current-filament supply circuit, the circuit possesses sufficient stability to remain drift-free over the course of an experiment.

Immediately adjacent to each detector is a preamplifier. This circuit is essentially the one employed by Yamamoto and Stickney[93], combining low amplification with an impedence shift.

The signal generated by the beam at the detector consists of a small alternating current imposed on the top of a much larger direct current coming from the background gas. After passing the preamplifier stage, the a.c. signal passes into a lock-in amplifier, Model HR-8, purchased from Princeton Electronics Corporation. This device amplifies and filters the signal, then compares that signal with the reference generated at the mechanical beam chopper. The lock-in amplifier output is a $\pm$ 10-volt signal that is proportional to that fraction of the input signal which has the same frequency as that of the reference. The output appears across a capacitor bank. The size of the bank may be altered to modify the dynamic response (time constant) of the instrument.

This lock-in amplifier has a sensitivity of 10 nanovolts, but

typical signal strengths were of the order of tens of millivolts for the spatial scattering distribution measurements. The zero signal level may be suppressed by up to an order of magnitude to conveniently display very small changes in large signals.

The phase angle between the chopper reference signal and the beam was found to be approximately 7^{o}. This lag in the beam signal arises from the finite length of time required by the gas particles in the beam to traverse the chamber and enter the detector after they have passed through the beam chopper.

The output from the lock-in amplifier goes to the ordinant of an x-y plotter (Electro Instruments, Model 520). For the spatial scattering distribution measurements, the signal to the abscissa arises from a simple potentiometer circuit attached to the rotary feedthrough that drives the detector turntable around the target. When the speed distribution of particles in the beam is measured, the abscissa is a time base. A typical speed distribution measurement requires about 45 minutes. The signal may be displayed on an oscilloscope connected to the lock-in amplifier.

CHAPTER III

RESULTS AND DISCUSSION

A. Distribution of Particle Speeds in The Beam

All of the tests involving a tungsten surface were conducted using an argon beam that had been generated with a quartz nozzle. In most tests, the beam was extracted from a body of gas in thermal equilibrium at $300^{\circ}K$. The detector employed in all tests of particle speed distribution was sensitive to the total particle flux entering the detector envelope. However, the presence of the slotted disk velocity selector, interposed in the path of the beam before the detector opening, allowed evaluation of the number density distribution of particle speeds as well.

The relative spread in the flux and number density distributions is indicated by what is defined as the speed distribution:[16]

$$(SD) = \left(\int P_n(v) \ (v-\bar{v})^2 \ dv \ / \ \int P_n(v) dv \right)^{\frac{1}{2}} \frac{1}{\bar{v}} \qquad (9)$$

This is the root-mean-square deviation in particle speed divided by the mean speed of all particles in the beam. For an ensemble of particles in thermal equilibrium (Maxwellian speed distribution), this equation yields a value of 0.363. The factor $P_n(v)$ contains the particle distribution per unit volume and $\bar{v}$ is the mean speed of particle flux in a differential solid angle of the beam.

Initially, it was necessary to establish that the nozzle beam and the detector electronics remained stable for a period of time longer than that required for a series of measurements. As a check of instrument stability, the distribution of particle speeds in the nozzle beam was measured repeatedly during the course of these tests. The most sensitive measurement that could be accomplished was the repeated checking of particle speeds centered about the most probable speed. The general procedure was to establish flow in the nozzle while the detector electronics warmed up and stabilized. The background pressure in the nozzle chamber was used as an estimate of nozzle throughput. When this background pressure reached a constant value, usually 4.0×10^{-4} mm Hg, the SDVS would be accelerated to the desired angular velocity. Lock-in amplifier signal strength output was recorded while the speed selector gradually slowed down.

The day-to-day reproducibility of the total signal strength in the measurements centered about the most probable speed demonstrated that the instrument had satisfactory long-term stability. The results are summarized in Table I. These data were generated over a five-week period. With reference to Table I, data in line 1 represent the average of twelve SDVS runs made during a preliminary testing period lasting about two weeks. For each of the twelve runs, the most probable speed was the same. The magnitude of the signal strength, when corrected to a constant detector emission current, remained constant within two percent.

The nozzle gas supply was then altered slightly. These modifications involved the addition of a heating coil and thermocouple to the outside of the quartz tube behind the nozzle orifice. Data in line 2

of Table I represent the average of two runs made immediately following the modification. Unfortunately, the differences between the values in line 1 and line 2 cannot be rationalized in terms of the apparatus modifications alone. It is thought that the temperature of the body of gas from which the beam was drawn remained constant (ca. 300°K) over this period. Gas source pressure was constant throughout for the data in lines 1 and 2.

TABLE I

SPEED DATA. QUARTZ NOZZLE BEAM

Test No.	Maximum Signal (Millivolts)	Number Average Speed (cm x 10^4)	Speed Distribution	Most Probable Speed (cm x 10^4)	Nozzle Temperature (°K)
1	1162	5.60	0.0847	5.49	300
2	623	6.13	0.1261	6.15	300
3	526	6.15	0.1089	6.25	300
4	399	8.27	0.1385	8.27	580
5	24.5	11.14	0.1352	11.20	960
6	526	6.05	0.1155	6.15	300

The total nozzle flow was then decreased for the remainder of the tests. Line 3 in Table I is the data for one SDVS run taken at the start of these final tests. Line 6 is the average of the last three runs made on the SDVS at the conclusion of all tests. The agreement is quite good. Lines 4 and 5 are averages of three runs each made at

elevated nozzle temperatures near the conclusion of testing. They clearly show the expected result, that particle speed in the beam is a function of the temperature of the body of gas from which the beam is extracted. These data strongly suggest that the bulk temperature of the gas was significantly higher than thought for the tests represented by lines 2, 3, and 6 in Table I. Similarly, the most probable speed in the beam was consistently greater than the average speed for all tests except for the ones done initially. This provides further evidence that the alterations made in the gas beam supply were more profound than imagined. Neither most probable speed nor average speed for the particles in the gas beam is a linear function of $T^{\frac{1}{2}}$ for the gas body from which the beam is extracted. It is interesting to note that the spread in the speed distribution of the particles in the beam does not increase appreciably with temperature. The distribution of particle speeds in this beam is far more narrow than that for a gas beam that originates in an ideal effusive source where the distribution of particle speeds is Maxwellian.

Some difficulty was encountered in the detailed analysis of the distribution of particle speeds in the argon beam. These difficulties were traced to design shortcomings and they ultimately prevented the determination of the particle speeds in a beam that was reflected from a surface. The problem could be largely attributed to two sources: mechanical noise arising from operation of the SDVS and a slight misalignment in the detector opening.

The lock-in amplifier was sensitive to the signal-to-noise ratio at the output of the detector preamplifier. However, the noise found at the preamplifier output was not constant, but increased with the

angular velocity of the SDVS. To a first approximation, this source of noise was a linear function of SDVS rotor speed. There were, however, resonant frequencies in the SDVS rotor which would overwhelm the signal for a time long compared with the time constant in the lock-in amplifier output. The result would be seen as a precipitous drop in the recorded output, even though the true signal or information from the experiment was changing only slightly. The opening of the detector was inadvertently placed a very slight distance above the disks of the SDVS. The result of this error was seen as an appreciable signal even when the SDVS was standing still.

A typical recording of the output from the lock-in amplifier made during a test with the SDVS is shown in Figure 11. These data were graphically smoothed to remove the short-term perturbations in the output that result from resonance in the SDVS rotor. Data points from the smoothed output were entered in a computer program which corrected the output to a constant detector emission current. The program then calculated the estimated contribution to noise arising from operation of the SDVS. This linear function is subtracted from the smoothed and corrected data to yield plots of the type shown in Figure 12.

The technique described above was not successful when applied to measurements made on the argon beam after it had collided with the surface. In this instance, the actual signal was less while the noise arising from the SDVS remained the same as in tests on the undeflected beam. The signal-to-noise ratio decreased to a level where the lock-in amplifier could not sensitively distinguish the true magnitude of the signal and yet have sufficient dynamic response to satisfactorily

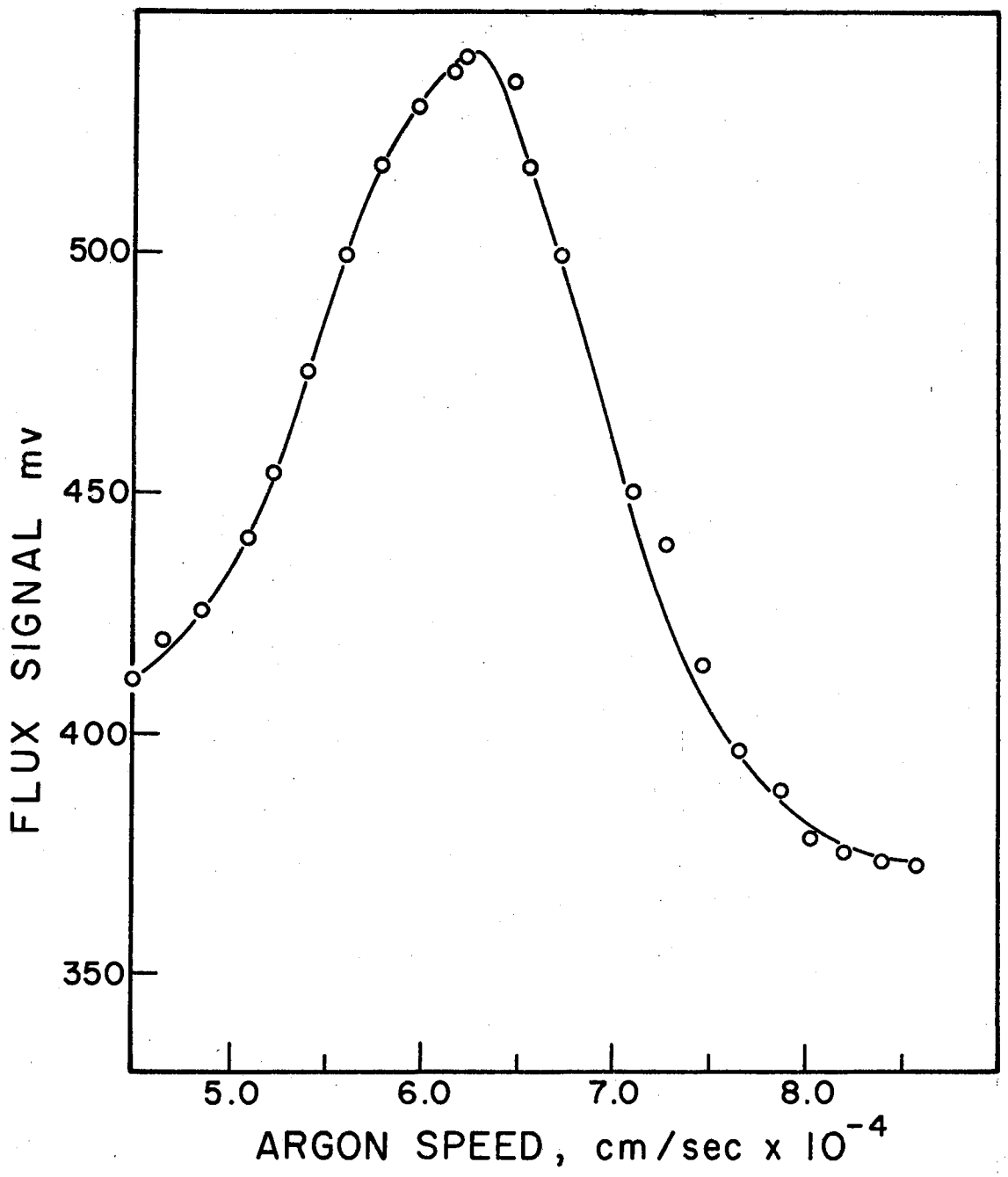

Figure 11. Uncorrected Flux Signal From Quartz Nozzle

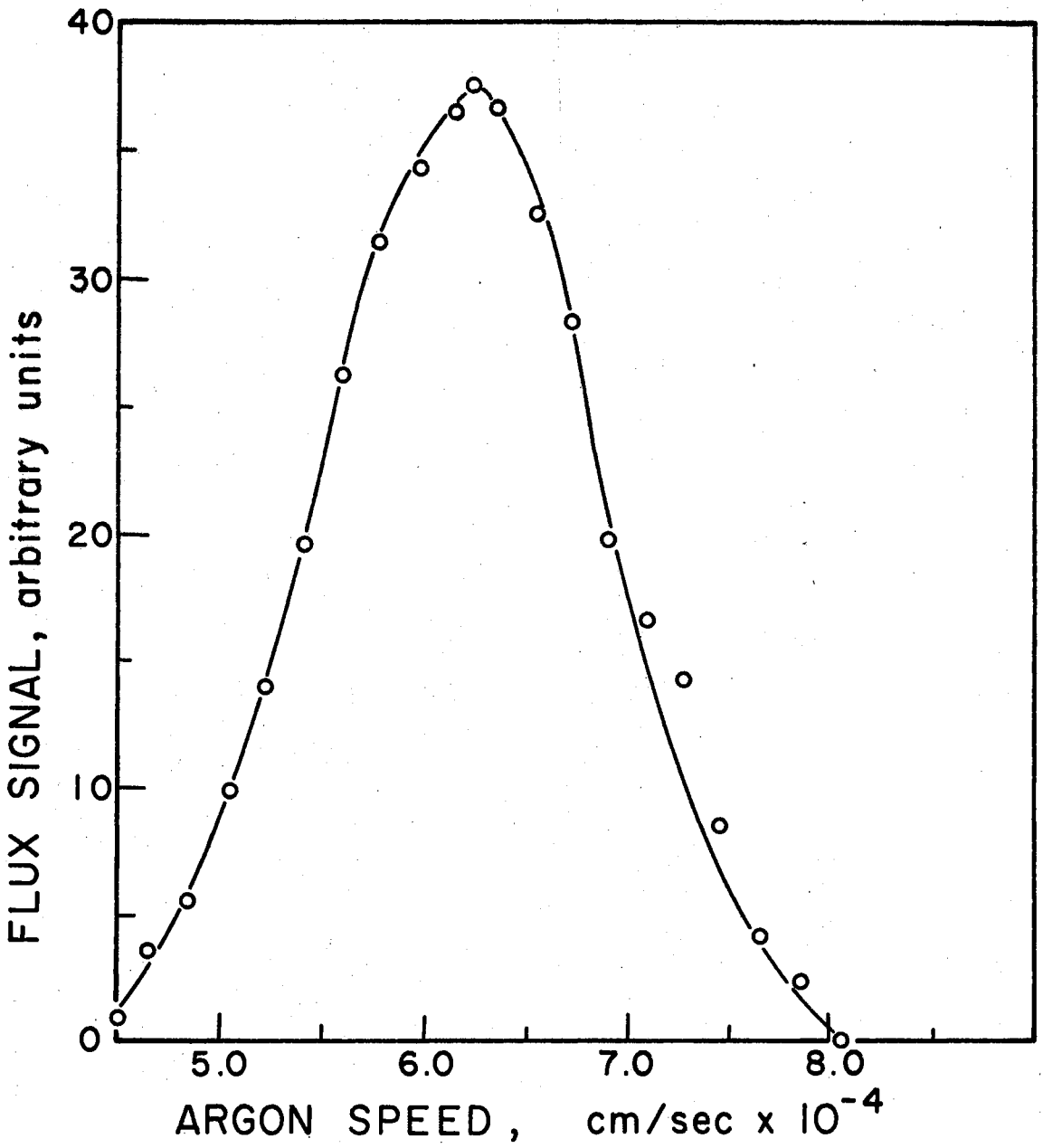

Figure 12. Corrected Flux Signal From Quartz Nozzle

determine how the signal varied as a function of the angular velocity of the SDVS rotor. The solution to this dilemma would be found in a SDVS power supply that could maintain the disk rotors at some constant angular velocity for a significant period of time, about 250 seconds, which would be long relative to the time constant of the lock-in amplifier. In this fashion, an average over the random noise in the system would yield satisfaceoty results.

An additional improvement in signal-to-noise ratio might be gained by clamping the detector in a dynamic suspension. Random vibrations, arising at the SDVS bearings, would be dampened and the detector would not tend to act as a microphone. Further amplification of the signal, as a route to improved signal-to-noise ratio, does not seem to hold much promise, since it seems the noise sources are intimately associated with signal generation. There now exists more than ample signal strength.

Some additional collimation of the reflected beam would decrease the "noise" that results when particles are reflected toward the detector off the upper regions of the target from above the plane containing the nozzle source, the target and the detector. These particles, in their downward trajectory, were not effectively screened by the velocity selector, and consequently appeared in the detector output even when the SDVS was at rest.

B. Spatial Distribution of Particles Scattered from a Surface

The bulk of data in this work involved measuring the spatial distribution of an argon beam scattered from a hot tungsten surface.

Figure 13 shows some typical data. The ordinant is signal strength (flux) measured in millivolts output at the lock-in amplifier. The abscissa is angle of reflection measured from the target normal. The surface temperature is 2100°K measured with an optical pyrometer. The angle of incidence taken in the plane of the beam and the target normal is 50°, while the out-of-plane angle of reflection is 0°. For this plot, the emission current of the detector was 0.72 milliamperes, and the time constant of the lock-in amplifier was three seconds.

It is seen that some hysteresis is evident in the two traces. Data was taken by cranking the detector turntable by hand at a nearly constant rate, typically about one degree per second (~90 seconds per scan). Each plot thus consisted of two scans, one at increasing angle and one at decreasing angle of reflection. Since the lock-in amplifier had a finite and significant response time, as determined by its time constant, some fixed amount of hysteresis is to be expected. The greatest difference in the two traces occurred where the slope of the trace was the largest. This was never greater than about 5 millivolts in a total signal of 50 millivolts. The trace had its largest slope at angles of reflection above 60°, where the signal diminishes rapidly. This region is removed from those angles of reflection where significant structure is seen in the output trace.

Except where noted, plots shown in this paper are the average of two scans. The traces given by the x-y plotter were smoothed and interpreted at intervals of seven degrees (angle of reflection). It was then necessary to normalize each trace to a constant emission current. Figure 14 was used to perform this normalization. Duplicates of the data plotted in Figure 14 were taken several times during the

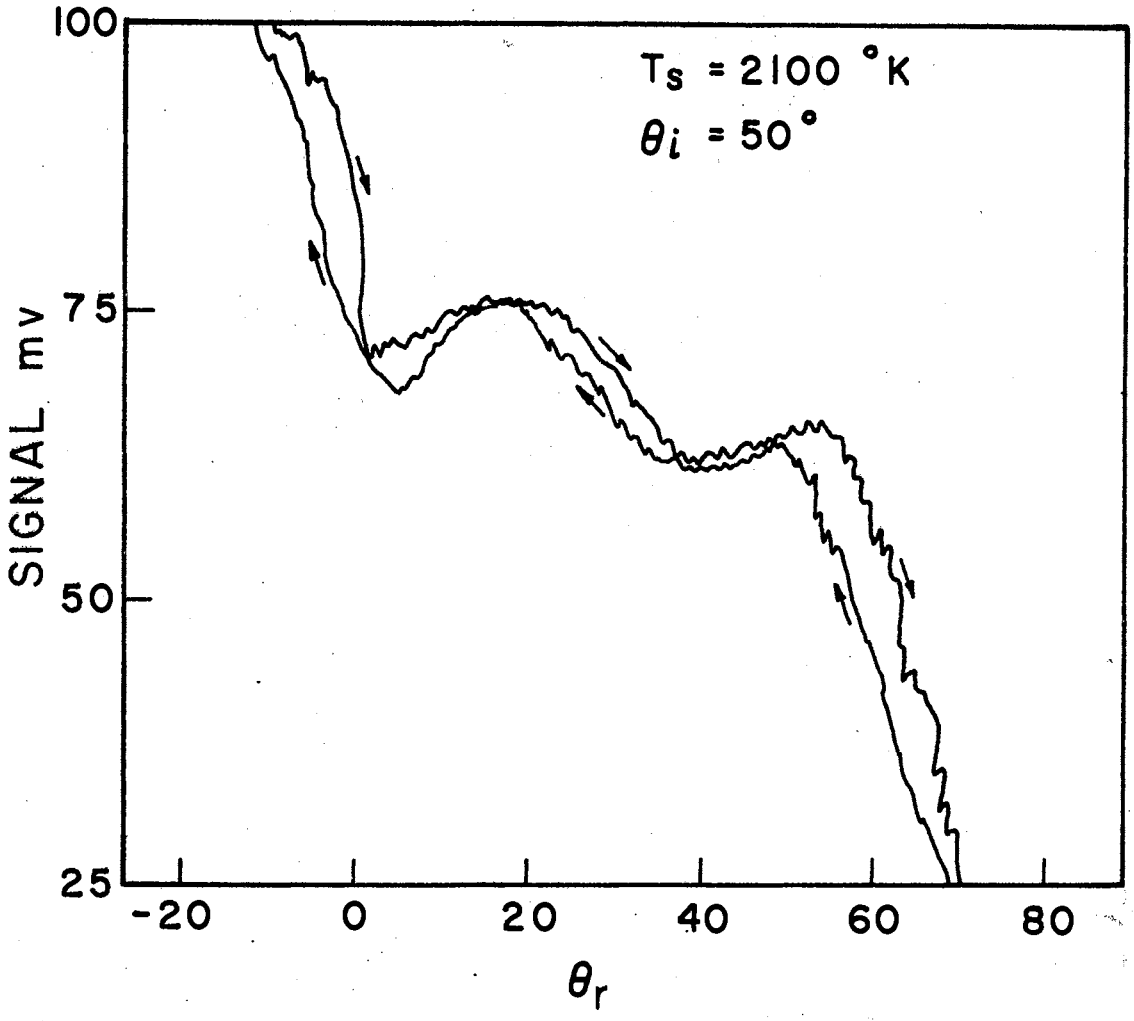

Figure 13. Typical Spatial Scattering Distribution Data

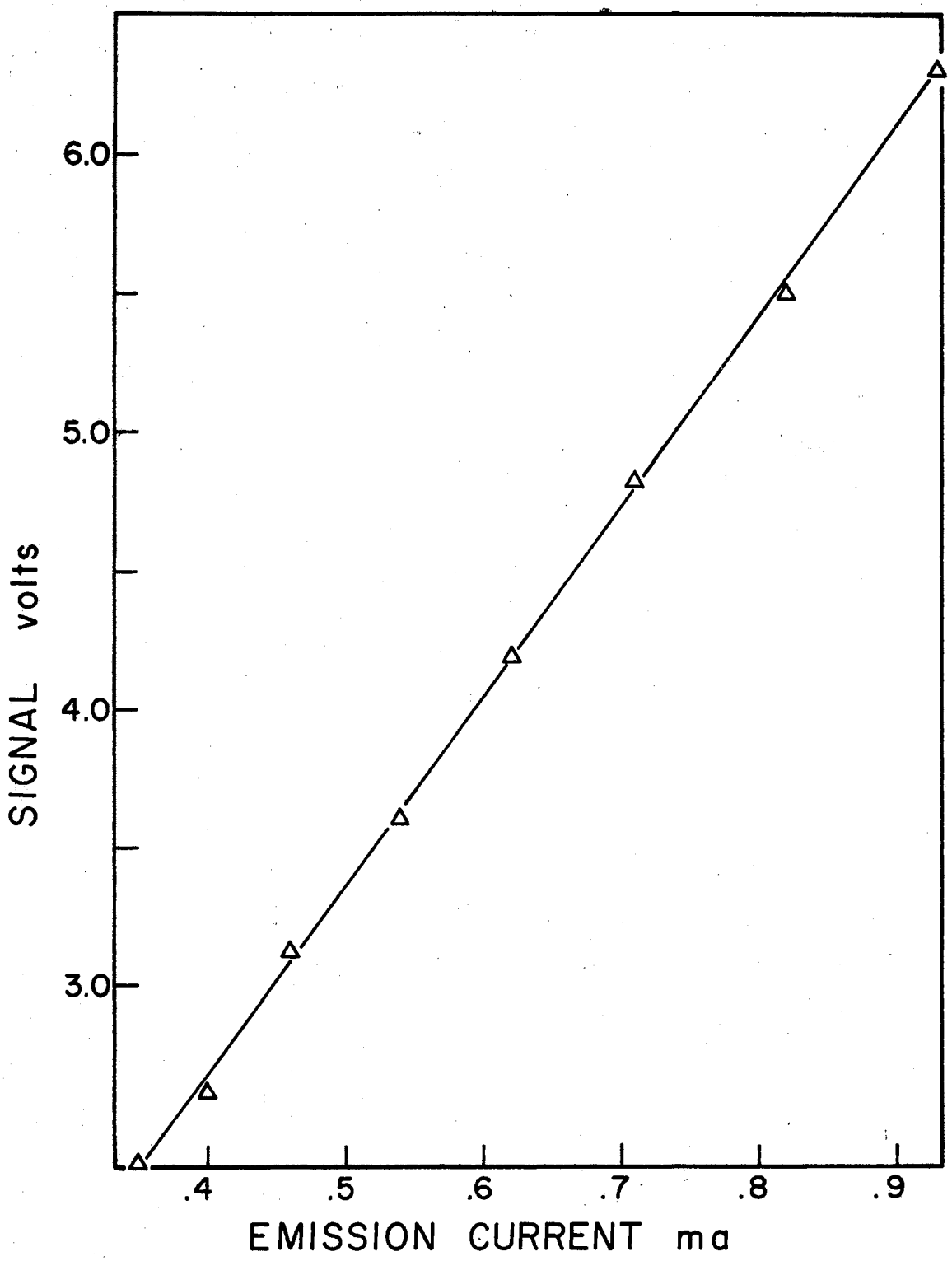

Figure 14. Emission Current of Open Detector

course of these experiments. The detector response remained remarkably constant throughout.

Figure 15 shows data taken at two surface temperatures with a fixed angle of incidence of 50°. The function, $(\cos \theta_r)$ is shown for comparison. This function was normalized to give a value equal to that of the $300^{\circ}K$ data at $\theta_r = 20^{\circ}$.

Data taken at a surface temperature of $300^{\circ}K$ follows a cosine distribution at angles of reflection greater than 15°. The data taken at $1350^{\circ}K$ follows the cosine distribution about as well as that taken at $300^{\circ}K$. In this trace, however, there is evidence of some structure centered about an angle of reflection of 20°. The most significant result shown by these data is the increasing signal strength at angles of reflection less than 0°. This backscatter was displayed to a great extent in all the traces taken in these experiments.

Figure 15 shows more data taken at a fixed angle of incidence (50°) as the surface temperature was increased. Neglecting backscatter, the maximum in the distribution shifts toward the normal as the temperature increases. The distribution becomes clearly bimodal at temperatures above $\sim 1900^{\circ}K$. Backscatter decreases relative to forward scatter at these higher temperatures. At $2100^{\circ}K$, the total in-plane flux scattered into the region that could be measured is about 44.6% of its value at $300^{\circ}K$.

It required approximately 15 minutes to take the data shown in the upper 5 traces on Figure 16. After thirty minutes at $2100^{\circ}K$, the lower plot in Figure 16 was recorded. This represents the flux distribution obtained from a stable (clean) tungsten surface. Data taken at differing angles of incidence under these same conditions gave results

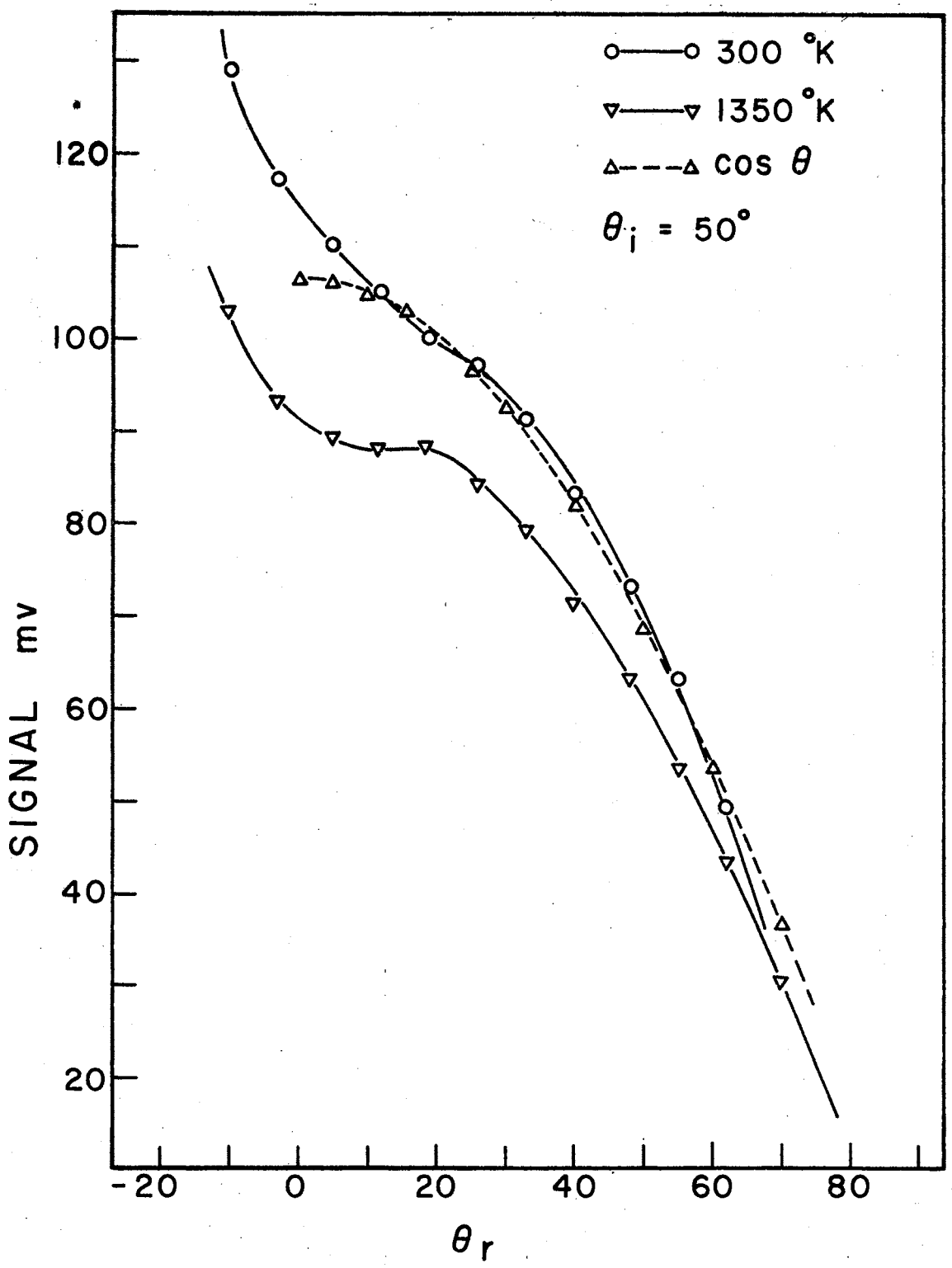

Figure 15. Spatial Distributions at Two Surface Temperatures

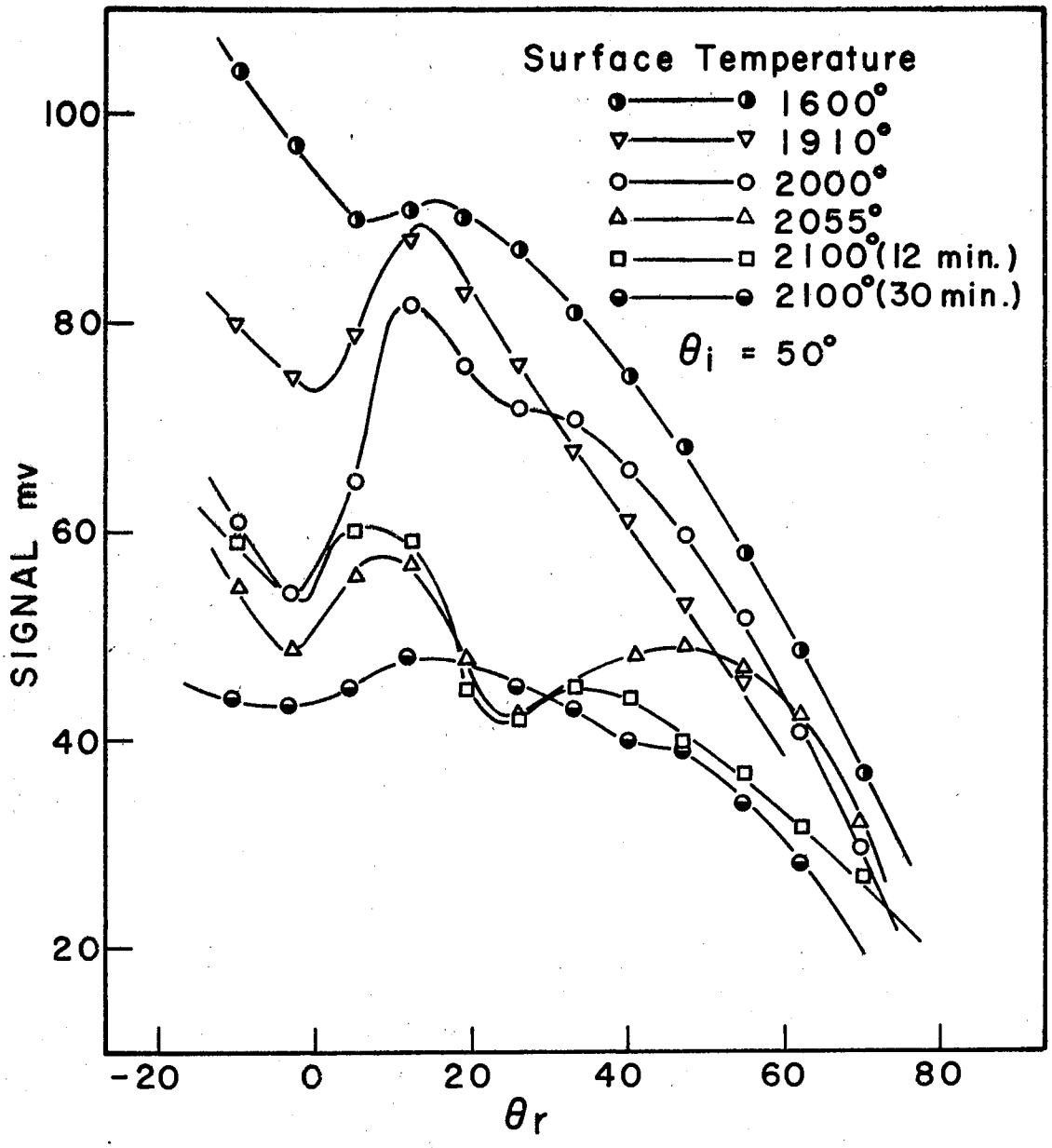

Figure 16. Spatial Distributions at Increasing Surface Temperatures

very similar to that shown in the lower plot of Figure 16.

Such data show that the surface undergoes reversible alteration as the temperature of the surface is increased. This change requires some appreciable time to accomplish. As expected, the length of time required to achieve a stable surface varies directly with the temperature at which the surface is maintained. Table II shows that result for $\theta_i = 50^o$, $\theta_r = 50^o$. In these experiments, flux intensity at the detector was measured as a function of time under constant conditions. An Arrhenius plot of these data, Figure 17, gives an activation energy of ~50 kcal/mole. This value is much lower than the heat of desorption of 110 kcal/mole found by Madey[132] and co-workers for WO_3/W. The lower value in the present work could be due to surface diffusion effects. The activation energy for diffusion at a tungsten surface is in the order of 20 kcal/mole.[143]

With the onset of large scale movement across the surface, the potential energy contour would loose some of its periodicity, and the spatial scattering patterns would tend to loose their bimodal character, and some of their intensity.

The "induction period" refers to that span of time during which the spatial scattering distributions, as a function of temperature, are clearly reproducible. That is, the process occurring at the surface is reversible. Once the process of change occurs, the tungsten surface gives a flat, unstructured distribution to the argon scattering pattern at temperatures at least as low as 1900^oK. In one test, the spatial distribution remained flat for over 3-1/2 hours at a temperature of 1930^oK after being subjected to a temperature of 2100^oK for 40 minutes. In this same test, the temperature was then lowered to 1800^oK.

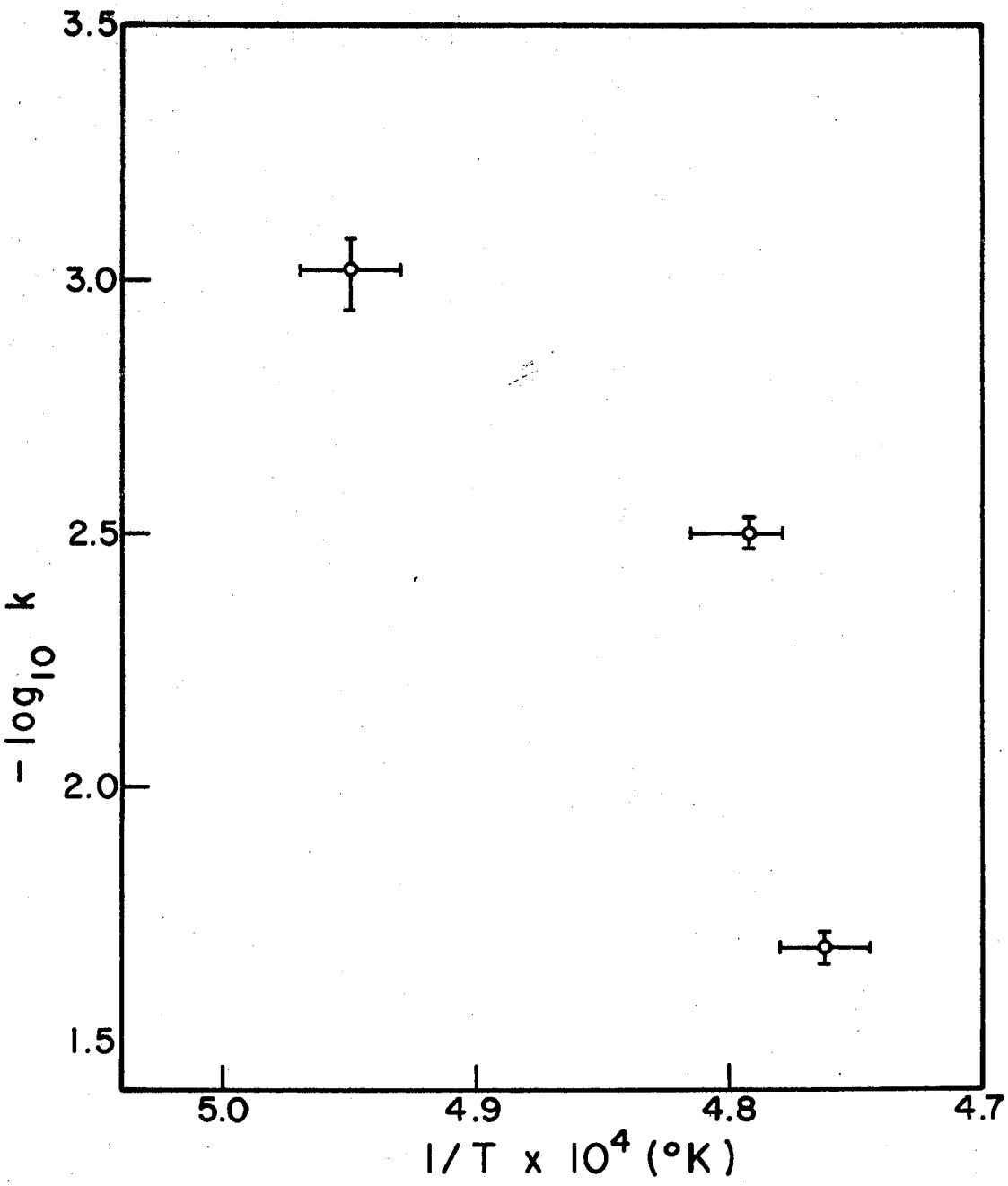

Figure 17. Arrhenius Plot for the Ar/W System

The distribution remained flat for 20 minutes. This spatial distribution is shown in Figure 18. By this time, however, the surface had vaporized sufficient material that it developed a pin hole and subsequently burned out.

TABLE II

KINETIC DATA FOR RESTRUCTURING OF THE TUNGSTEN SURFACE

Temperature	Induction Period (Minutes)	$t_{1/2}$ (Seconds)	$k \times 10^4$ sec^{-1}
2020	110	720 ± 120	9.6
2085	50	218 ± 2	32
2100	30	33.2 ± 1.5	210

Germer and May[136] used low energy electron diffraction to determine the sticking probability of oxygen on a tungsten crystal (110 face) at 300°K. They found the probability of sticking very high (almost 1) until about a 1/2 monolayer coverage of oxygen is developed. The average chance of additional oxygen molecules sticking then drops very rapidly as the full monolayer develops. They speculate that the oxides of tungsten, rather than molecular oxygen, are evaporated from the surface as the temperature of the crystal approaches 2000°K. They further conclude that the oxide coverage on the tungsten has a

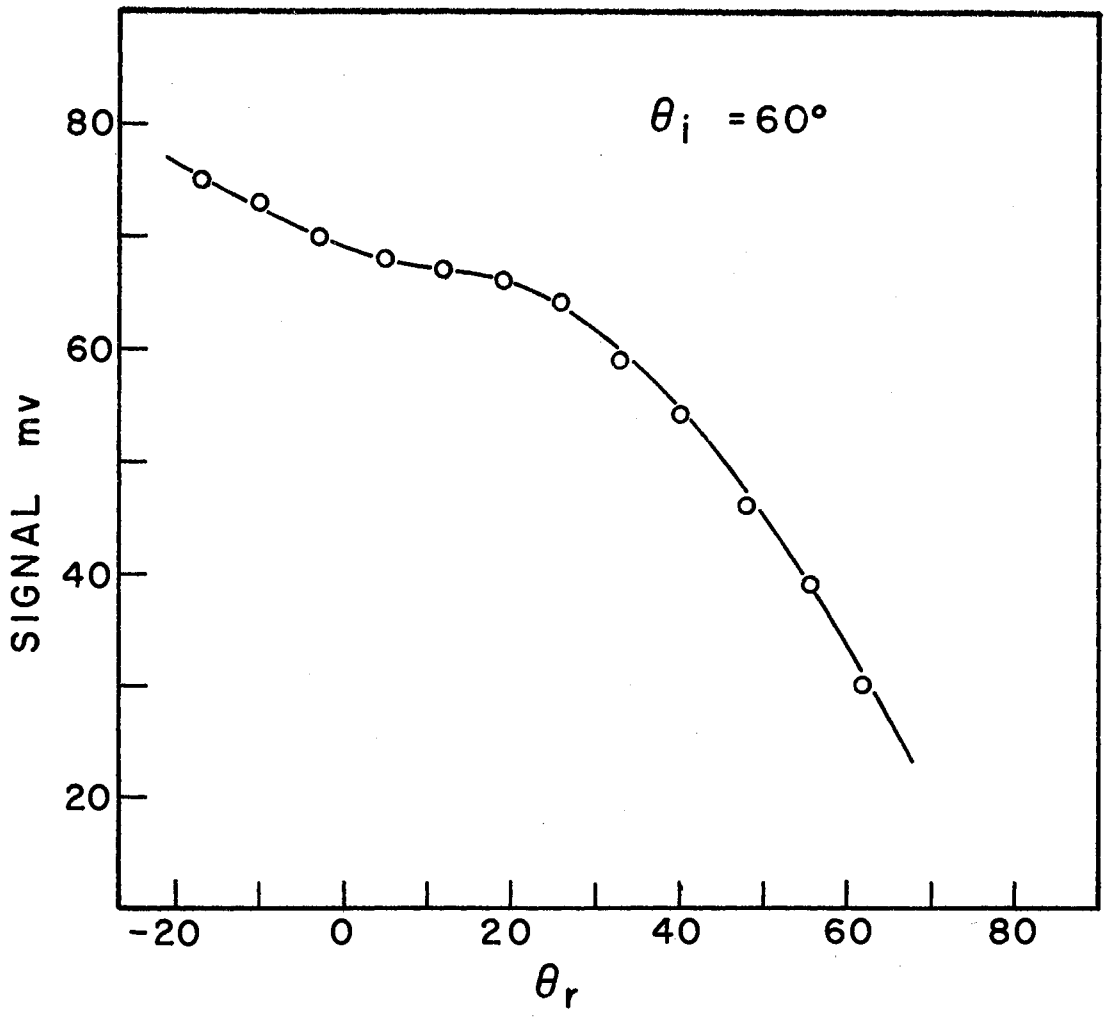

Figure 18. Spatial Distribution at 1800°K After Surface Cleaning

1:1 correspondence with the tungsten crystal lattice beneath it and that oxygen and tungsten atoms on the surface are able to interchange positions to an appreciable extent at temperatures above 800°K.

Brennan, Haywood, and Trapnell[144] found a calorimetric heat of adsorption of oxygen on tungsten of 194 kcal/mole. Their technique employed a polycrystalline tungsten sample. For reference, the heat of sublimation of tungsten is 202 kcal/mole. Any calorimetric technique for measuring the heat of adsorption of oxygen establishes an equilibrium between a gas, chiefly WO_2, WO_3, and $(WO_3)_x$, at these temperature, and an oxygenated tungsten surface. Results from such a technique are therefore influenced by (tungsten oxide)-(tungsten oxide) interactions. A non-equilibrium method such as one where the oxide vapor is pumped by a high vacuum, will give a more accurate heat of adsorption.

The cleaning process that occurs at the target surface and the bimodal nature of the spatial scattering flux distributions are clearly shown in Figures 19 and 20. A bimodal distribution has been noted only rarely in other works.[78-82] McClure[128,129] discusses the likely causes of these sharp intensity maxima. He concludes that the essential requirement for the formation of such a bimodal distribution is a spatial periodicity in the gas atom - target surface interaction field. That such distributions are not usually seen is generally taken as an indication that either: (1) the fraction of the surface under study is not sufficiently well-ordered or, more likely (2) the periodic variation of the long-range gas atom-metal field is too weak.

The peaks in a bimodal distribution of this sort result when a stream of gas atoms interact with a periodic surface field and are preferentially repulsed into two rather narrow solid angles. The

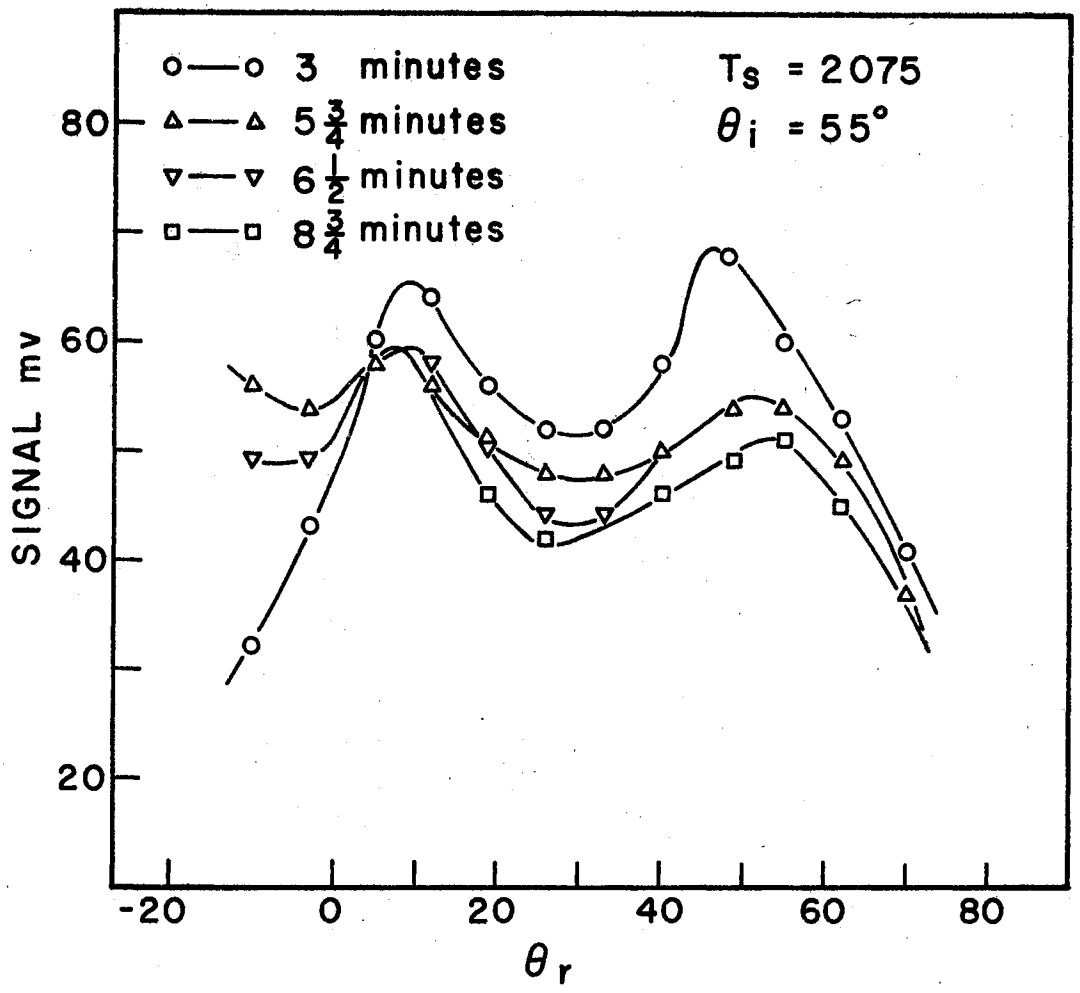

Figure 19. Spatial Distributions During Cleaning

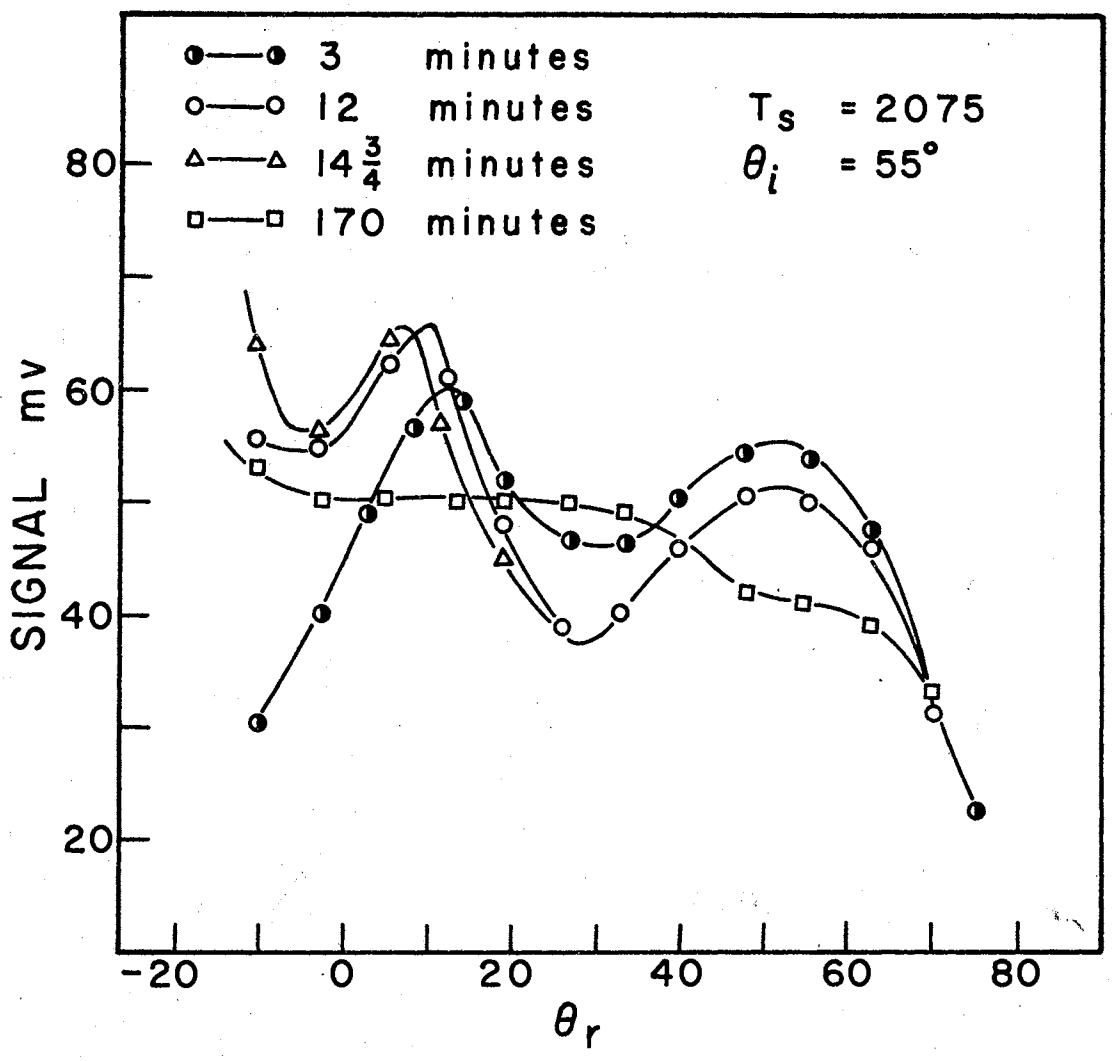

Figure 20. Spatial Distributions During Cleaning

incident beam is, to a first approximation, evenly distributed over the metal surface. All impact parameters are equally likely. The surface is conveniently pictured as a series of equipotential mounds, which are situated directly over each of the metal atoms on the surface. Thus, all angles of reflection are not equally likely. It is much more probable that a gas atom will reflect off the "side" of one of the mounds rather than from either a mound "peak" or "valley". This situation is depicted in Figure 21. Part A shows the equipotential surface in the plane of the target normal and the incident beam, with a scale of impact parameter represented above. Three rays, corresponding to impact parameters of 0.0, 0.3, and 0.8, are traced. Part B shows the angles of reflection that might be expected from various equally spaced impact parameters. Part C is a histogram showing the number density distribution of the scattered gas particles as a function of angle of reflection. It is seen that this distribution is highest for the angles of reflection about 12° and about 75°. These two angles of reflection arise from particles which have impact parameters of from 0.1 to 0.3 and from 0.6 to 0.8. Within those ranges of impact parameter, the quantity, $\left(\frac{\partial \theta_r}{\partial I_g}\right)$, approaches zero, and the number density distribution as a function of θ_r has maxima. Thus, there exist regions along the potential energy contour probed by the gas atom where angle of reflection is relatively uninfluenced by impact parameter. When viewed along the incoming beam, these areas appear as the "sides" of the contours in the equipotential surface. The influence that this contour has in the extent of the bimodal distribution is a function of the angle of incidence and energy of the incident particle and the depth and lattice spacing of the contour. These effects are detailed

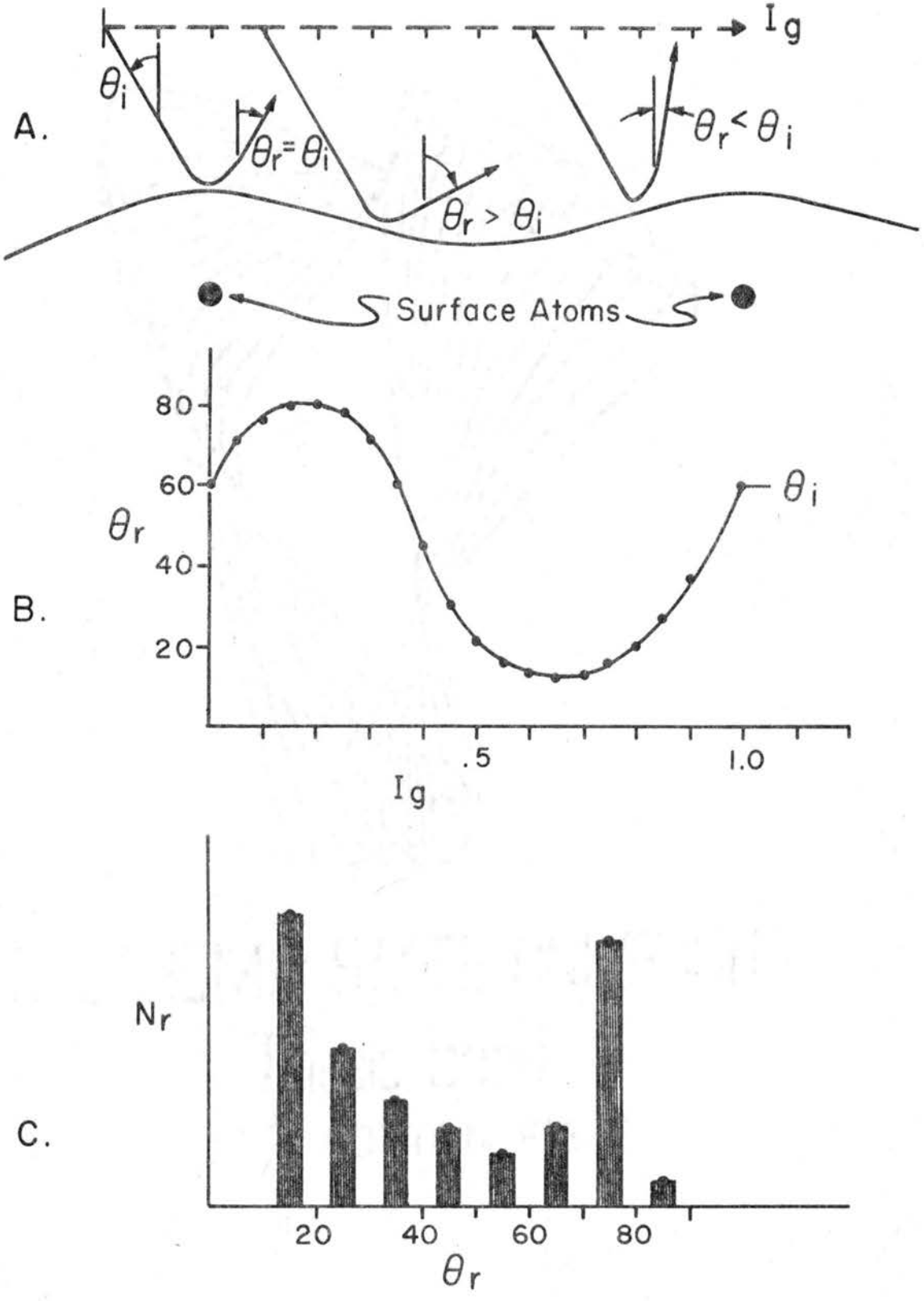

Figure 21. Origin of Bimodal Intensity Maxima

by McClure, who refers to these intensity maxima as "surface rainbows", since they result from a mechanism similar to that which causes the rainbow structure in gaseous binary collisions.

One consequence of gas-solid interaction models that employ a finite range interaction field, such as the models of Oman, McClure, or Lorenzen and Raff, is that as lattice spacing increases, so will the structure in the spatial scattering distributions. The potential energy contour for the expanded lattice has a much greater amplitude than does the compressed lattice structure, and the surface appears rougher to the incident gas beam. Thus, the periodic variation in the potential field of an oxygenated tungsten surface is greater than the variation shown by a clean tungsten surface, and bimodal scattering is seen. It is likely that the annealed tungsten surface has large scale surface dislocations and is appreciably rough on a microscopic scale. Bimodal spatial scattering distributions are still possible, though, because two criteria fundamental to its observation are still satisfied by the annealed surface. The surface has a certain long-range order on an atomic scale, in that only crystal planes of a single type are presented to the incident beam, and the potential energy contour at the surface has sufficient amplitude.

It is not unreasonable to expect that the clean surface of tungsten presents to an incoming argon atom a potential field much "smoother" than that of a surface with a partial coverage of oxygen atoms. Germer and May[136] postulate the existence of ordered domains on a tungsten surface with a 1/2 monolayer coverage of oxygen. In these domains, rows of oxygen atoms are spaced between rows of tungsten atoms, doubling the size of the unit cell. Their conclusions were

confirmed and expanded upon by Madey[132,133] and co-workers. At a temperature greater than 1700°K, the final oxides of tungsten (WO, WO_2 WO_3) desorb, leaving a monolayer or less of atomic oxygen. The final adsorbate leaves the surface as the temperature goes above 2200°K. Both oxygen atoms and tungsten atoms are highly mobile on the tungsten surface at moderately elevated temperatures.[136] (> 800°K). The activation energy for diffusion of tungsten on a tungsten surface is about 20 kcal/mole.[143] Several authors report on the restructuring that occurs on the surface of polycrystalline tungsten following annealing. Tamm and Schmidt[145] conclude that the reconstructed surface consists of large single crystals which are primarily oriented with the (110) plane exposed. Other authors[146,147] discuss how such faceting of surface planes into the (110) orientation is enhanced by the presence of oxygen.

These facts support the hypothesis that the periodic variation in the potential field of an oxygenated tungsten surface is greater than the variation shown by clean tungsten surface. Thus, it seems likely that the process occurring in Figures 19 and 20 is the removal of adatoms from the tungsten substrate. The process of evaporation proceeds smoothly until about a 1/2 monolayer coverage is reached. This might correspond to the "induction period" mentioned earlier. The sticking probability at this coverage then becomes significantly higher. The decrease in signal strength at the lock-in amplifier marks the final evaporation of the remaining oxygen. The accommodation of argon on a clean tungsten surface is much less than that of argon on a contaminated surface. As the surface becomes cleaner and accommodation less, the energy (velocity) of the reflected particles drops

and consequently, the flux of the reflected stream of gas atoms decreases.

Hopkins, Pender, and Usomi[112] measured the work function of oxygen molecules on a tungsten surface with differing crystallographic orientations. They found a pronounced restructuring of the (110) surface at approximately a half monolayer coverage. O'Keefe and French[113] have determined the spatial scattering distributions of inert gases reflected from a tungsten surface selectively covered with various contaminant gases. Their beam source produced relatively energetic particles (0.25 to 2.0 eV). Gases with energies at the lower end of this range displayed broader scattering distributions with some evidence of bimodal structuring.

It should be noted that for all measurements of spatial distribution reported here, the detector employed was sensitive to particle flux. It was impossible to achieve a reproducible measurement of the speed component of the flux, because the noise level was too great at the speed selector.

Yamamoto and Stickney[93] measured the mean speed of argon scattered from a clean tungsten crystal using a time-of-flight procedure. Using their data at a surface temperature of 2100°K, it is possible to estimate the number density spatial distribution from the flux data taken in this current work. These results are shown in Figures 22, 23, and 24. These plots are of signal intensity in arbitrary units versus angle of reflection relative to the surface normal. The number density plot has been normalized to give a value equal to that of the flux at $\theta_r = 64^\circ$.

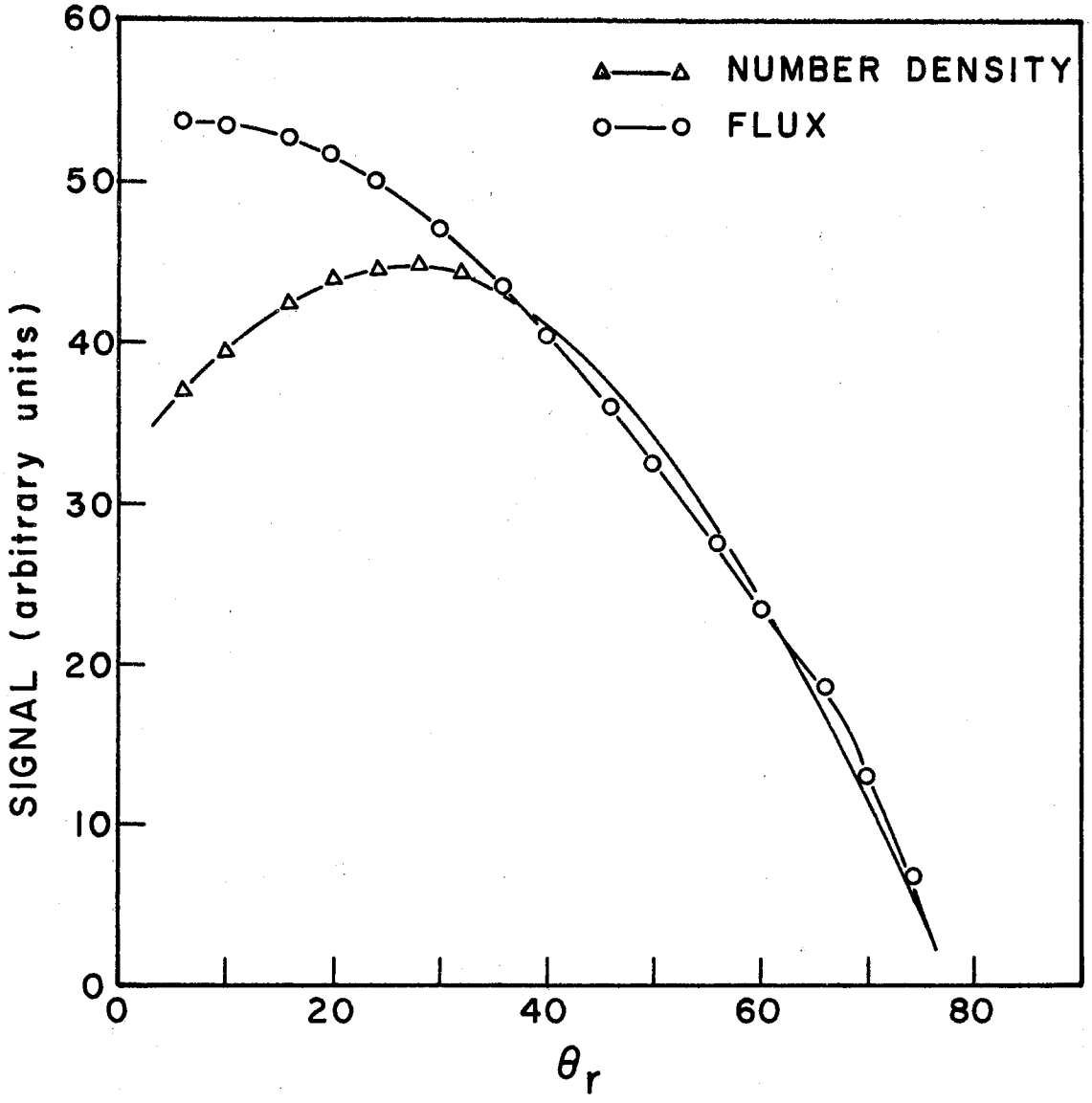

Figure 22. Flux and Estimated Number Density Distribution. $\theta_i = 40^o$

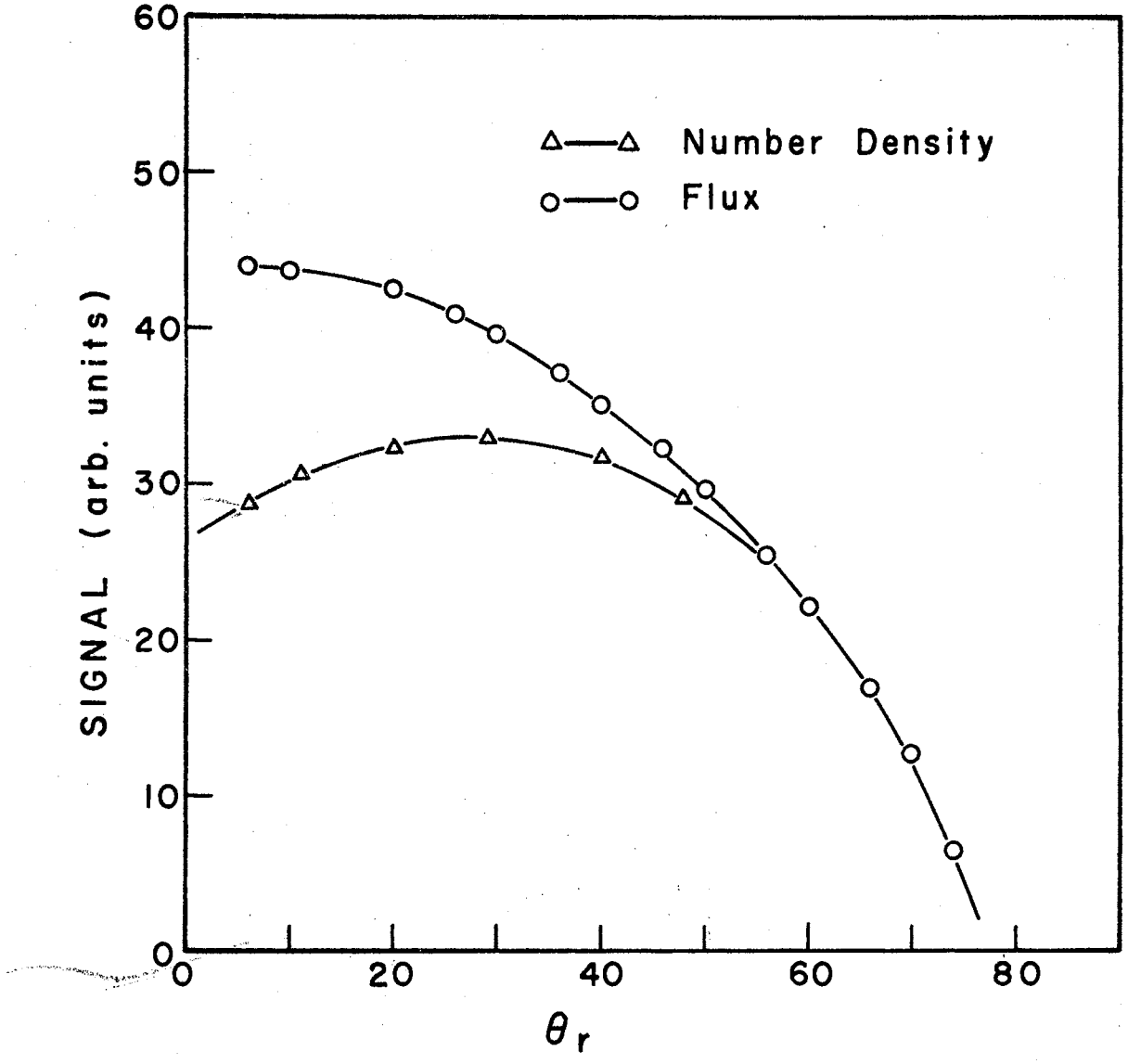

Figure 23. Flux and Estimated Number Density Distribution. $\theta_i = 50^o$

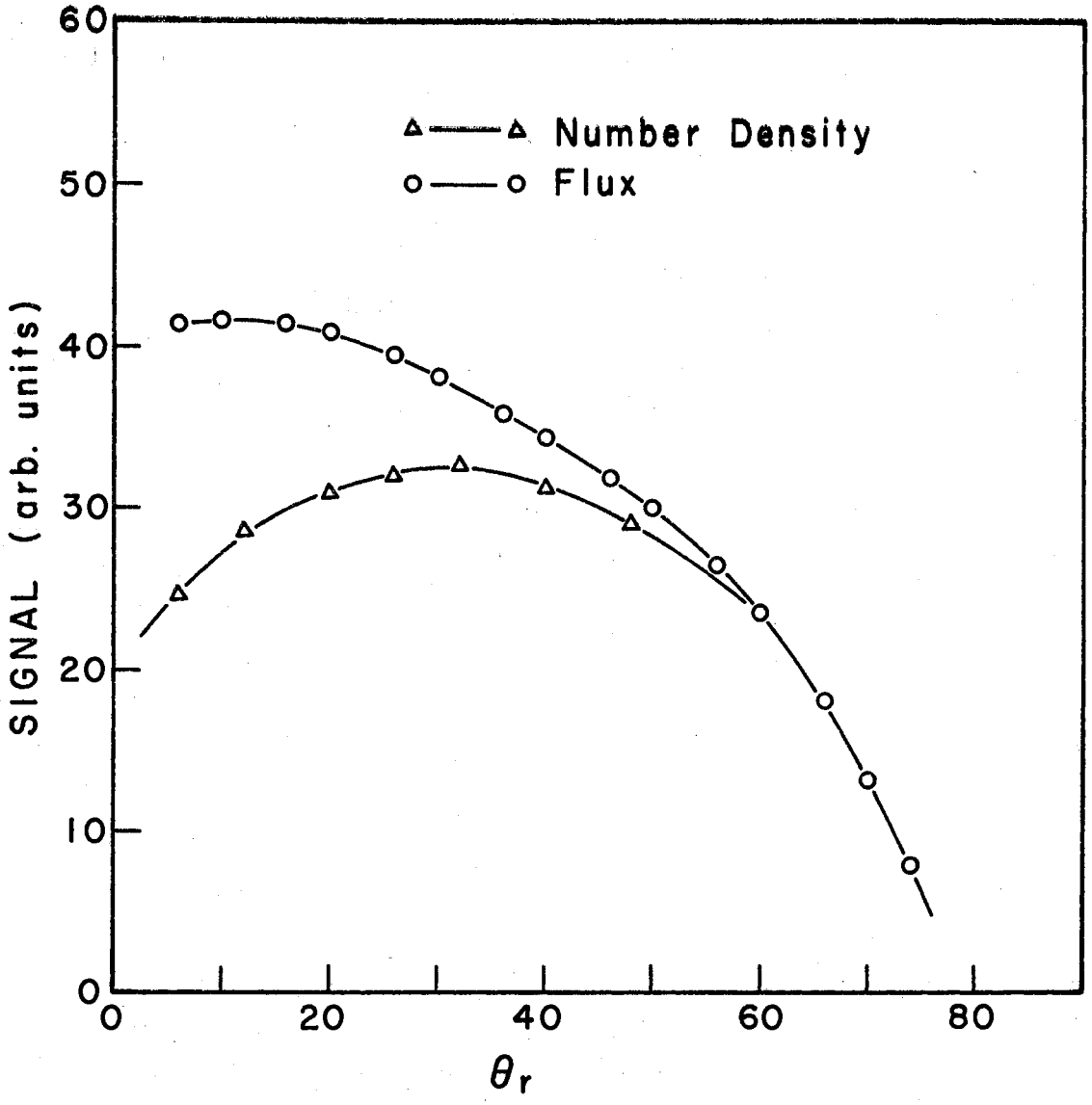

Figure 24. Flux and Extimated Number Density Distribution. $\theta_i = 60^o$

Table III gives a summary of the data shown in the three figures. Yamamoto and Stickney note that their estimate of $\bar{u}_r$, the mean speed of reflected particles is "based on an approximate analysis of undetermined accuracy". Part A of Table III gives the data based on a measurment of flux distribution with the tungsten surface at a temperature of 2070°K. Using the estimates of Reference[93], flux intensity as function of angle of reflection was divided by mean speed as a function of angle of reflection to give the corresponding number density distribution.

TABLE III

SPATIAL DISTRIBUTION DATA. COMPARISON OF RESULTS FROM POLYCRYSTALLINE TUNGSTEN WITH A SINGLE TUNGSTEN CRYSTAL.

	θ_i	θ_r'	$\theta_{1/2}$	$\Delta\theta$	A_r'
A	40°	26°	72°	14°	44.8
(this work)	50°	29°	76°	21°	33.0
	60°	34°	69°	26°	32.6
B	40°	28 ± 2	53 ± 3	12 ± 2	44.8
(Reference 93)	50°	35 ± 2	54 ± 2	15 ± 2	43
	60°	39 ± 2	55 ± 3	21 ± 2	39

Part B gives the results of Reference 93, in which the number density distribution as a function of angle was measured directly. The tabulated parameters are:

$\theta_i \equiv$ angle of incidence measured from the normal

$\theta_r' \equiv$ angular position of the peak in the number density of the reflected particles

$\theta_{1/2} \equiv$ full-width of the number density distribution at one half peak maximum

$\Delta\theta \equiv \theta_r - \theta_r'$ deviation of the angular position of the maximum in the number density from the specular angle

$A_r' \equiv$ magnitude of the number density at θ_r'

The data in Table III was normalized to give equal A_r' for $\theta_i = 40^o$. The results of this current work confirm with generally good agreement some of the treands found in the earlier work of Yamamoto and Stickney. An increase in the angle of incidence causes a corresponding increase in the angle of reflection at which the number density distribution has its maximum ($\partial\theta_r'/\partial\theta_i > 0$). This effect seems to be observed in all gas-solid interaction systems. An increase in angle of incidence causes an increased deviation from the angle at which specular reflection would be noted. ($\partial(\Delta\theta_i)/\partial\theta_i > 0$). This effect is seen in some other systems, but not in all. As the angle of incidence is changed from 40^o to 60^o, there is a drop in maximum signal.

The greatest discrepancy between the two sets of data is in the magnitude and trend of $\theta_{1/2}$. These differences are unquestionably the result of the fundamental difference in the target material used in the two experiments. Yamamoto and Stickney used the (110) face of a tungsten crystal in their work, while in the current work a

polycrystalline tungsten foil is employed. Smith, Saltsburg, and Palmer[66] have compared spatial scattering number density distributions of argon from both polycrystalline nickel and the (111) face of a single nickel crystal, with an angle of incidence of 50°. They found that in going from an ordered surface to a polycrystalline surface, the peak position, θ_r', shifted from 44° to 38°. The width of the distribution at one-half maximum intensity increased from 39° to 65°. Thus, a polycrystalline surface tends to give more diffuse spatial scattering patterns than does a surface cleaved from a single crystal. These diffuse patterns tend toward the cosine distribution that is characteristic of a contaminated, rough, and/or disordered surface. In a series of experiments with ultra-high vacuum conditions, McGinn[150] measured the momentum exchange between beams of argon and krypton and a gold surface deposited on a mica substrate. His surface conditions caused the gold to be layered in a random fashion (not epitaxially). He found that data taken at grazing incidence showed variations from surface-to-surface that could only be attributed to surface irregularities.

Using the data of Reference 93 to estimate the number density distribution as a function of angle of reflection shows the great deal of backscatter present in this gas-solid system. This backscatter is the result of surface roughness on an atomic scale and is most pronounced at the higher angles of incidence.

The Figures 25 through 30 show the changes in the structure of the spatial flux distributions for various angles of incidence and surface temperature. The ordinant on each of the Figures 25 through 30 is the actual signal strength at the lock-in amplifier measured in millivolts.

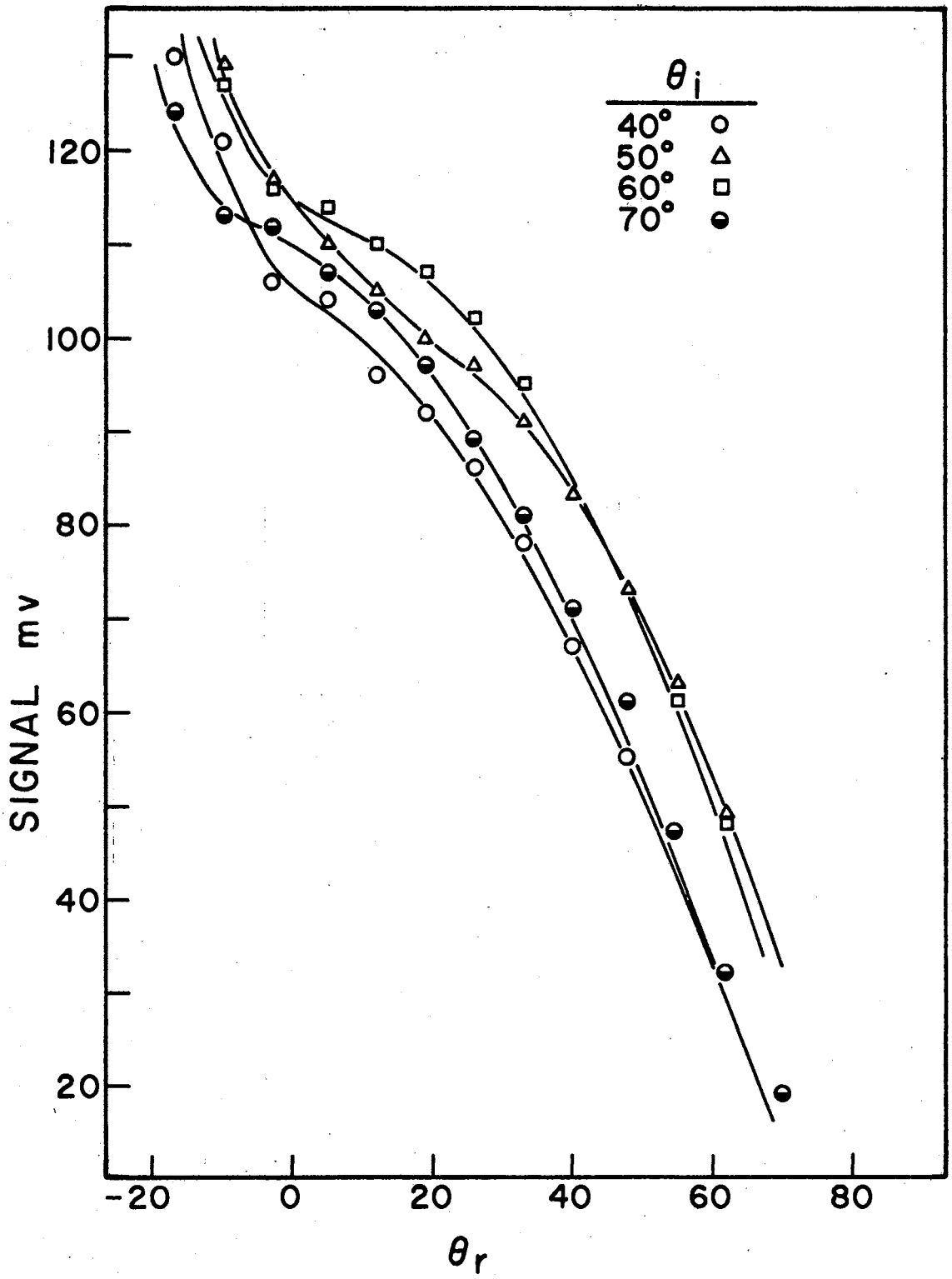

Figure 25. Spatial Distribution. Ts = 300°K

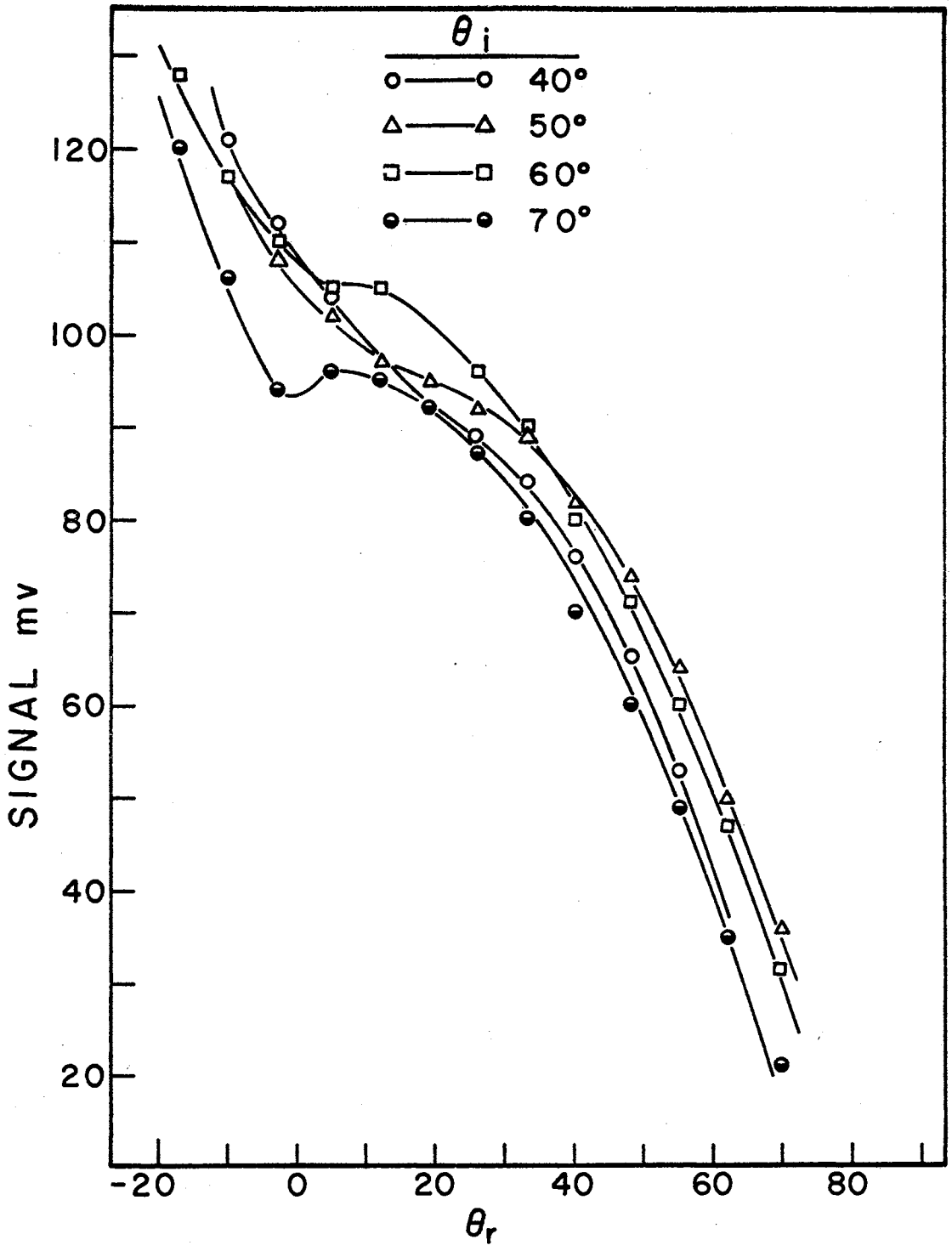

Figure 26. Spatial Distribution. Ts = 1400°K

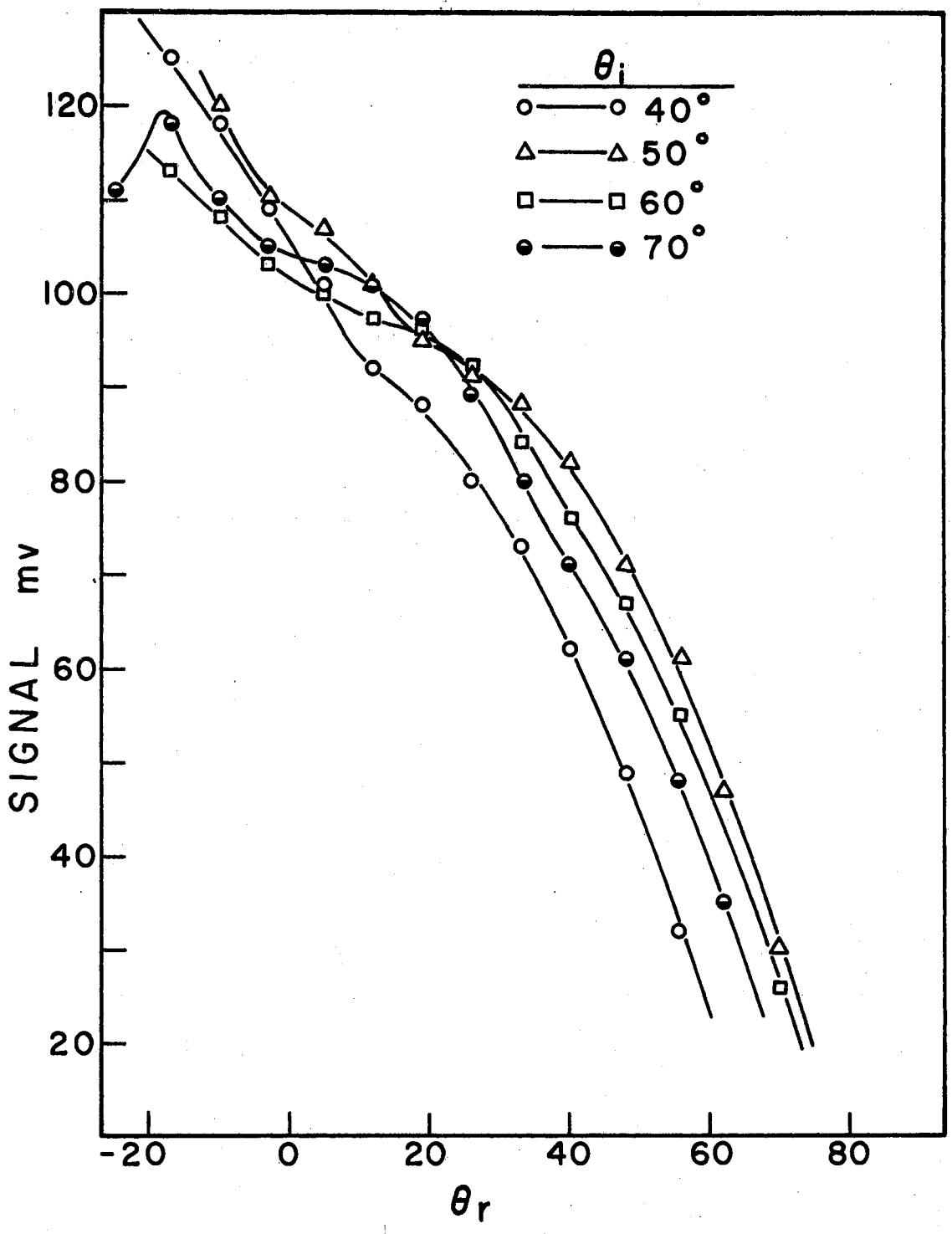

Figure 27. Spatial Distribution. Ts = 1800°K

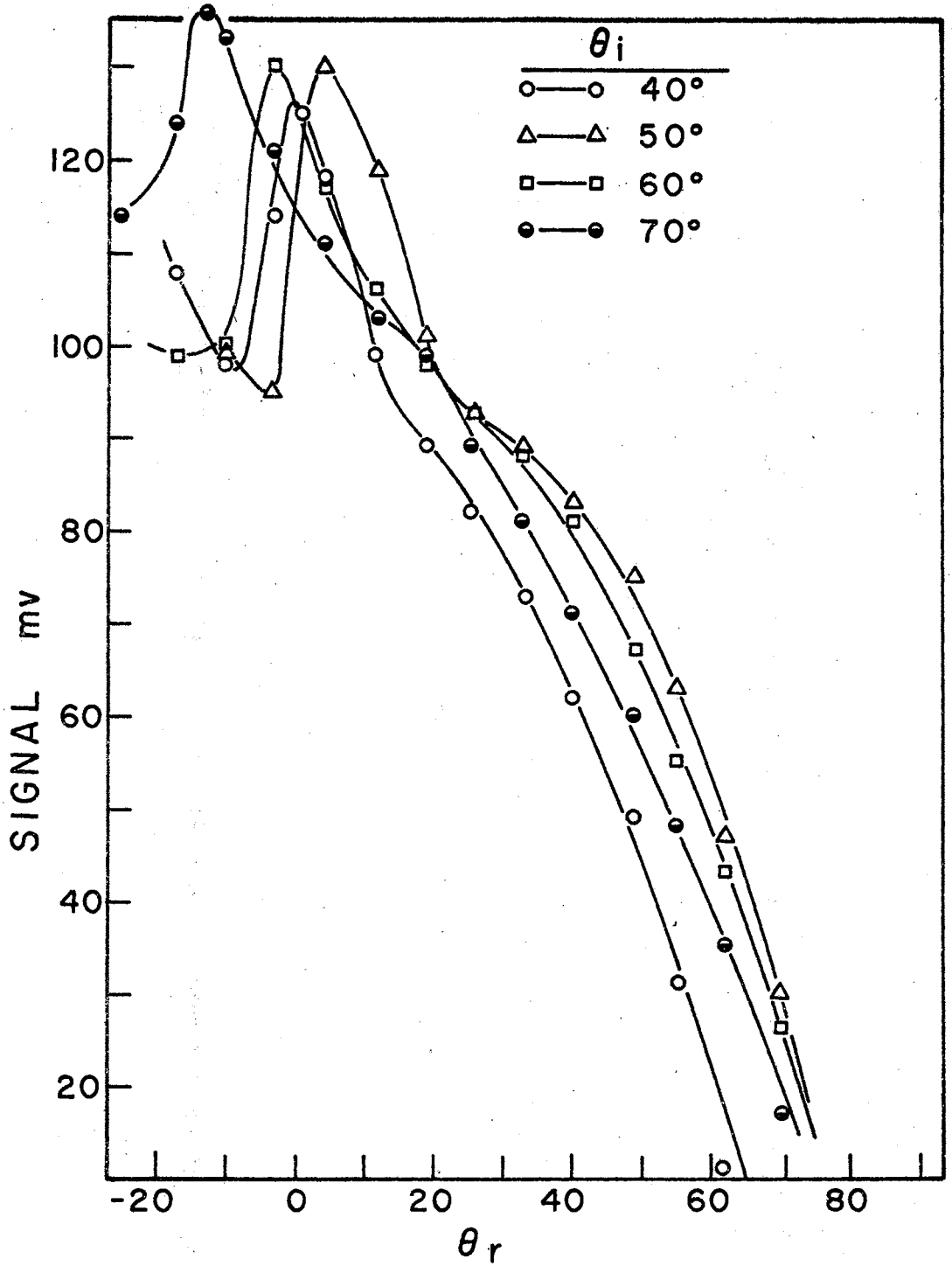

Figure 28. Spatial Distribution. Ts = 1930°K

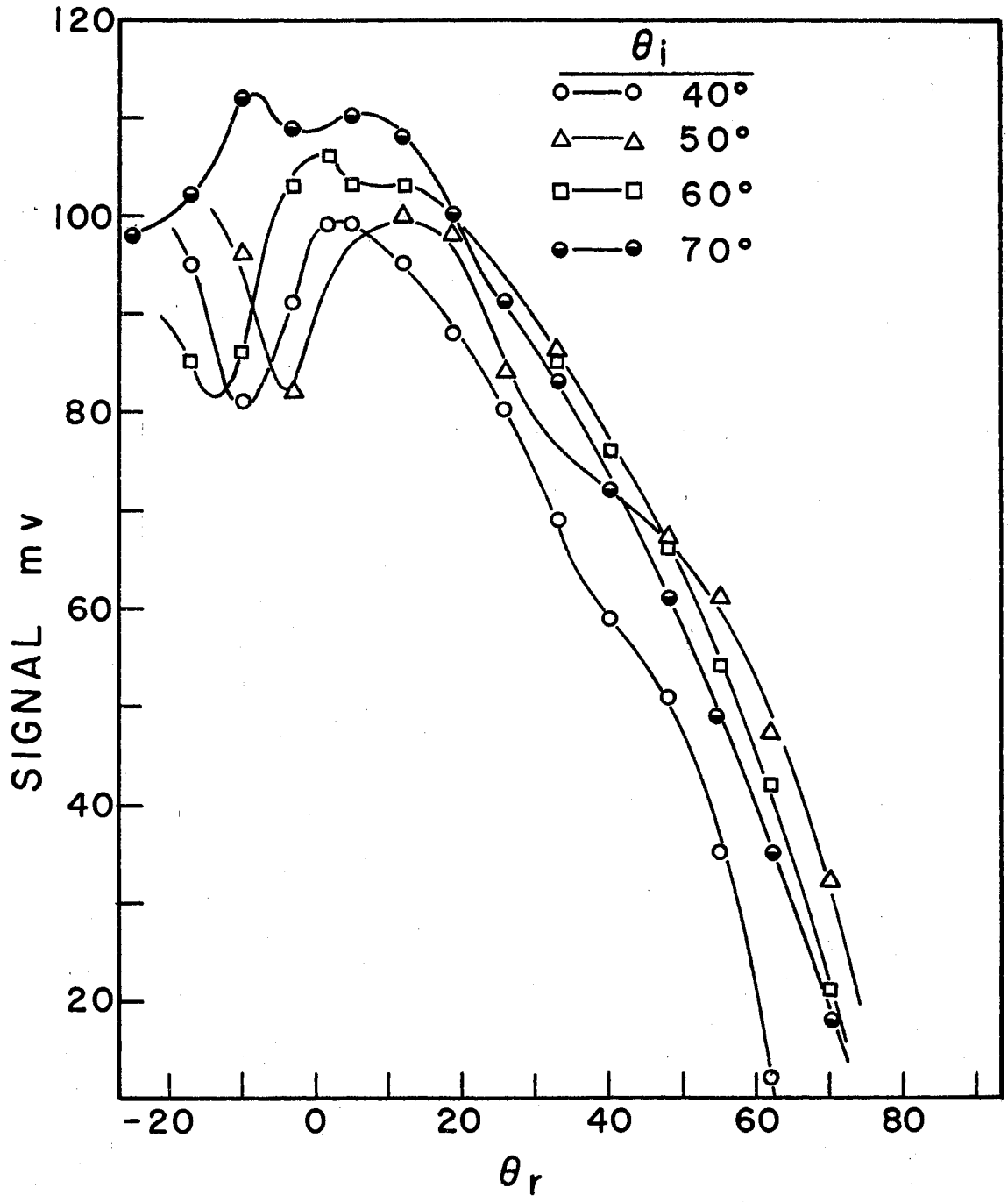

Figure 29. Spatial Distribution. Ts = 1980°K

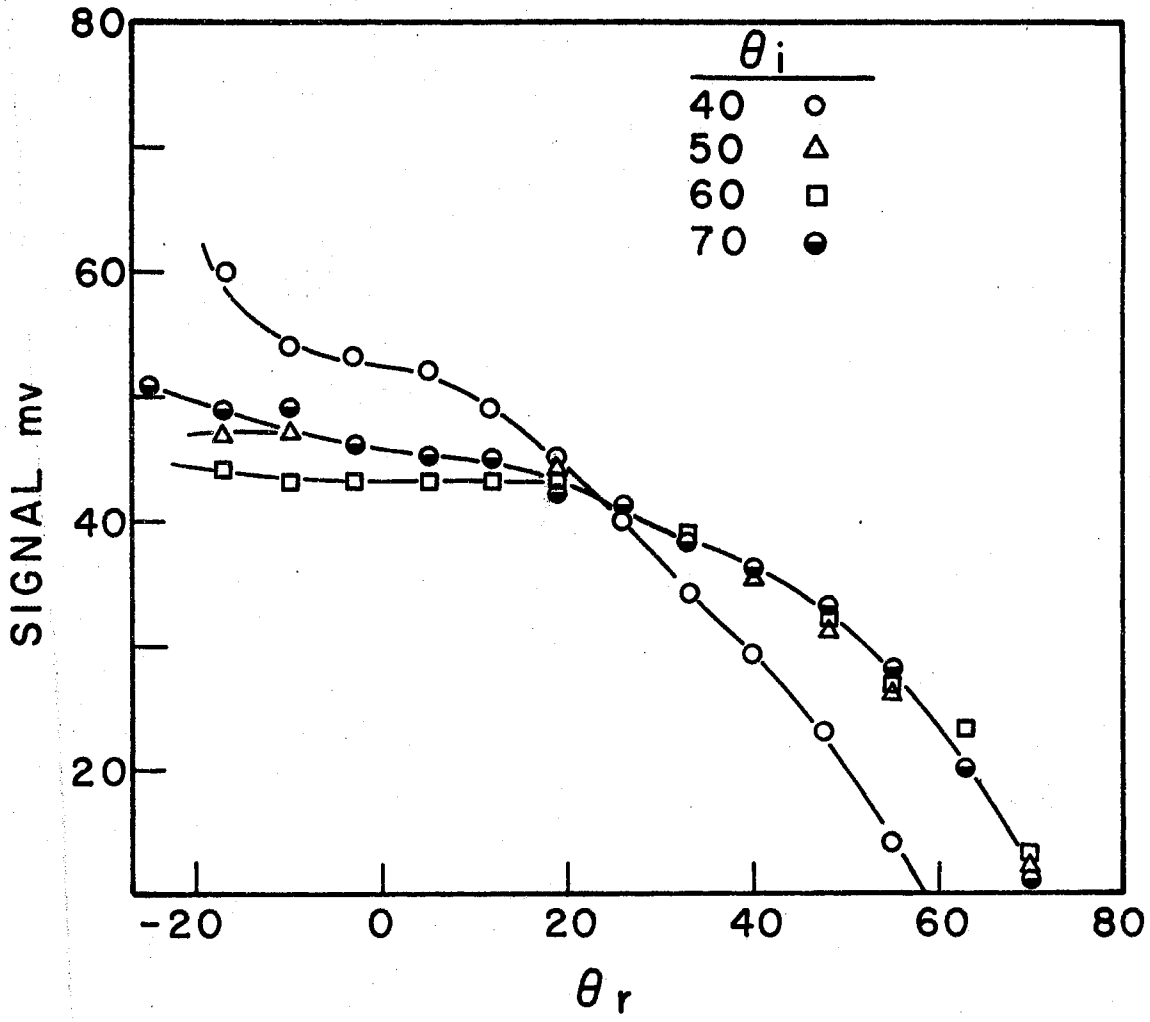

Figure 30. Spatial Distribution. Ts = 2071°K

None of the Figures have been normalized. As was noted previously, backscatter (relative to forward-scatter) and structure in the distributions increase with increasing angle of incidence. These two effects reach a peak at 1930°K where the solid surface is postulated to consist of about a half monolayer of adatoms. As the surface is cleaned, backscatter decreases. There is, however, still an appreciable backscatter when the surface is heated to 2100°K or higher, under which conditions all adsorbed particles are removed. The disordered, polycrystalline surface tends to cause a diffuse scattering at this high temperature.

The backscatter is evidence of a large momentum accommodation at the argon-tungsten interface. A crude estimate of the change in energy transfer coefficient with the establishment of a clean surface may be made by comparing Figure 28 with 30. Energy transfer coefficient measures the fraction of energy that is transferred from incoming argon atoms to the surface. Many authors have noted that accommodation is much greater on rough or contaminated surfaces than on clean ones. In Figure 28, the surface is at 1930°K and the maximum flux intensity is measured with an angle of incidence of 70°. For these conditions, the signal strength is 136 mv at $\theta_r = -12°$. In Figure 30, the surface temperature is 140°K higher, yet the signal is only 49 mv under the same geometry. Under the conditions of Figure 28 (rough, contaminated surface), the out-of-plane scattering of the flux would be expected to be somewhat more substantial than in the conditions of Figure 30. However, the measured in-plane flux distribution of Figure 30 is a great deal less than in Figure 28. This indicates that there is an appreciable decrease in the mean velocity of the

reflected particles under clean-surface conditions. A quantitative measure of ETC awaits a definitive determination of the actual speed distribution of particles scattered from the surface.

There is a considerable amount of structure seen "behind" the surface normal in Figures 28 and 29. This highly structured back-scatter has not been previously reported. There seems to be a "direct recoil" mechanism acting through the adlayers which causes a significant number of particles to scatter back toward the nozzle. At its nearest, the detector is about 25° from the beam.

In Figures 28 and 29, the flux at the surface normal with $\theta_i = 70^{\circ}$ is 10% greater than that of $\theta_i = 40^{\circ}$. Under conditions of a clean surface, as in Figure 29, the flux at the normal is greatest when $\theta_i = 40^{\circ}$. With loosely adsorbed particles on the surface, a type of "structure" scattering prevails. Argon atoms approaching the ad-layer at an angle of 70° are more subject to the periodic, irregular nature of the surface than are atoms that strike the surface more from the normal. With a clean surface being presented to the incoming particles, accommodation is much greater with decreasing θ_i, thus the flux at the surface normal under these conditions is greater for $\theta_i = 40^{\circ}$ than it is for $\theta_i = 70^{\circ}$.

A residual gas analyzer is necessary for positive identification of surface contaminants. Many authors have noted that the principal residual gases in a stainless steel vacuum system are water, carbon monoxide, and carbon dioxide. All of these would be expected to strongly adsorb on the tungsten target surface at low temperatures and then dissociate and desorb as the temperature is increased.

CHAPTER IV

CONCLUSION

A. Summary

The argon-tungsten interface has been investigated. An experimental apparatus has determined the spatial distribution of argon atoms that have been scattered from a polycrystalline tungsten surface.

Temperature of the surface, angle of incidence of the gas particles, and the angle of reflection of the particles were variables that were studied. A quartz nozzle was employed to generate the argon beam. The distribution of particle speeds within the beam was found using a slotted disk velocity selector. Direct measurement of the speed distribution of the reflected argon particles was not achieved.

Some general conclusions concerning the results are:

(1) The distribution of particle speeds within the beam generated by a quartz nozzle is quite narrow. The spread in the speed distribution of such a beam is not a sensitive function of the temperature.

(2) The flux distributions of scattered argon particles show the expected qualitative trends.

(3) The presence of a large amount of backscatter and structure in the flux distributions as surface temperature is raised is postulated to be the result of adatoms on the tungsten surface. The bimodal nature of the flux distribution arises from the highly periodic nature of the partially contaminated tungsten surface.

(4) Backscatter persists in the flux distributions when the surface temperature is above that at which particles could be adsorbed. This backscatter is taken to be typical of scattering of argon from a "clean" but disordered (polycrystalline) surface.

(5) Energy transfer across the gas-solid interface diminishes rapidly as the surface contaminants are removed.

B. Suggestions for Further Work

The current work demonstrates the utility of this technique as a tool to probe the nature of the gas-solid interface. The complete elucidation of the interaction requires some improvements in the experimental apparatus.

Three primary modifications should be accomplished: (a) the noise level, inherent in the current slotted disk velocity selector, must be reduced; (b) the vacuum should be improved; (c) some method for analyzing residual gas should be incorporated into the system.

Direct measurement of energy transfer across the gas-solid interface requires a knowledge of the mean energy of incident and reflected particles. The present SDVS is adequate for the determination of incident particle velocities. If a number density detector were incorporated into the current apparatus, it might be possible to indirectly evaluate the mean speed of the scattered particles. The relative signal strength of number density and flux detectors is proportional to the mean speed of the distribution being measured. The constant of proportionality could be determined by using both detectors to directly examine the gas nozzle beam, for which the mean speed is currently available. This technique was employed with some success by Smith[90]

as well as by McKinley.[151] Both authors used a single detector which had a shutter at the rear of the detector envelope. The shutter was opened, allowing free passage of the gas particles for number density measurements. For flux measurements, the shutter was closed. Both authors assumed a Maxwell-Boltzman distribution for their incoming gas particles. However, their source chamber pressures and orifice geometry almost certainly precluded that type of distribution. Use of a gas nozzle beam source with a sharply peaked and well known particle speed distribution would increase the value of this technique considerably. If two detectors were employed, one with a slotted disk velocity selector and one with a shutter device, an excellent opportunity for cross-checking the results would exist.

An improvement in vacuum is essential to maintenance of a clean surface at low temperatures. The present apparatus could easily accommodate more or larger vacuum pumps. In the absence of an improved vacuum, the surface temperature must be kept at a high value to guarantee a surface free of adsorbed particles. High temperatures cause the rapid sublimation of target material. Frequent replacement of the target was therefore necessary in the current work. Use of a more substantial target material (thicker) is recommended.

A residual gas analyzer would be useful in the study of surface coverage by adsorbed particles. In the present system, the true nature of the residual contaminants is unknown. The principal gases present in vacuum systems below 10^{-5} mm Hg are usually carbon monoxide, water, and carbon dioxide. The presence of carbon monoxide contributes considerable uncertainty as an impurity in studies of controlled adsorption of oxygen on tungsten. The sticking probability of CO on a

half monolayer of oxygen on tungsten is much greater than is the incorporation of further oxygen on the tungsten surface. Coverage of the surface might be estimated from results obtained using a retarding field diode. O'Keefe and French[149] employed this technique in their studies on the scattering of inert gases from tungsten.

In further studies of the tungsten surface, use of a single crystal as a target would remove some ambiguities inherent in the current work. Use of a single crystal for a target establishes the orientation of surface atoms in an unequivocal manner. In addition, use of a crystal affords some methods of surface preparation not possible in the current work.

Further studies most obviously should include the other inert gases as well as targets of platinum and nickel. It is particularly important to use the less massive inert gases in these studies. As Smith, Saltsburg, and Palmer[66] note, differences in roughness of surface are not critical for helium. Moreover, if helium were employed in an experiment similar to the one described herein, true diffraction peaks would be expected. Examination of such peaks could lead directly to a determination of the grating spacing for the surface.

Since the nozzle source generates such an intense beam of gas, it might be possible to use a diatomic gas and employ a rotational energy selector to specify J-state prior to interaction with the target. Busby and Trilling[152] have given a simplified theoretical treatment of a system involving the interaction between a one-dimensional rotator and a one-dimensional soft cube surface model. With such a representation of the diatomic atom, they find that 60% to 80% of the energy that is transferred by the interaction is found in rotational

modes. Such a large fraction could probably be seen with the detection system described herein.

SELECTED BIBLIOGRAPHY

1. Harris, I. and Jastrow, R., Planetary and Space Sci., 2, 20 (1959).

2. Moe, K., AIAA Journal, 6, 1375 (1968).

3. Kundt, A. and Warburg, E., Pogg, Ann. Phys., 155, 337 (1875).

4. Maxwell, J. C., The Scientific Papers of James Clerk Maxwell, Vol. 2, Dover, New York, 1952, p. 706.

5. Smoluchowski, M. S., Phil. Mag., 46, 192 (1898).

6. Knudsen, M., Ann. der Physik, 34, 593 (1911).

7. Knudsen, M., Ann. der Physik, 36, 871 (1911).

8. Knudsen, M., The Kinetic Theory of Gases, Methuen, London, 1950.

9. Blodgett, K. B., and Langmuir, I., Phys. Rev., 40, 78 (1932).

10. Raff, L. M., Lorenzen, J. A., and McCoy, B. C., J. Chem. Phys., 46, 4265 (1967).

11. Jackson, J. M. and Mott, N. F., Proc. Royal Soc., A 137, 703 (1932).

12. Kostoff, R. N., Anderson, J. B., and Fenn, J. B., Fundamentals of Gas-Surface Interactions; ed. Saltsburg, H., Smith, J. N., Jr., and Rogers, M., Academic Press, New York, 1967, p. 512.

13. Mair, W. M., Viney, B. W., and Colligon, J. S., Proc. Intern. Symp. Rarefied Gas Dyn., Suppl. 4, 1, 187 (1967).

14. Kennard, E. H., The Kinetic Theory of Gases, McGraw-Hill Book Co., Inc., New York, 1938, p. 311.

15. Moran, J. P., "Experiments on Scattering of Monoenergetic Argon Beams by Heated Platinum", Ph.D. Thesis, Massachusetts Institute of Technology, 1967.

16. Moran, J. P., Wachman, H. Y., and Trilling, L., Phys. of Fluids, 12, 987 (1969).

17. Hinchen, J. J. and Foley, W. M., Proc. Intern. Symp. Rarefied Gas Dyn., Suppl. 3, 2, 505 (1966).

18. Hagena, O. F., Appl. Phys. Let., 9, 385 (1966).

19. Hagena, O. F. and Varma, A. K., Rev. Sci. Instr., 39, 47 (1968).

20. Bishara, M. N. and Fisher, S. S., J. Chem. Phys., 52, 5661 (1970).

21. Wachman, H. Y., ARS Journal, 32, 2 (1962).

22. Thomas, L. B., and Olmer, F. G., J. Amer. Chem. Soc., 64, 2190 (1942).

23. Thomas, L. B. and Golike, R. C., J. Chem. Phys., 22, 300 (1954).

24. Roberts, J. K., Proc. Royal Soc., A 129, 146 (1930).

25. Roberts, J. K., Proc. Royal Soc., A 142, 518 (1933).

26. Roach, D. V. and Thomas, L. B., Proc. Intern. Symp. Rarefied Gas Dyn., Suppl. 4, 1, 163 (1967).

27. Thomas, L. B. and Brown, R. E., J. Chem. Phys., 18, 1367 (1950).

28. Silvernail, W. L., Ph.D. Thesis, University of Missouri, 1954.

29. Faust, J. W., Ph.D. Thesis, University of Missouri, 1954.

30. Thomas, L. B. and Schofield, E. B., J. Chem. Phys., 23, 861 (1955).

31. Thomas, L. B., Proc. Intern. Symp. Rarefied Gas Dyn., Suppl. 4, 1, 155 (1967).

32. Thomas, L. B., Fundamentals of Gas-Surface Interactions, ed. Saltsburg, H., Smith, J. N., Jr., and Rogers, M., Academic Press, New York, 1967, p. 346.

33. Eggleton, A. E. J. and Tompkins, F. C., Trans. Farad. Soc., 48, 738 (1952).

34. Menzel, D. and Kouptsidis, J., Fundamentals of Gas-Solid Interactions, ed. Saltsburg, H., Smith, J. N., Jr., and Rogers, M., Academic Press, New York, 1967, p. 493.

35. Jackson, J. M., Proc. Camb. Phil. Soc., 28, 136 (1932).

36. Jackson, J. M. and Howarth, A., Proc. Royal Soc., A 142, 447 (1933).

37. Devonshire, A. F., Proc. Royal Soc., A 158, 269 (1937).

38. Landau, L., Phys. Zeit. der Sowjetunion, 5, 489 (1935).

39. Brown, R. E., Ph.D. Thesis, University of Missouri, 1957.

40. Zwanzig, R. W., J. Chem. Phys., 32, 1173 (1960).

41. Cabrera, N. B., Disc. Farad. Soc., 28, 16 (1959).

42. Goodman, F. O., J. Phys. Chem. Solids, 23, 1269 (1962).

43. Goodman, F. O., J. Phys. Chem. Solids, 23, 1491 (1962).

44. Goodman, F. O., J. Phys. Chem. Solids, 24, 1451 (1963).

45. Goodman, F. O., J. Phys. Chem. Solids, 26, 85 (1965).

46. Goodman, F. O., Surf. Sci., 3, 368 (1965).

47. Goodman, F. O., Proc. Intern. Symp. Rarefied Gas Dyn., Suppl. 3, 2, 366 (1966).

48. Goodman, F. O., Proc. Intern. Symp. Rarefied Gas Dyn., Suppl. 4, 1, 35 (1967).

49. Goodman, F. O., Surf. Sci., 7, 391 (1967).

50. Goodman, F. O., Surf. Sci., 11, 283 (1968).

51. Goodman, F. O., Proc. Intern. Symp. Rarefied Gas Dyn., Suppl. 5, 2, 1105 (1969).

52. Goodman, F. O. and Wachman, H. Y., J. Chem. Phys., 46, 2376 (1967).

53. Goodman, F. O., J. Chem. Phys., 55, 5742 (1971).

54. Trilling, L., J. de Mecanique, 3, 215 (1964).

55. Trilling, L., Phys. Fluids, 7, 1681 (1964).

56. Trilling, L., Fundamentals of Gas-Surface Interactions, ed. Saltsburg, H., Smith, J. N., Jr., and Rogers, M., Academic Press, New York 1967, p. 392.

57. Trilling, L., Proc. Intern. Symp. Rarefied Gas Dyn., Suppl. 5, 2, 139 (1969).

58. Roberts, R. W., Brit. J. App. Phys., 14, 537 (1963).

59. Smith, J. N., Jr. and Saltsburg, H., J. Chem. Phys., 40, 3585 (1964).

60. Smith, J. N., Jr. and Saltsburg, H., J. Chem. Phys., 45, 2175 (1966).

61. Smith, J. N., Jr. and Saltsburg, H., Proc. Intern. Symp. Rarefied Gas Dyn., Suppl. 3, 2, 491 (1966).

62. Smith, J. N., Jr. and Saltsburg, H., Fundamentals of Gas-Surface Interactions, ed. Saltsburg, H., Smith, J. N., Jr., and Rogers, M., Academic Press, New York, 1967, p. 370.

63. Saltsburg, H., Smith, J. N., Jr., and Palmer, R. L., Proc. Intern. Symp. Rarefied Gas Dyn., Suppl. 4, 1, 223 (1967).

64. Saltsburg, H., Smith, J. N., Jr., and Palmer, R. L., J. Chem. Phys., 49, 1287 (1968).

65. Saltsburg, H., Smith, J. N., Jr., and Palmer, R. L., Bull. Am. Phys. Soc., Series II, 13, 906 (1968).

66. Saltsburg, H., Smith, J. N., Jr., and Palmer, R. L., Proc. Intern. Symp. Rarefied Gas Dyn., Suppl. 5, 2, 1141 (1969).

67. Palmer, R. L., Saltsburg, H., and Smith, J. N., Jr., J. Chem. Phys., 50, 4661 (1969).

68. Palmer, R. L., O'Keefe, D. R., Saltsburg, H., and Smith, J. N., Jr., J. Vac. Sci. and Tech., 7, 91 (1970).

69. Palmer, R. L., Smith, J. N., Jr., Saltsburg, H., and O'Keefe, D. R., J. Chem. Phys., 53, 1666 (1970).

70. Belous, M. V. and Wayman, C. M., J. App. Phys., 38, 5119 (1967).

71. Hinchen, J. J. and Shepard, E. F., Proc. Intern. Symp. Rarefied Gas Dyn., Suppl. 4, 1, 239 (1967).

72. Hinchen, J. J. and Malloy, E. S., Fundamentals of Gas-Surface Interactions, ed. Saltsburg, H., Smith, J. N., Jr., and Rogers, M., Academic Press, New York, 1967, p. 448.

73. Esterman, J. and Stern, O., Z. Phys., 61, 95 (1930).

74. Frisch, O. R., Z. Phys., 64, 430 (1933).

75. Crews, J. C., J. Chem. Phys., 37, 2004 (1962).

76. Crews, J. C., Fundamentals of Gas-Surface Interactions, ed. Saltsburg, H., Smith, J. N., Jr., and Rogers, M., Academic Press, New York, 1967, p. 480.

77. Lennard-Jones, J. E. and Devonshire, A. F., Proc. Royal Soc., A 158, 253 (1937).

78. O'Keefe, D. R. Palmer, R. L., Saltsburg, H. and Smith, J. N., Jr., J. Chem. Phys., 49, 5194 (1968).

79. Smith, J. N., Jr., O'Keefe, D. R., Saltsburg, H., and Palmer, R. L., J. Chem. Phys., 50, 4667 (1969).

80. Smith, J. N., Jr., O'Keefe, D. R., and Palmer, R. L., J. Chem. Phys., 52, 315 (1970).

81. O'Keefe, D. R., Smith, J. N., Jr., Palmer, R. L., and Saltsburg, H., J. Chem. Phys., 52, 4447 (1970).

82. Palmer, R. L., and O'Keefe, D. R., App. Phys. Letters, 16, 529 (1970).

83. Zahl, H. A. and Ellet, A., Phys. Rev., 37, 1705 (1931).

84. Zah., H. A. and Ellet, A., Phys. Rev., 38, 977 (1931).

85. Zabel, R. M., Phys. Rev., 42, 218 (1932).

86. Kellog, J. N. B., Phys. Rev., 41, 635 (1932).

87. Hancox, R. R., Phys. Rev., 42, 864 (1932).

88. Fisher, S. S., Bishara, M. N., Kuhlthau, A. R., and Scott, J. E., Proc. Symp. Rarefied Gas Dyn., Suppl. 5., 2, 1227 (1969).

89. Fite, W. L. and Brackman, R. T., Phys. Rev., 112, 1141 (1958).

90. Smith, J. N., Jr., J. Chem. Phys., 40, 2050 (1965).

91. Smith, J. N., Jr., General Atomic Report No. GA-4665 (Nov. 5, 1963).

92. Smith, J. N., Jr., and Fite, W. L., Proc. Intern. Symp. Rarefied Gas Dyn., Suppl. 1, 2, 430 (1963).

93. Yamamoto, S. and Stickney, R. E., J. Chem. Phys., 53, 1594 (1970).

94. Stoll, A. G., Smith, D. L., and Merrill, R. P., J. Chem. Phys., 54, 163 (1971).

95. Logan, R. M., and Keck, J. C., J. Chem. Phys., 49, 860 (1968).

96. Smith, D. L. and Merrill, R. P., J. Chem. Phys., 53, 3588 (1970).

97. West, L. A. and Somorjai, G. A., J. Chem. Phys., 54, 2864 (1971).

98. Esterman, I., Frisch, R., and Stern, O., Z. Physik, 73, 348 (1931).

99. Frisch, R., and Stern, O., Z. Physik, 84, 430 (1933).

100. Frisch, R., Z. Physik, 84, 443 (1933).

101. Phillips, C. S. G., and Williams, R. J. P., Inorganic Chemistry, Oxford University Press, New York, 1965, p. 153.

102. Williams, B. R., J. Chem. Phys., 55, 1315 (1971).

103. Williams, B. R., J. Chem. Phys., 55, 3220 (1971).

104. Mason, B. F., and Williams, B. R., J. Chem. Phys., 56, 1895 (1972).

105. Weinberg, W. H. and Merrill, R. P., Phys. Rev. Letters, 25, 1198 (1970).

106. Moore, G. E., Datz, S., and Taylor, E. H., J. Catalysis, 5, 218 (1966).

107. Yamamoto, S. and Stickney, R. E., J. Chem. Phys., 47, 1091 (1967).

108. Knuth, E. L., Appl. Mech. Rev., 17, 751 (1964).

109. Oman, R. A., J. Chem. Phys., 48, 3919 (1968).

110. Hays, W. J., Rodgers, W. E., and Knuth, E. L., J. Chem. Phys., 56, 1652 (1972).

111. Miller, D. R. and Subbarao, R. B., J. Chem. Phys., 52, 425 (1970).

112. Baule, B., Ann. der Phys., 44, 145 (1914).

113. Beder, E., Surf. Sci., 1, 242 (1964).

114. Feuer, P., J. Chem. Phys., 39, 1311 (1963).

115. Allen, R. T. and Feuer, P., J. Chem. Phys., 43, 4500 (1965).

116. Allen, R. T. and Feuer, P., Proc. Intern. Symp. Rarefied Gas Dyn., Suppl. 4, 1, 109 (1967).

117. Logan, R. M., Keck, J. C., and Stickney, R. E., Proc. Intern. Symp. Rarefied Gas Dyn., Suppl. 4, 1, 49 (1967).

118. Logan, R. M., and Keck, J. C., J. Chem. Phys., 44, 195 (1966).

119. Oman, R. A., Bogan, A., Weiser, C. H., and Li, C. H., AIAA J., 2, 1722 (1964).

120. Oman, R. A., Bogan, A., and Li, C. H., Proc. Intern. Symp. Rarefied Gas Dyn., Suppl. 3, 2, 396 (1966).

121. Oman, R. A., AIAA J., 5, 1280 (1967).

122. Oman, R. A., Proc. Intern. Symp. Rarefied Gas Dyn., Suppl. 4, 1, 83 (1967).

123. Oman, R. A., J. Chem. Phys., 48, 3919 (1968).

124. Lorenzen, J. A. and Raff, L. M., J. Chem. Phys., 49, 1165 (1968).

125. Lorenzen, J. A. and Raff, L. M., J. Chem. Phys., 52, 1133 (1970).

126. Lorenzen, J. A. and Raff, L. M., J. Chem. Phys., 54, 674 (1971).

127. McClure, J. D. and Wu, Y., Proc. Symp. Rarefied Gas Dyn., Suppl. 5, 2, 1191 (1969).

128. McClure, J. D., J. Chem. Phys., 51, 1687 (1969).

129. McClure, J. D., J. Chem. Phys., 52, 2712 (1970).

130. McCarroll, B., J. Chem. Phys., 46, 863 (1967).

131. Musket, R. G., J. Less-Common Metals, 22, 175 (1970).

132. King, D. A., Madey, T. E., and Yates, J. T., Jr., J. Chem. Phys., 55, 3236 (1971).

133. King, D. A., Madey, T. E., and Yates, J. T., Jr., J. Chem. Phys., 55, 3247 (1971).

134. Kohrt, C., and Gomer, R., J. Chem. Phys., 52, 3283 (1970).

135. Ptushinskii, Y. G. and Chuikov, B. A., Surface Sci., 4, 452 (1966).

136. Germer, L. H. and May, J. W., Surface Sci., 4, 452 (1966).

137. Footnote 30, Ref. 132

138. Batzer, T. H. and Ryan, J. F., 1963 Vacuum Symposium Transactions, The Macmillan Company, New York, 1963, p. 166.

139. Batzer, T. H., University of California, Lawrence Radiation Laboratory (Livermore), Engineering Note No. 5505 - 45, Rev. Nov. 11, 1967.

140. Moran, J. P., AIAA Journal, 8, 539 (1970).

141. Hostettler, S. O. and Bernstein, R. B., Rev. Sci. Instr., 31, 872 (1960).

142. Trujillo, S. M., Rol, P. K., and Rothe, E. W., Rev. Sci. Instr., 33, 841 (1962).

143. Ehrlich, G. and Hudda, F. G., J. Chem. Phys., 44, 1039 (1966).

144. Brennan, D., Hayward, D. O., and Trapnell, B. M. W., Proc. Royal Soc., A 256, 81 (1960).

145. Tamm, P. W. and Schmidt, L. D., J. Chem. Phys., 55, 4253 (1971).

146. Anderson, J. and Danforth, W. E., J. Franklin Inst., 279, 160 (1965).

147. Tracey, J. C. and Blakely, J. M., Surface Sci., 13, 313 (1969).

148. Hopkins, B. J., Pender, K. R., and Usami, S., Fundamentals of Gas-Solid Interactions, ed. Saltsburg, H., Smith, J. N., Jr., and Rogers, M., Academic Press, New York, 1967, p. 284.

149. O'Keefe, D. R. and French, J. B., Proc. Intern. Symp. Rarefied Gas Dyn., Suppl. 5, 2, 1279 (1969).

150. McGinn, I. H., Proc. Symp. Rarefied Gas Dyn., Suppl. 5, 2, 1025 (1969).

151. McKinley, J. D., J. Phys. Chem., 66, 554 (1962).

152. Busby, M. R. and Trilling, L., Proc. Symp. Rarefied Gas Dyn., Suppl. 5, 2, 1135 (1969).

VITA

John William Coryell

Candidate for the Degree of

Doctor of Philosophy

Thesis: AN EXPERIMENTAL INVESTIGATION OF GAS-SOLID INTERACTION PHENOMENA

Major Field: Chemistry

Biographical:

Personal Data: Born in Watonga, Oklahoma, July 23, 1940, the son of Allen and Bonnie Coryell.

Education: Graduated from Waverly Rural High School, Waverly, Kansas, in May, 1958; received a Bachelor of Science degree with a major in Chemistry from Oklahoma State University in May, 1965; attended Kansas State Teachers' College of Emporia, Kansas and the University of Tulsa; completed requirements for the Doctor of Philosophy degree at Oklahoma State University in May, 1972.

Professional Experience: Laboratory Assistant, Jersey Production Research Company, 1962-1964; Graduate Teaching Assistant, Oklahoma State University, 1965-1969; Graduate Research Assistant, Oklahoma State University, 1966-1970; Research Chemist, E. I. duPont de Nemours & Co., Inc., 1970-1972.